Intricate kinetics: in-situ FTIR-spectroscopy discloses a phase change during ionic liquid synthesis

A. Ohligschläger[a] and M. A. Liauw[a]

Institut für Technische Chemie und Makromolekulare Chemie (ITMC), RWTH Aachen University

Worringerweg 1, 52056 Aachen, Germany

E-mail: ohligschlaeger@itmc.rwth-aachen.de/liauw@itmc.rwth-aachen.de

Table of Contents

1   Experimental Procedure

A 20 mL window autoclave has been applied with two ATR-IR fibre optical probes with two internal reflection elements from ifs Aachen. One probe is applied for the lower liquid phase, one for the upper gaseous phase. After recording a reference spectrum against air, the solvent methanol and the substrates triethylamine and dimethyl carbonate are inserted and the autoclave is sealed. While continuously recording spectra of upper and lower phase in an alternating manner, the autoclave is heated up to reaction temperature. The reaction is terminated after several hours. The chilled product phase is purified via removing the volatile components under vacuum.

Table 1: List of used reaction temperatures. The graphs of Experiment No. OHL-056 have also been shown in the communication.

Experiment No.	Temperature T [K]
OHL-057	363.15
OHL-069	378.15
OHL-068	388.15
OHL-067	393.15
OHL-056	398.15
OHL-064	398.15
OHL-066	398.15
OHL-060	403.15
OHL-054	408.15
OHL-061	413.15

Table 2: Weights, amounts and volumes of the substrates and the solvent.

	Methanol	Triethylamine	Dimethyl carbonate
Molar fraction	0.60	0.20	0.20
Mass [g]	4.18	4.40	3.92
Volume [mL]	5.30	6.03	3.67
Amount [mmol]	130	43.5	43.5
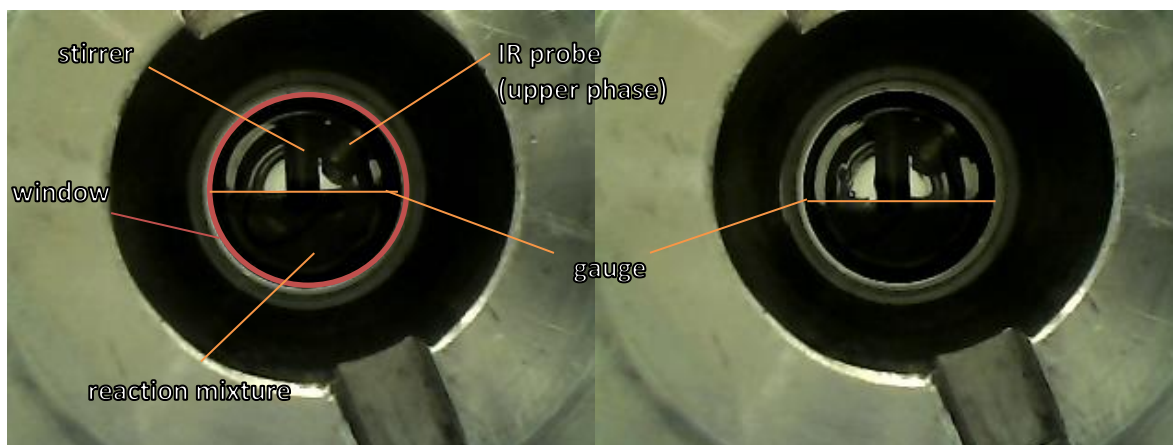
Figure 1: Pictures of the reaction mixture through the autoclave window at the beginning (left) and after two hours reaction time (right) of OHL-054. The decreasing gauge of the liquid phase emphasizes that the density increases with the reaction progress. The pictures have been taken with a BS-19+ USB-endoscope (Voltcraft).

1.1 NMR-Spectrum of the Product

OHA-01.10.fid
OHA
@1H CDCl3 /opt/topspin3.0 Leitner
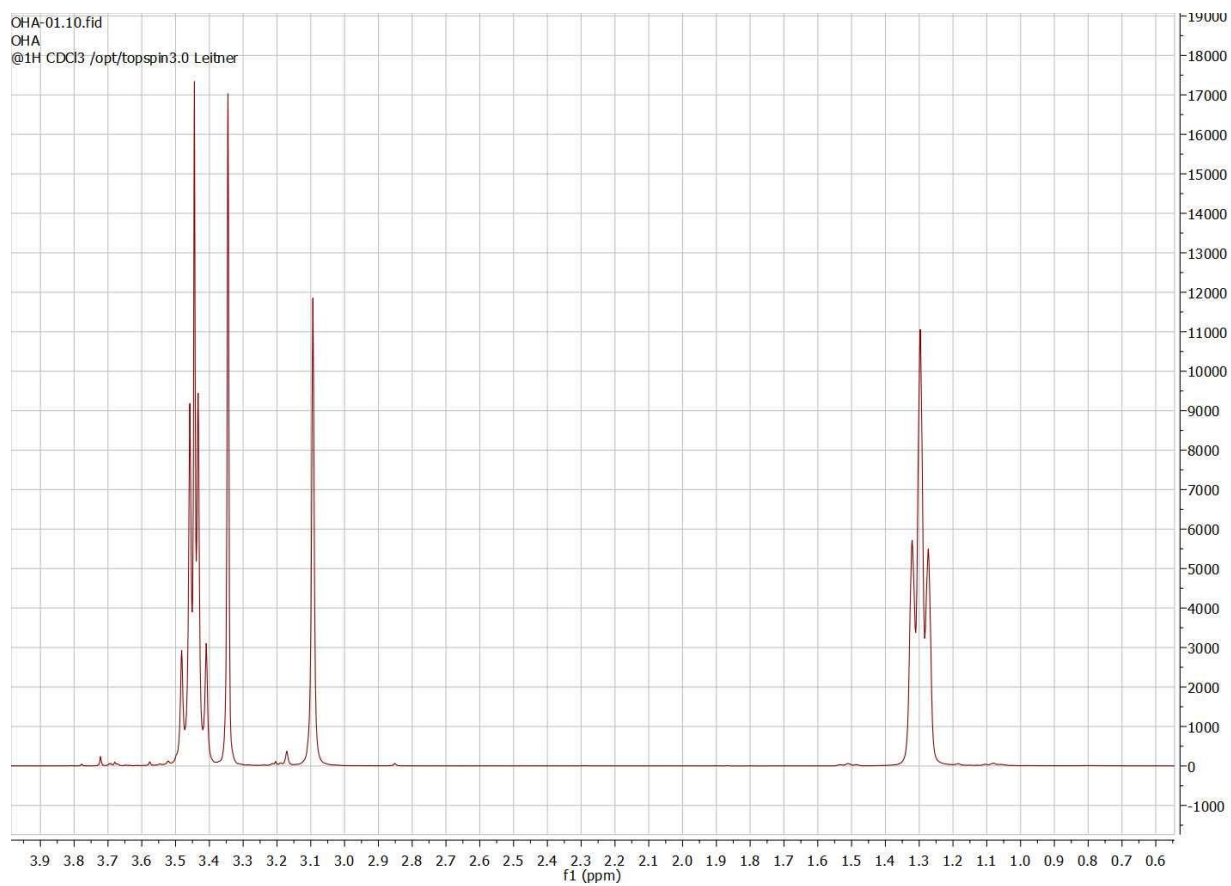
Figure 2: NMR spectrum of MeNEt$_3$ MeOCOO.

^{1}H-NMR (400 MHz, CDCl$_3$) δ 1.30 ppm (t, ^3J = 12 Hz, 9 H, CH$_3$(Et in MeNEt$_3^+$)), 3.09 ppm (s, 3 H, CH$_3$(Me in MeNEt$_3^+$)), 3.34 ppm (s, 3 H, CH$_3$(MeOCOO$^-$)), 3.44 ppm (q, ^3J = 12 Hz, 6 H, CH$_2$(Et in MeNEt$_3^+$)), 3.44 ppm (s, 3 H, CH$_3$(MeOH)).

2   Model and Calibration

2.1   Reference Spectra
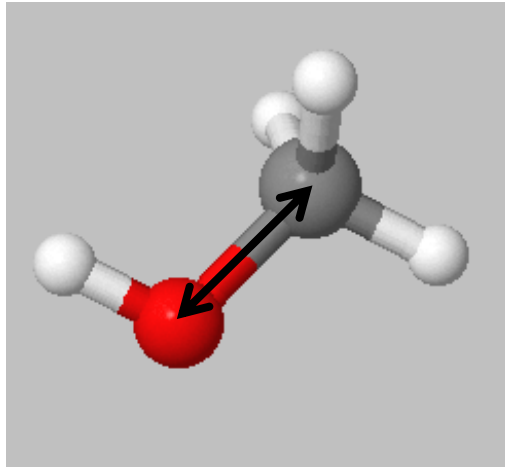
Figure 3: $v(H_3C\text{-}O)$ stretching vibration of methanol[1].
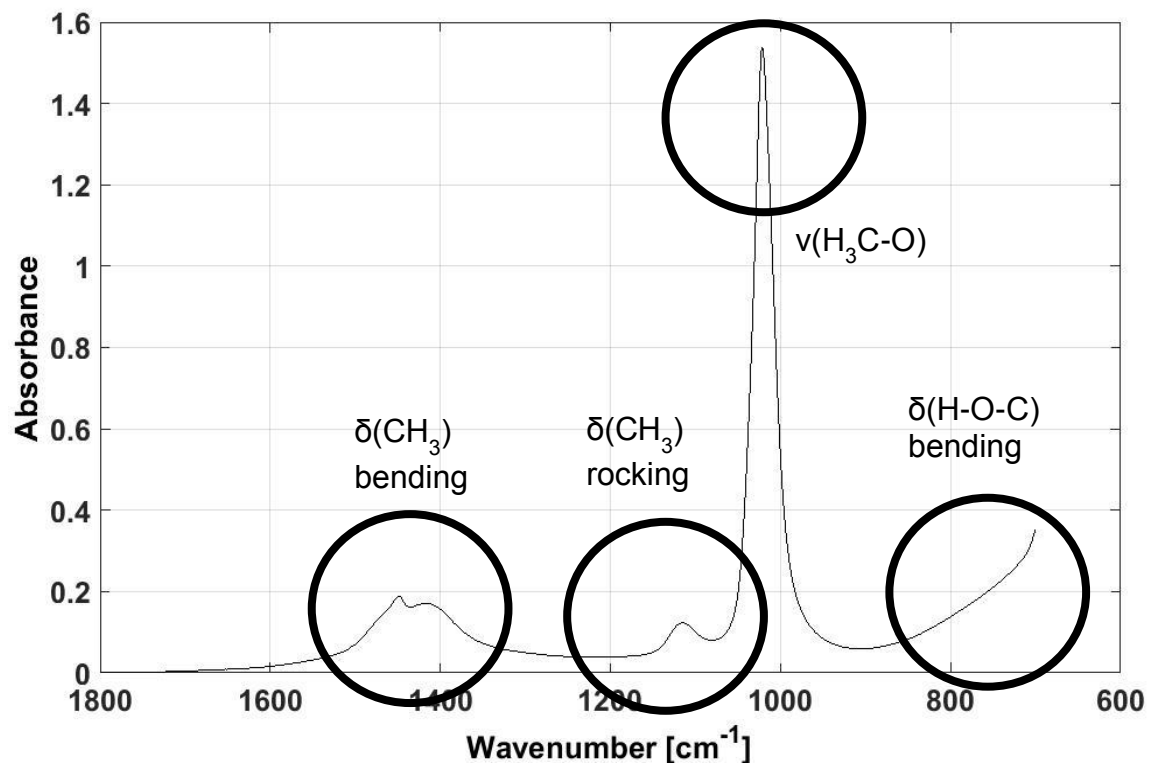
Figure 4: mIR spectrum of methanol. The marked $v(H_3C\text{-}O)$ band is used for the peak integration model, though it is overlapping with the peaks of the other substances. The high absorbance of this peak still allows integrating the central part of the peak.
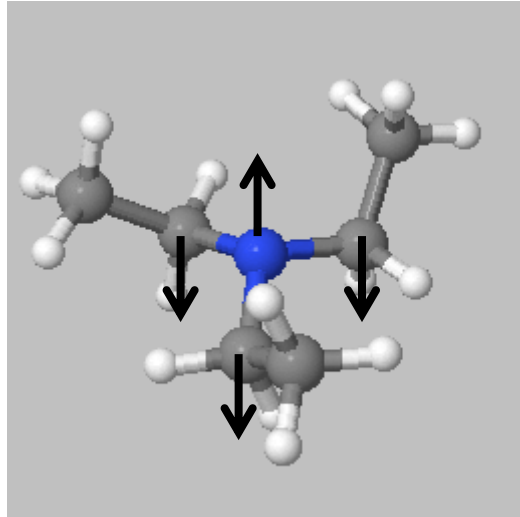
Figure 5: $\delta(NC_3)$ deformation vibration of triethylamine[1].
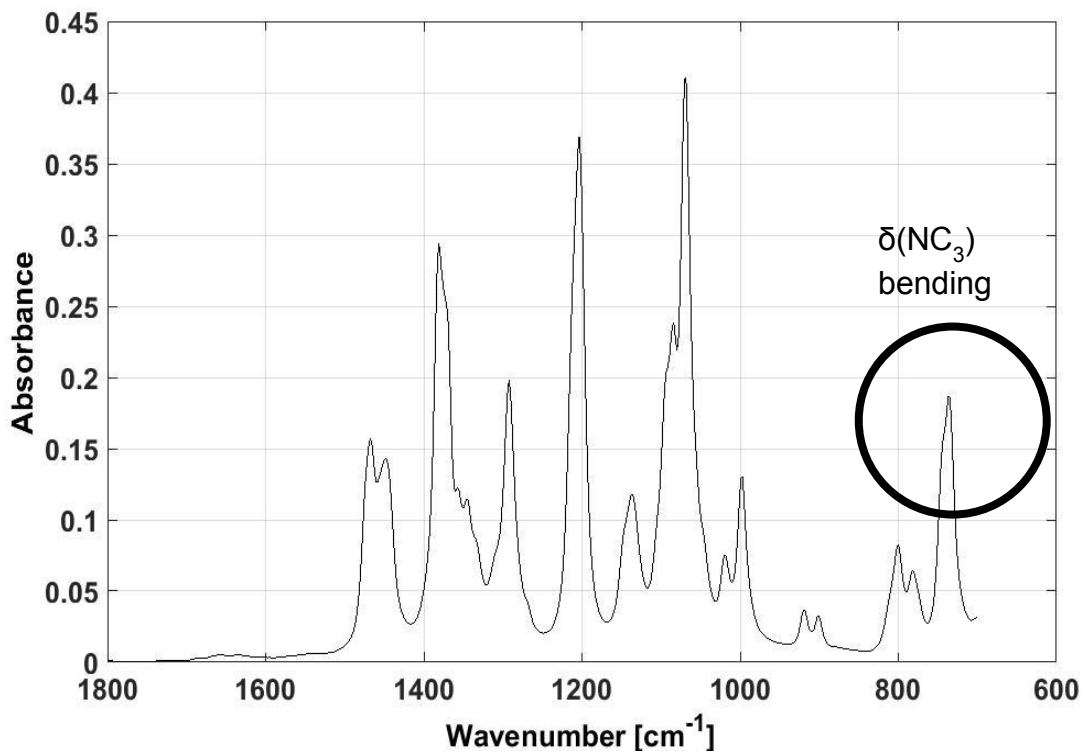
Figure 6: mIR spectrum of triethylamine. The overall low absorbance of the spectrum has to be considered. The marked band is used for the peak integration model, as it is located isolated.
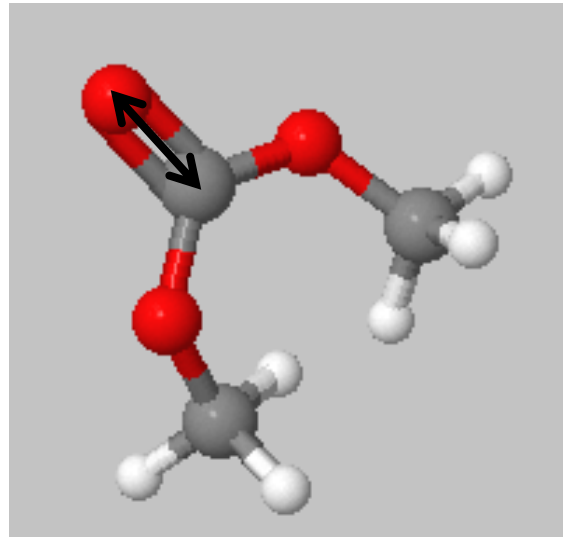
Figure 7: v(C=O) stretching vibration of dimethyl carbonate[1].
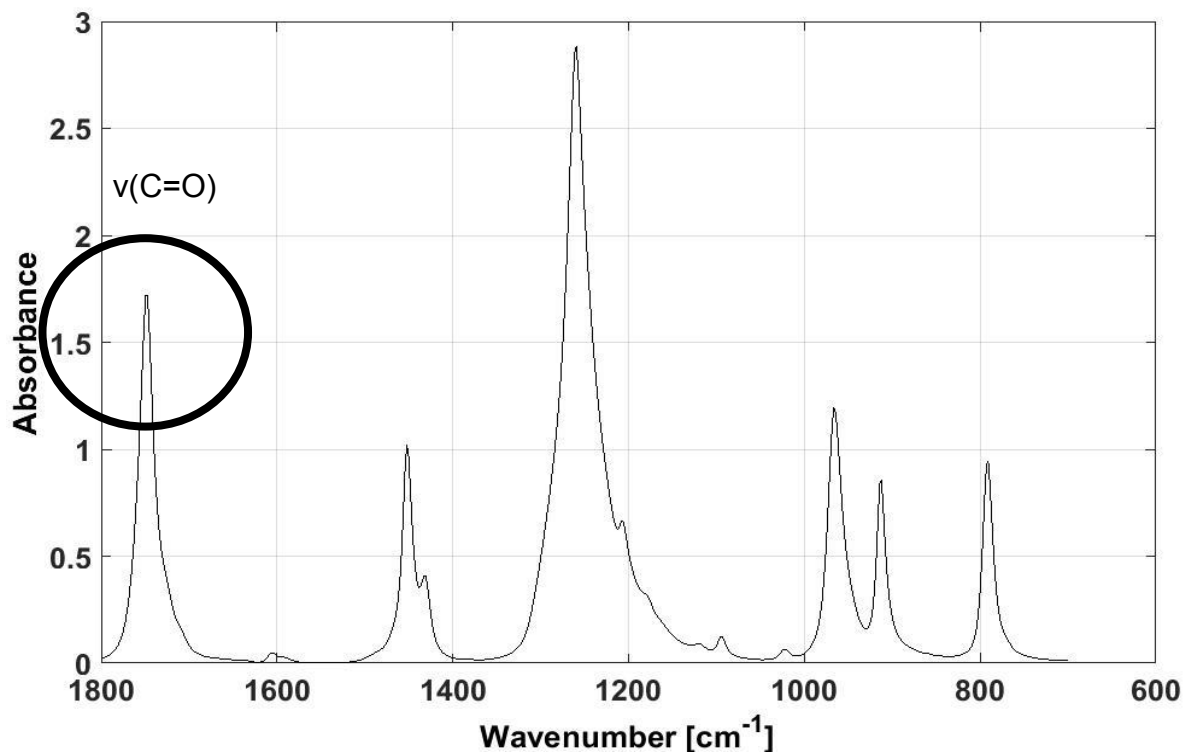
Figure 8: mIR spectrum of dimethyl carbonate. The marked band is used for the peak integration

model, as it is located isolated.
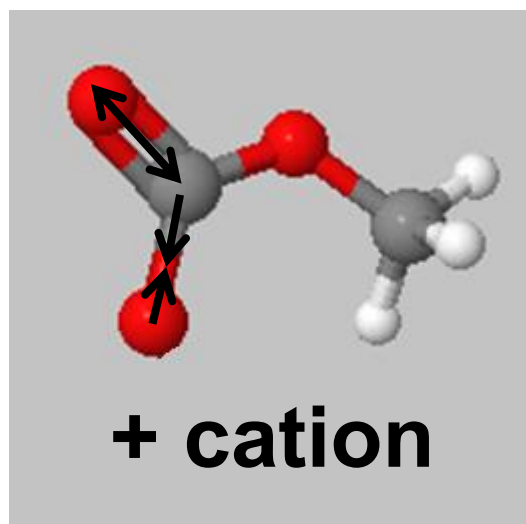
Figure 9: v(C=O) stretching vibration of monomethyl carbonate[1].
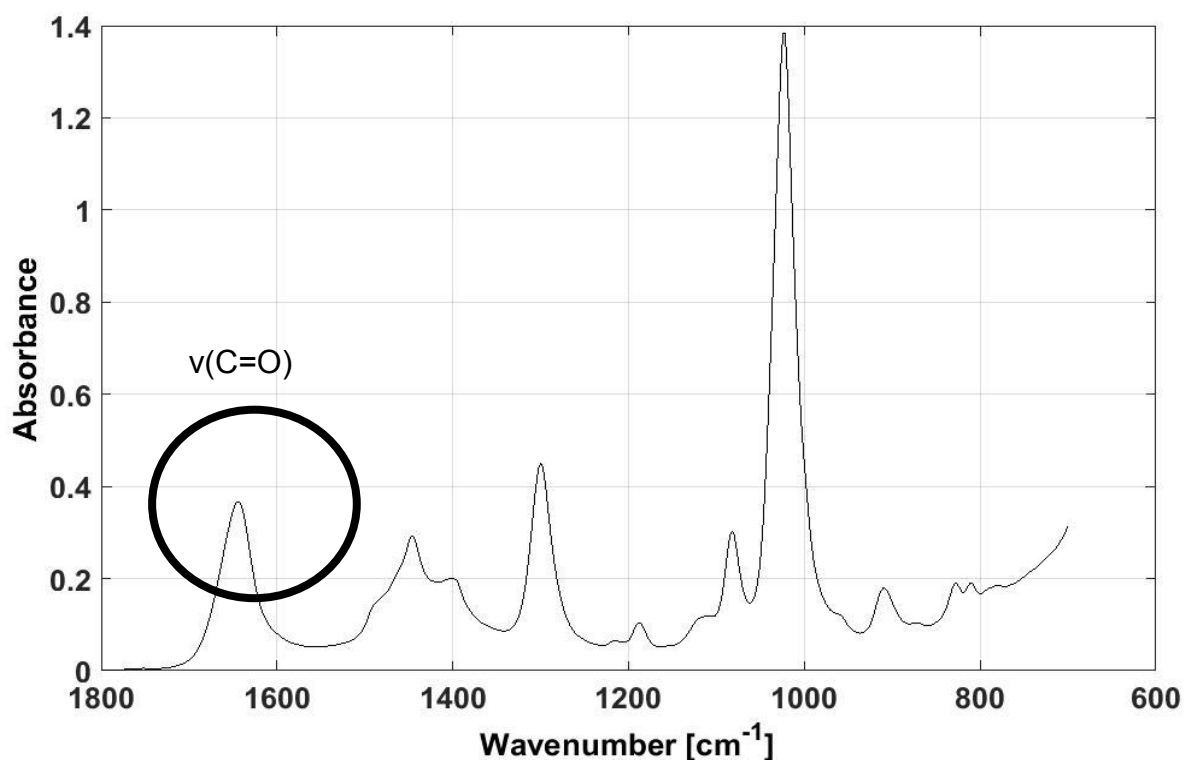
Figure 10: mIR spectrum of MeNEt$_3$ MeOCOO in methanol. The marked band is used for the peak integration model, as it is located isolated.

2.2   Peak Integration Model
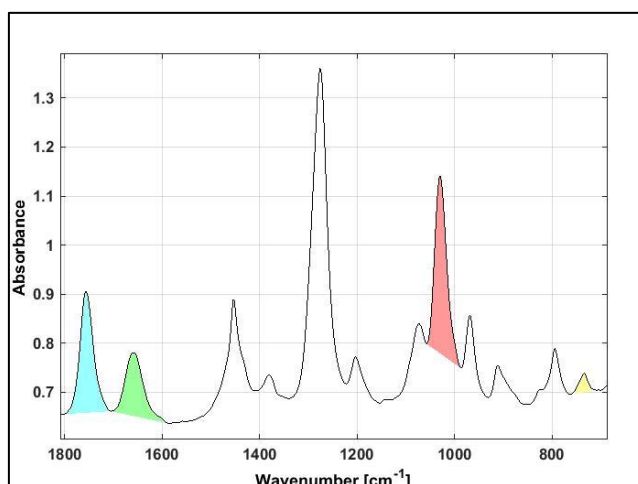
Figure 11: Peak integration model for mixtures of methanol, triethylamine, dimethyl carbonate and MeNEt$_3$ MeOCOO.

2.3   Calibration
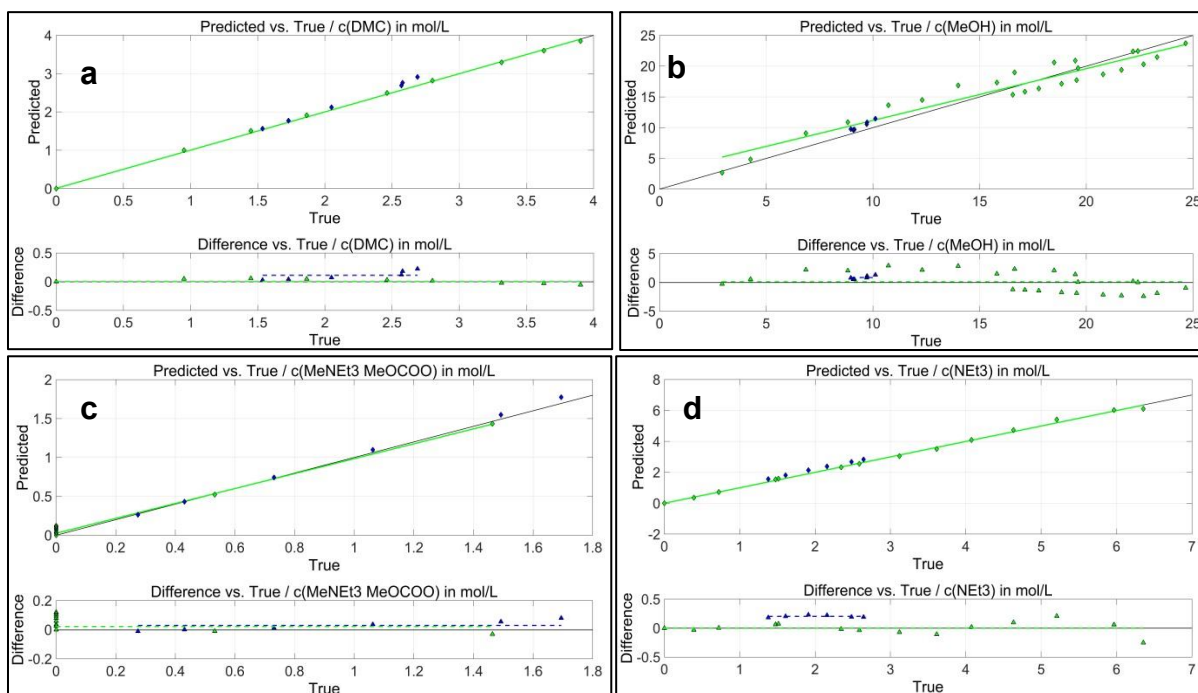
Figure 12: Predicted vs. true plots for dimethyl carbonate (a), methanol (b), MeNEt$_3$ MeOCOO (c) and triethylamine (d). Calibration samples (green symbols) are binary mixtures for each component with methanol while validation samples (blue symbols) consist of quaternary mixtures of all components.

Table 3: RMSECV and RMSEP values of the peak integration model.

Substance	RMSECV [mol L^{-1}]	RMSEP [mol L^{-1}]
Methanol	1.88	0.93
Dimethyl carbonate	0.026	0.14
Triethylamine	0.12	0.21
MeNEt$_3$ MeOCOO	0.065	0.044

3   Results

3.1   IR Spectra
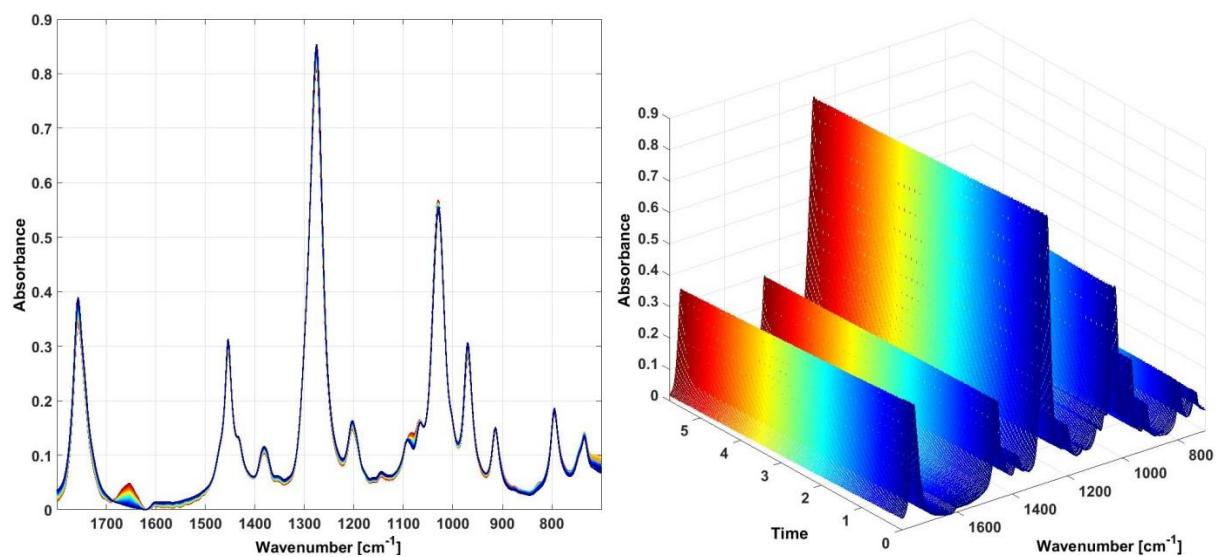
Figure 13: 2D plot (left) and 3D plot (right) of time-resolved mIR spectra of the reaction mixture at 90 °C (Exp. No. OHL-057).
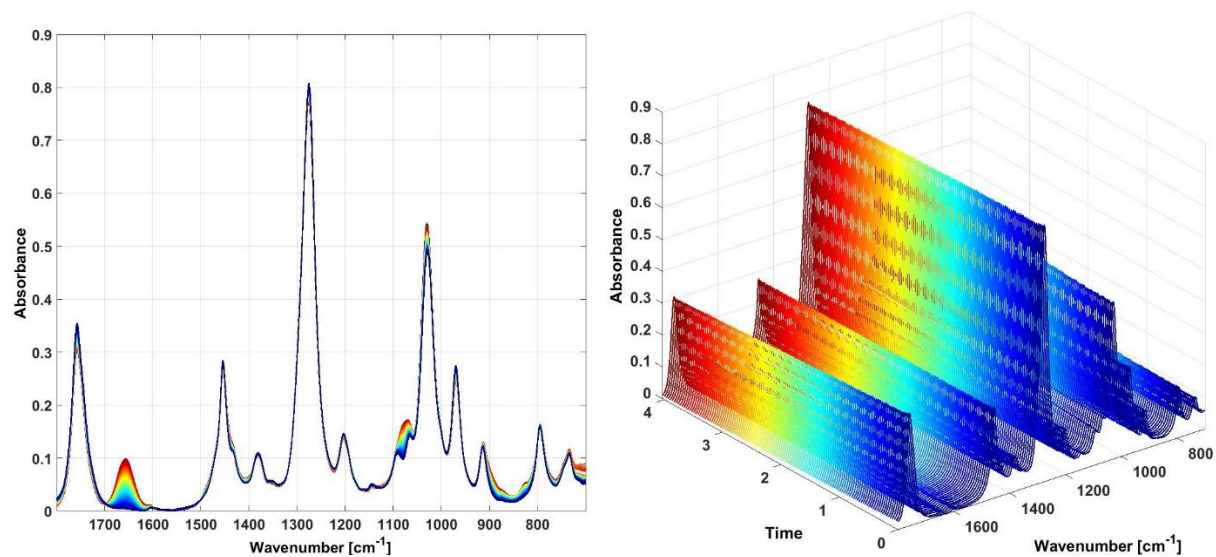
Figure 14: 2D plot (left) and 3D plot (right) of time-resolved mIR spectra of the reaction mixture at 105 °C (Exp. No. OHL-069).
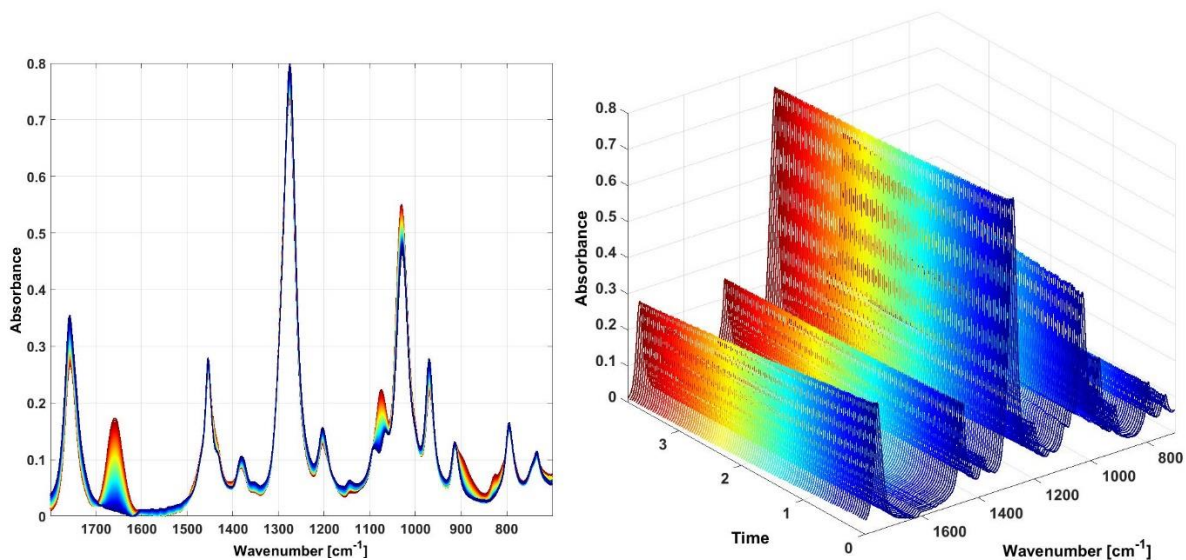
Figure 15: 2D plot (left) and 3D plot (right) of time-resolved mIR spectra of the reaction mixture at 115 °C (Exp. No. OHL-068).
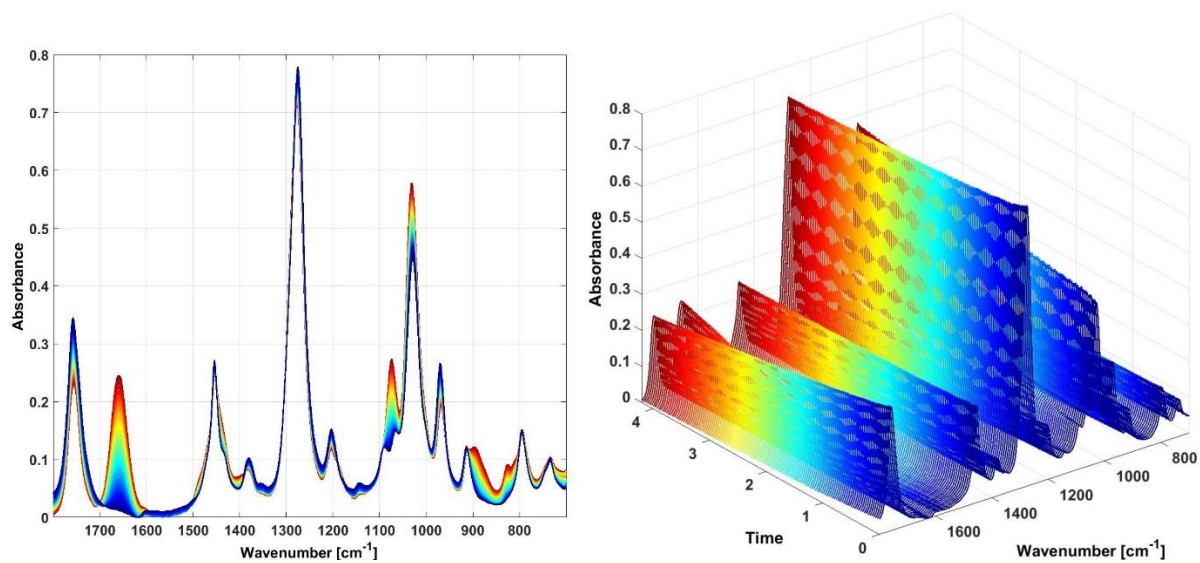
Figure 16: 2D plot (left) and 3D plot (right) of time-resolved mIR spectra of the reaction mixture at 120 °C (Exp. No. OHL-067).
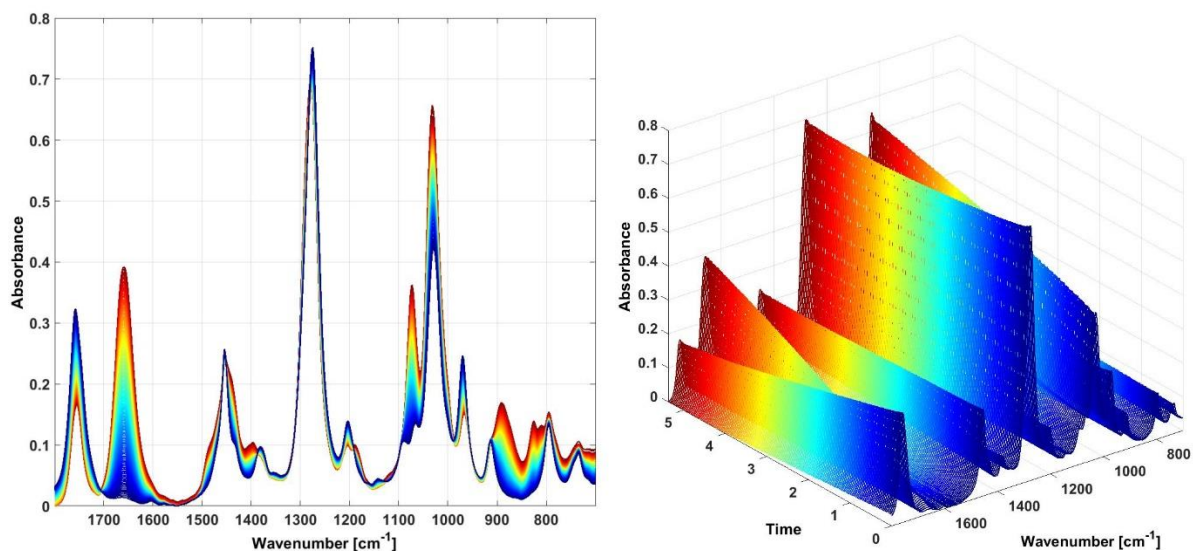
Figure 17: 2D plot (left) and 3D plot (right) of time-resolved mIR spectra of the reaction mixture at 125 °C (Exp. No. OHL-056).
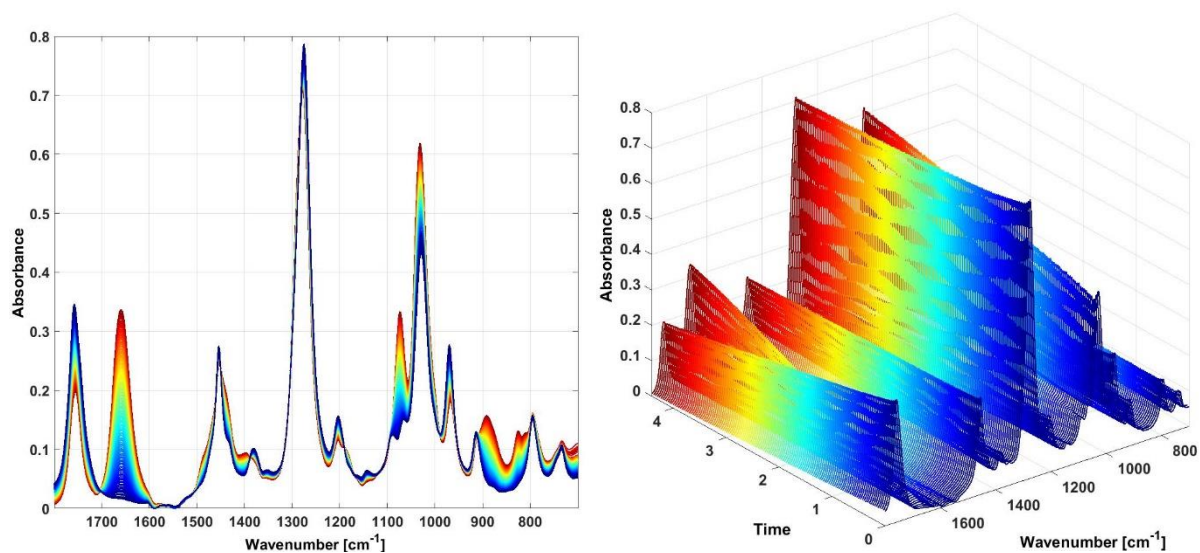
Figure 18: 2D plot (left) and 3D plot (right) of time-resolved mIR spectra of the reaction mixture at 125 °C (Exp. No. OHL-064).
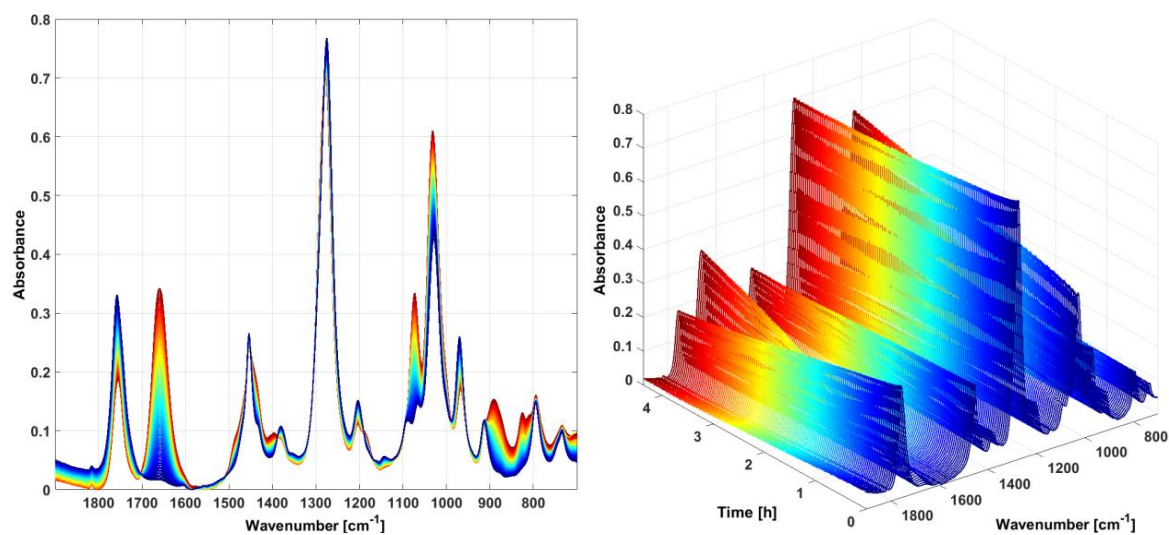
Figure 19: 2D plot (left) and 3D plot (right) of time-resolved mIR spectra of the reaction mixture at 125 °C (Exp. No. OHL-066).
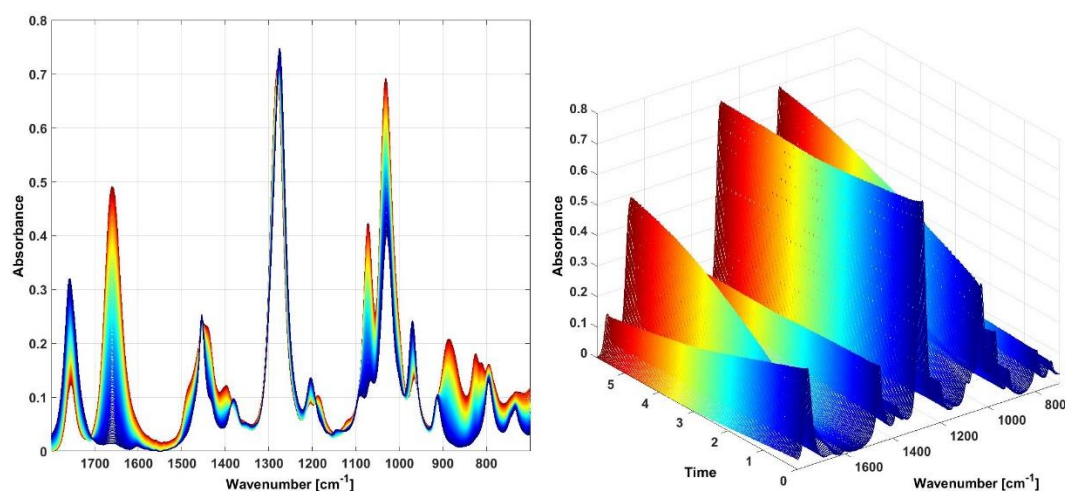
Figure 20: 2D plot (left) and 3D plot (right) of time-resolved mIR spectra of the reaction mixture at 125 °C (Exp. No. OHL-060).
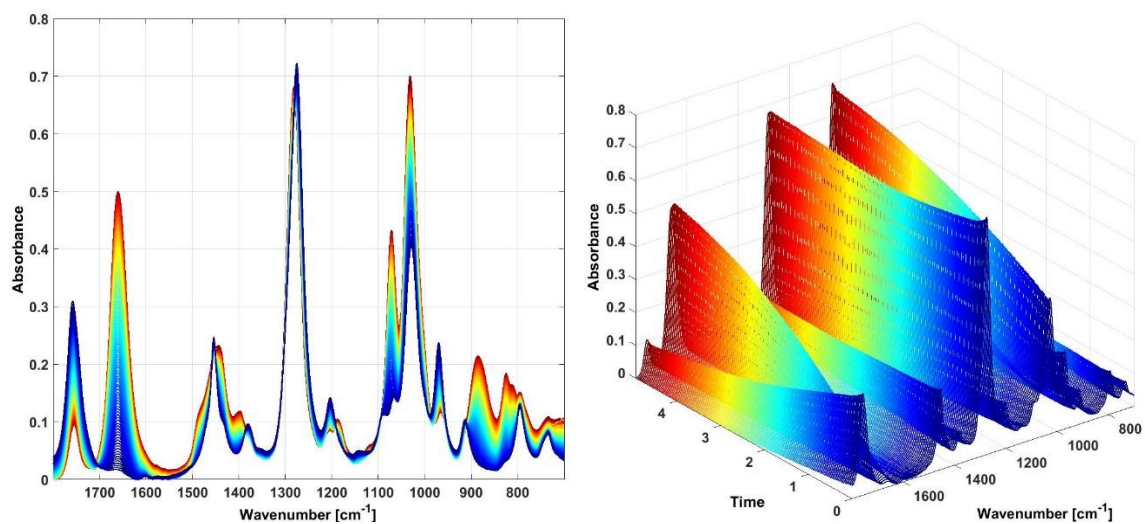
Figure 21: 2D plot (left) and 3D plot (right) of time-resolved mIR spectra of the reaction mixture at 135 °C (Exp. No. OHL-054).
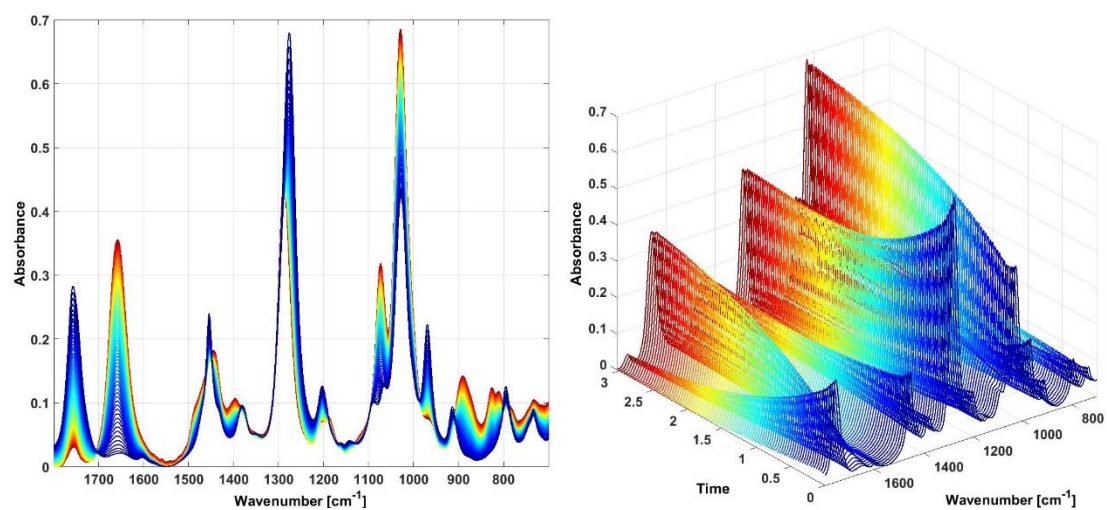
Figure 22: 2D plot (left) and 3D plot (right) of time-resolved mIR spectra of the reaction mixture at 140 °C (Exp. No. OHL-061).

3.2   Concentration and Reaction Rate Profiles
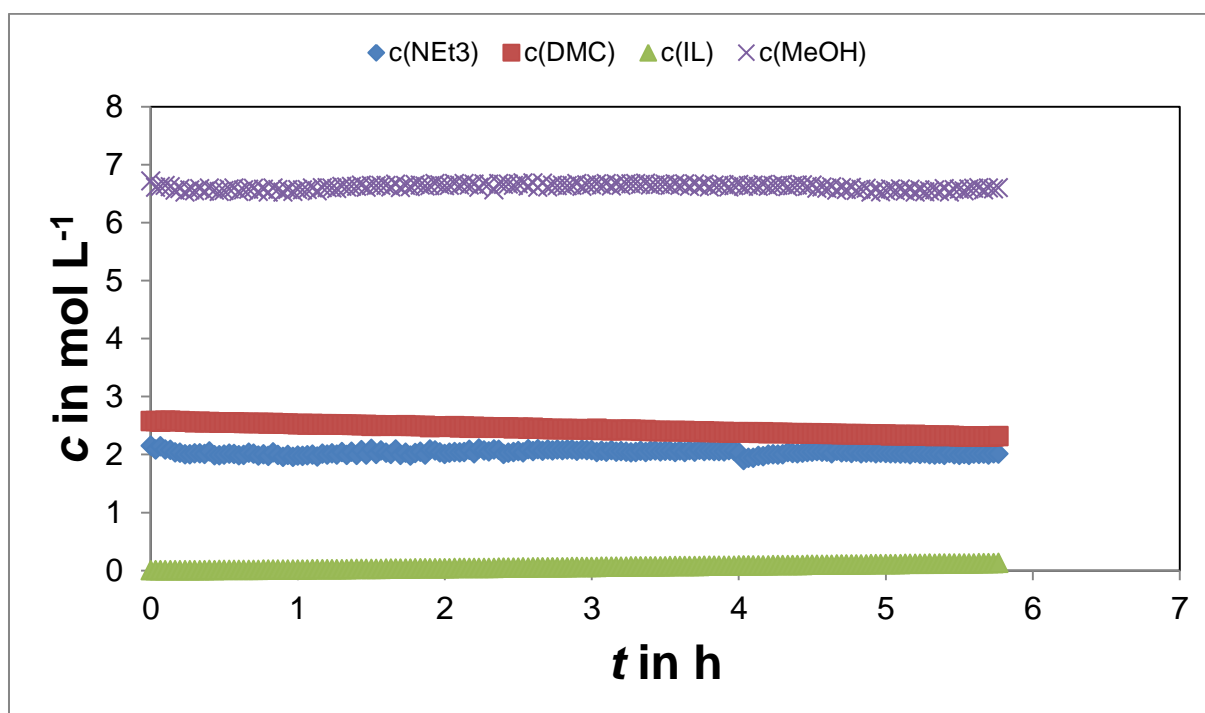
Figure 23: Concentration profiles of solvent, substrates and product determined via Peak Integration at 90 °C (Exp. No. OHL-057). The discontinuity in the triethylamine profile at about 4 h corresponds to refilling of liquid nitrogen which interferes with the relatively small signal of this compound.
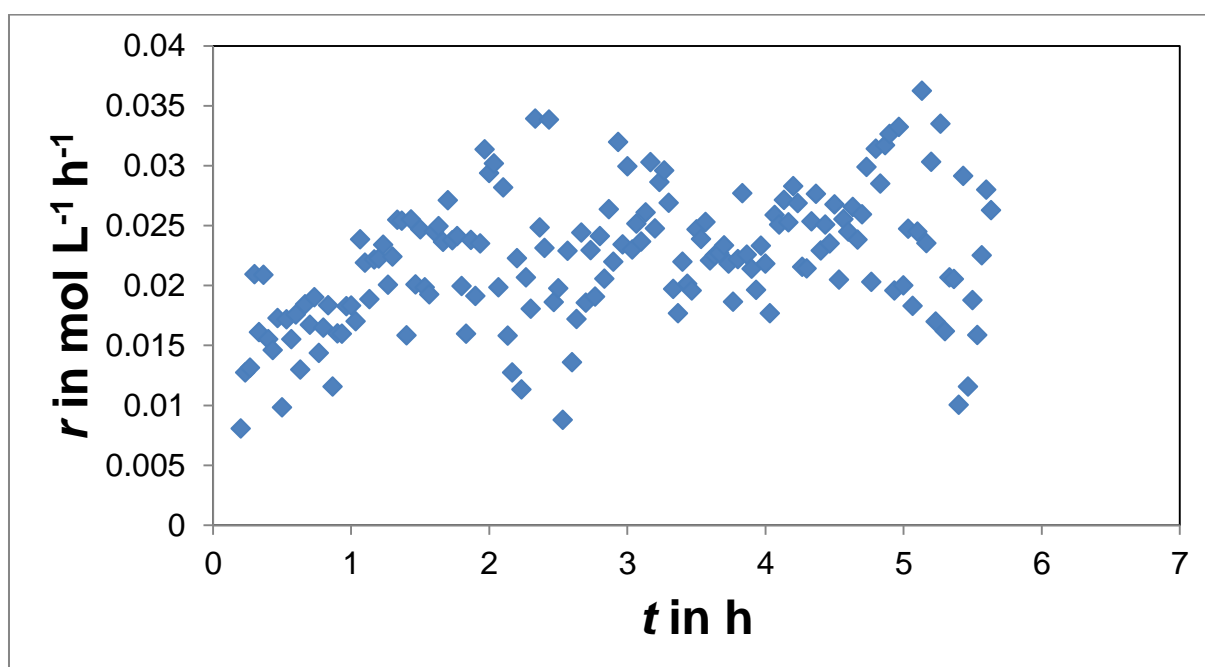
Figure 24: Reaction rate profiles of the product computed via numerical differentiation with an interval length of 12 min at 90 °C (Exp. No. OHL-057). In this experiment, the critical ionic liquid concentration has not been reached in reaction time.
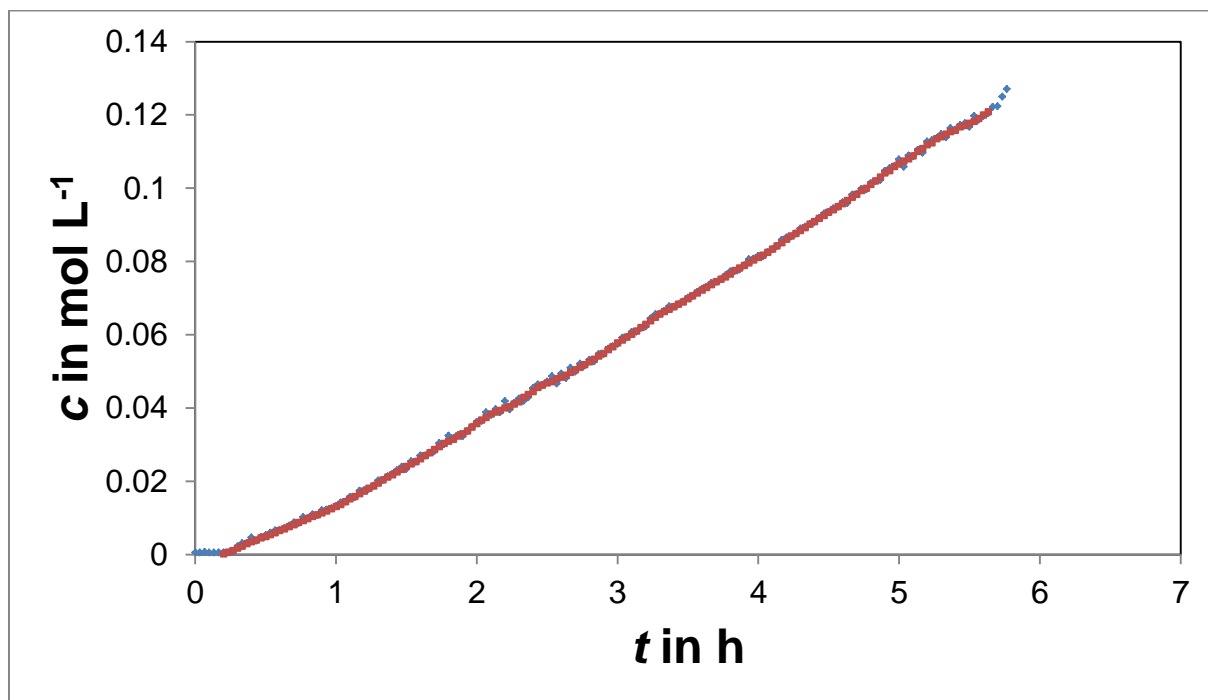
Figure 25: Concentration profile of the product (blue) compared with the re-integrated reaction rate of Fig. 24 (red). The similar shape of both graphs confirms the correctness of the numerical differentiation.
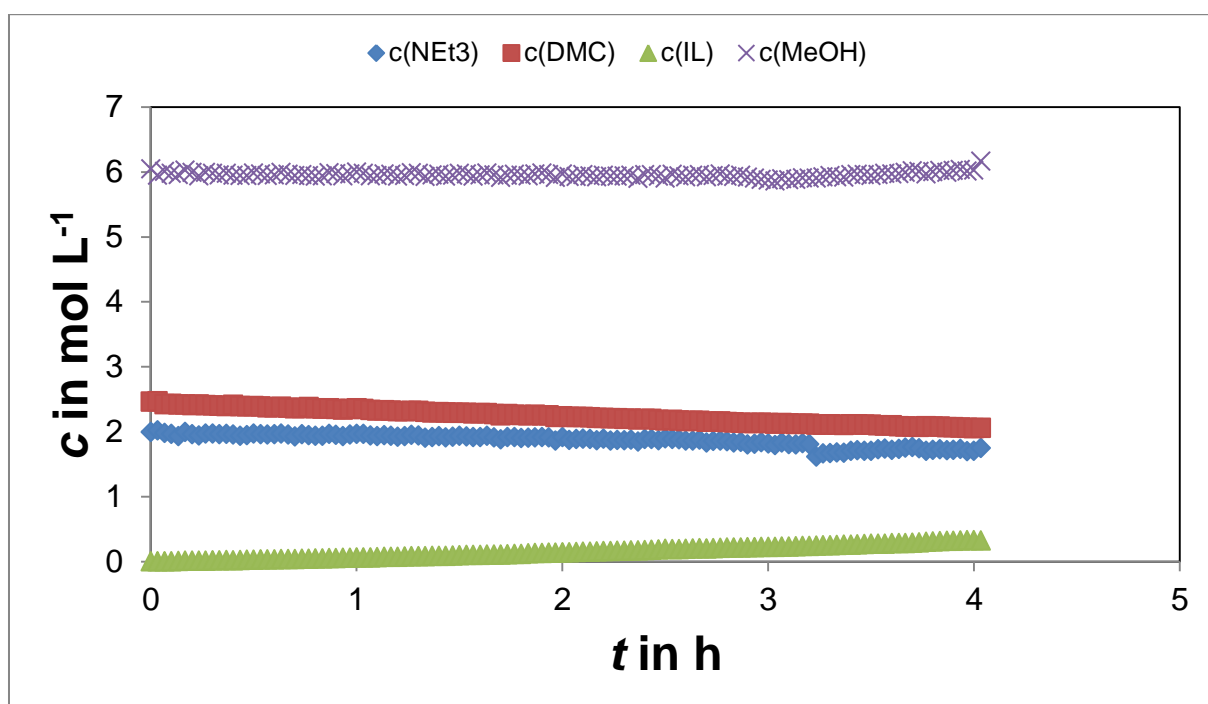
Figure 26: Concentration profiles of solvent, substrates and product determined via Peak Integration at 105 °C (Exp. No. OHL-069). The fluctuation of the methanol concentration at 3 h indicates a phase change. The discontinuity in the triethylamine profile at about 3.2 h corresponds to refilling of liquid nitrogen which interferes with the relatively small signal of this compound.
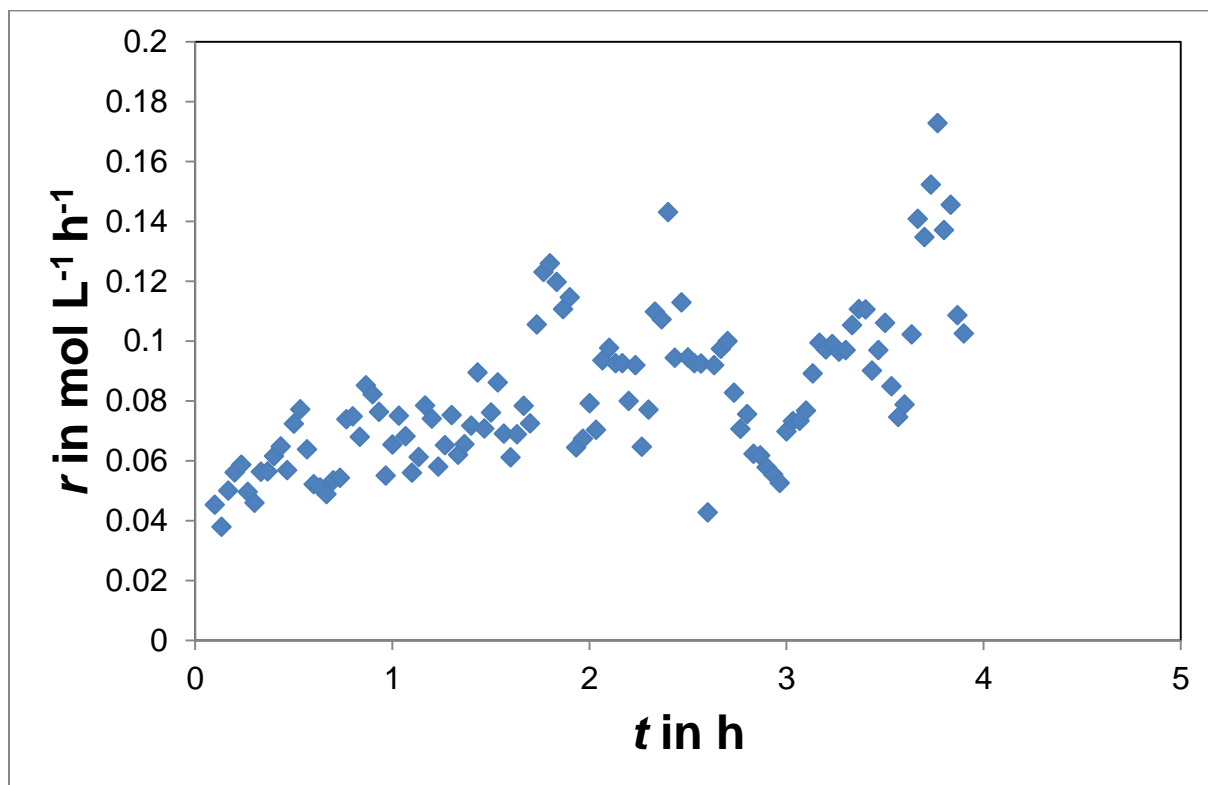
Figure 27: Reaction rate profiles of the product computed via numerical differentiation with an interval length of 12 min at 105 °C (Exp. No. OHL-069). In this experiment, the critical ionic liquid concentration has been reached at 2.9 h.
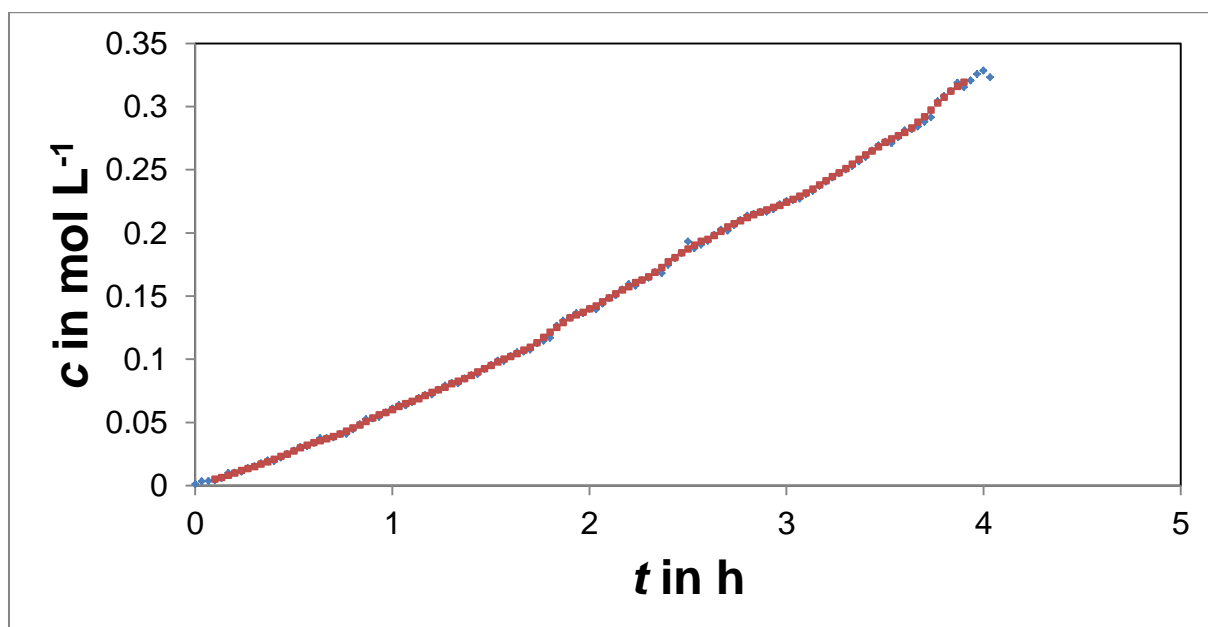
Figure 28: Concentration profile of the product (blue) compared with the re-integrated reaction rate of Fig. 27 (red). The similar shape of both graphs confirms the correctness of the numerical differentiation.
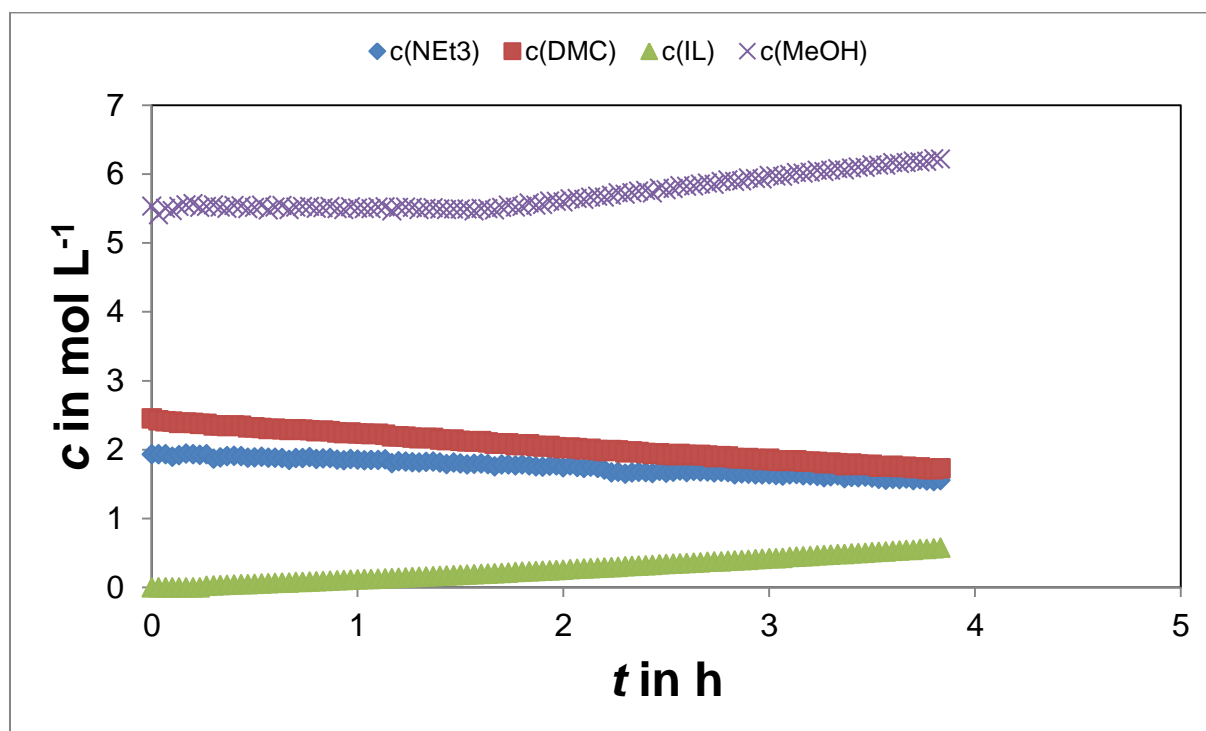
Figure 29: Concentration profiles of solvent, substrates and product determined via Peak Integration at 115 °C (Exp. No. OHL-068). The increase of methanol concentration at 1.8 h indicates a phase change. The discontinuity in the triethylamine profile at about 2.3 h corresponds to refilling of liquid nitrogen which interferes with the relatively small signal of this compound.
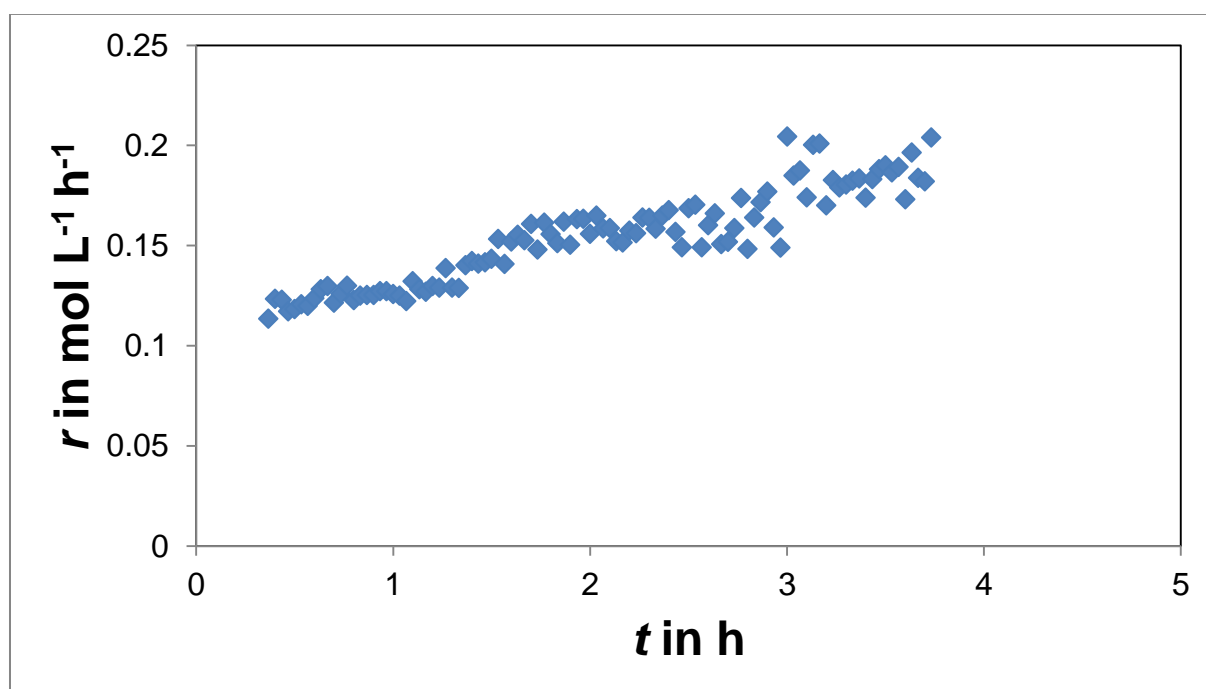
Figure 30: Reaction rate profiles of the product computed via numerical differentiation with an interval length of 12 min at 115 °C (Exp. No. OHL-068). In this experiment, the critical ionic liquid concentration has been reached at 1.8 h.
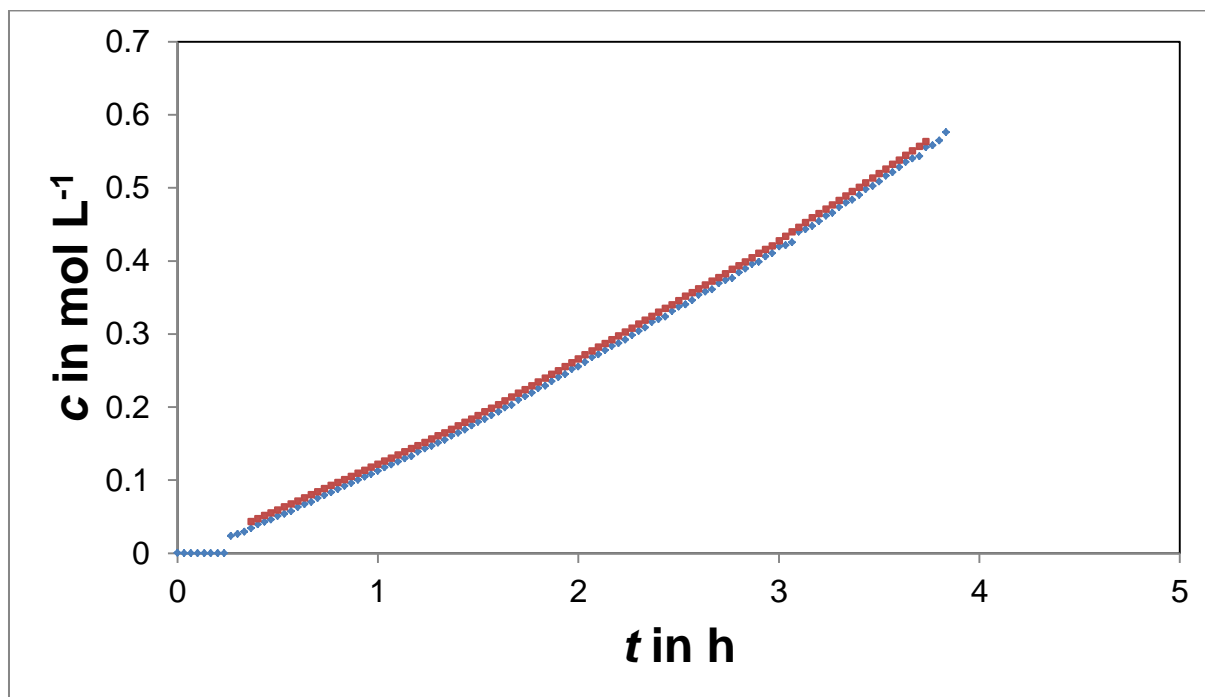
Figure 31: Concentration profile of the product (blue) compared with the re-integrated reaction rate of Fig. 30 (red). The similar shape of both graphs confirms the correctness of the numerical differentiation.
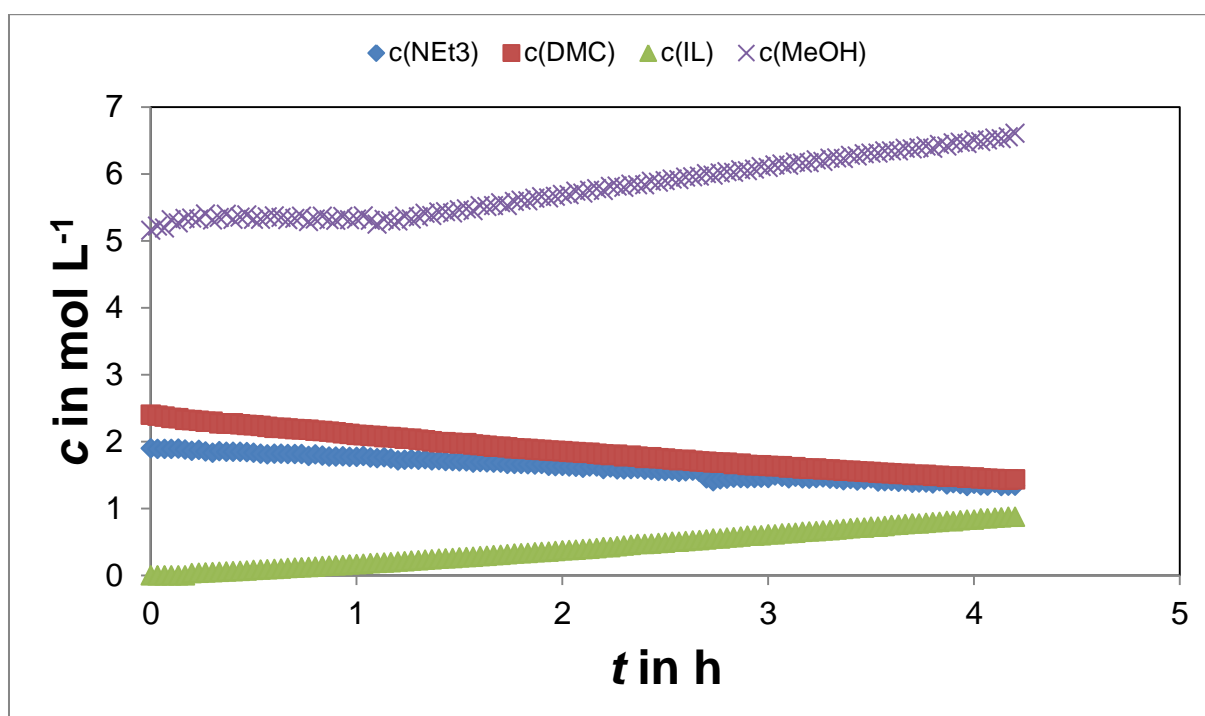
Figure 32: Concentration profiles of solvent, substrates and product determined via Peak Integration at 120 °C (Exp. No. OHL-067). The increase of methanol concentration at 1.2 h indicates a phase change. The discontinuity in the triethylamine profile at about 2.7 h corresponds to refilling of liquid nitrogen which interferes with the relatively small signal of this compound.
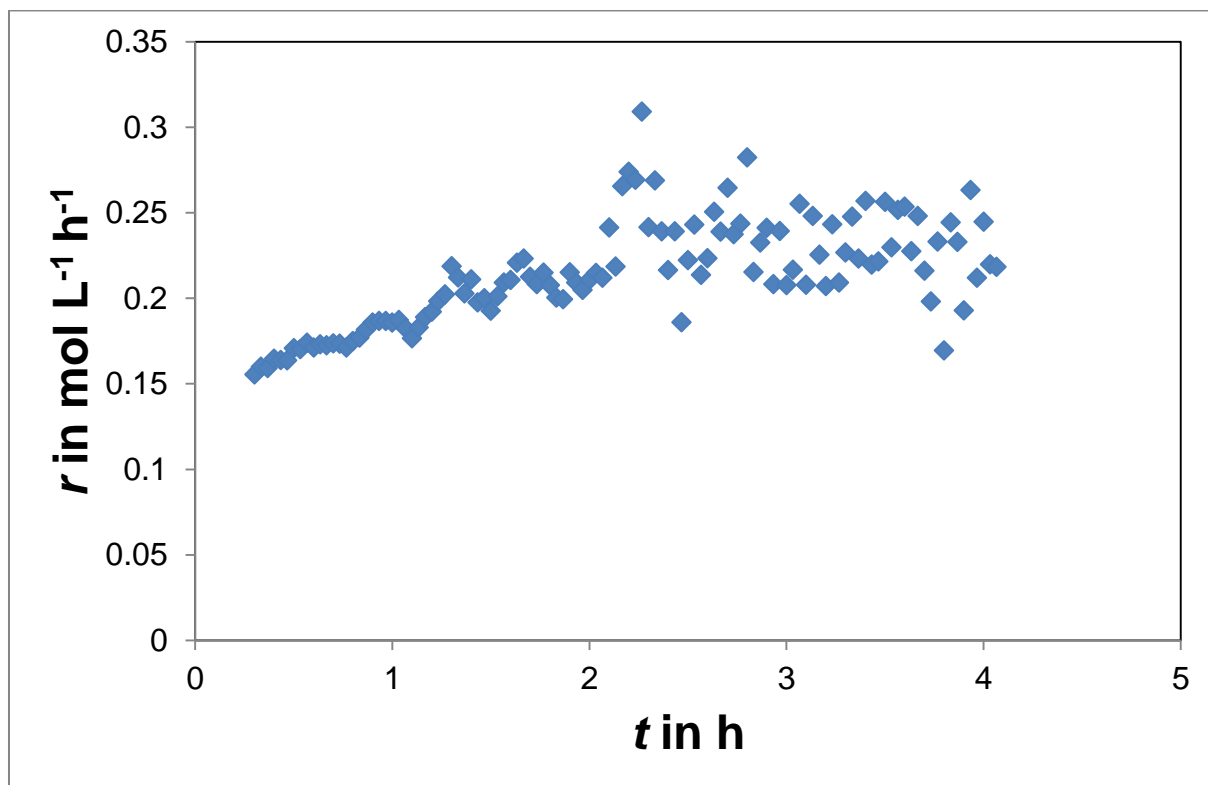
Figure 33: Reaction rate profiles of the product computed via numerical differentiation with an interval length of 12 min at 120 °C (Exp. No. OHL-067). In this experiment, the critical ionic liquid concentration has been reached at 1.2 h.
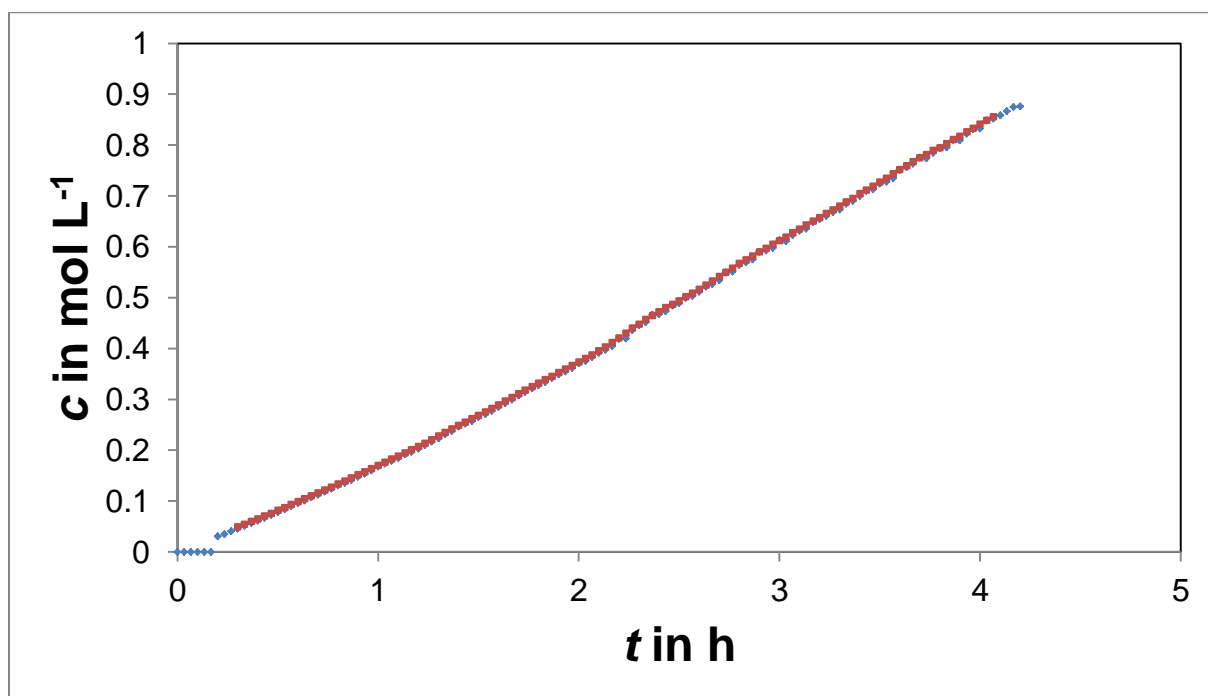
Figure 34: Concentration profile of the product (blue) compared with the re-integrated reaction rate of Fig. 33 (red). The similar shape of both graphs confirms the correctness of the numerical differentiation.
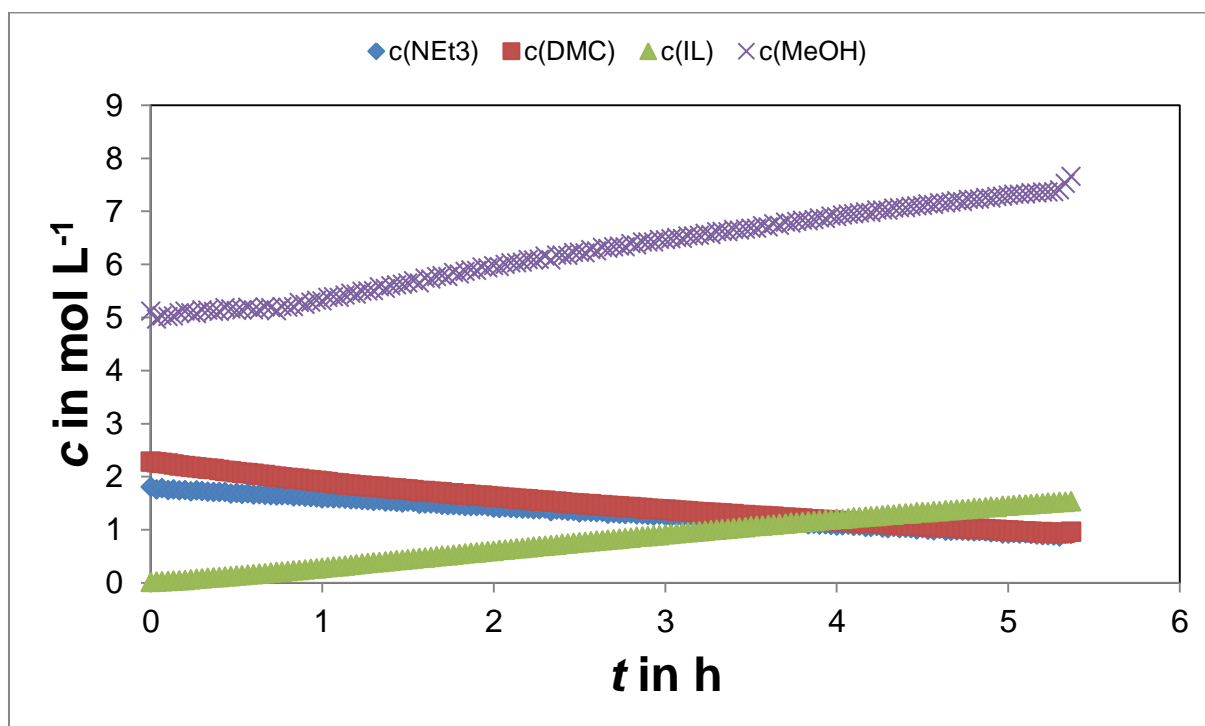
Figure 35: Concentration profiles of solvent, substrates and product determined via Peak Integration at 125 °C (Exp. No. OHL-056). The increase of methanol concentration at 1.1 h indicates a phase change.
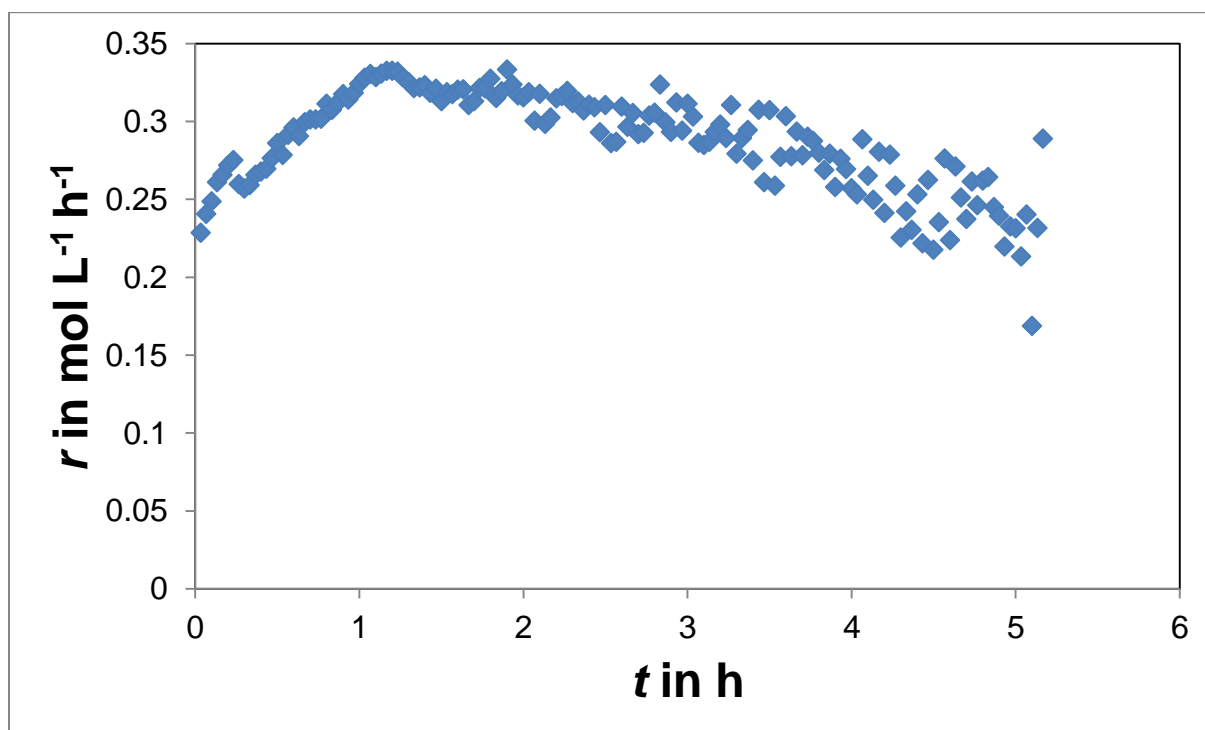
Figure 36: Reaction rate profiles of the product computed via numerical differentiation with an interval length of 15.6 min at 125 °C (Exp. No. OHL-056). In this experiment, the critical ionic liquid concentration has been reached at 1.1 h.
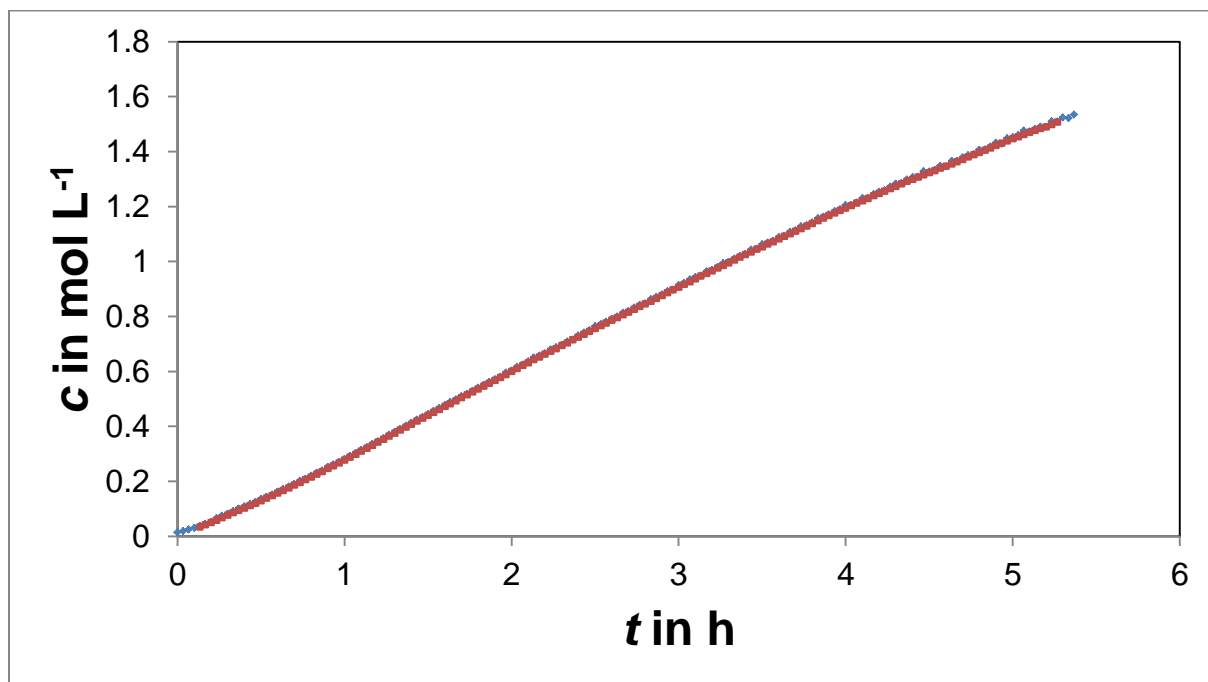
Figure 37: Concentration profile of the product (blue) compared with the re-integrated reaction rate of Fig. 36 (red). The similar shape of both graphs confirms the correctness of the numerical differentiation.
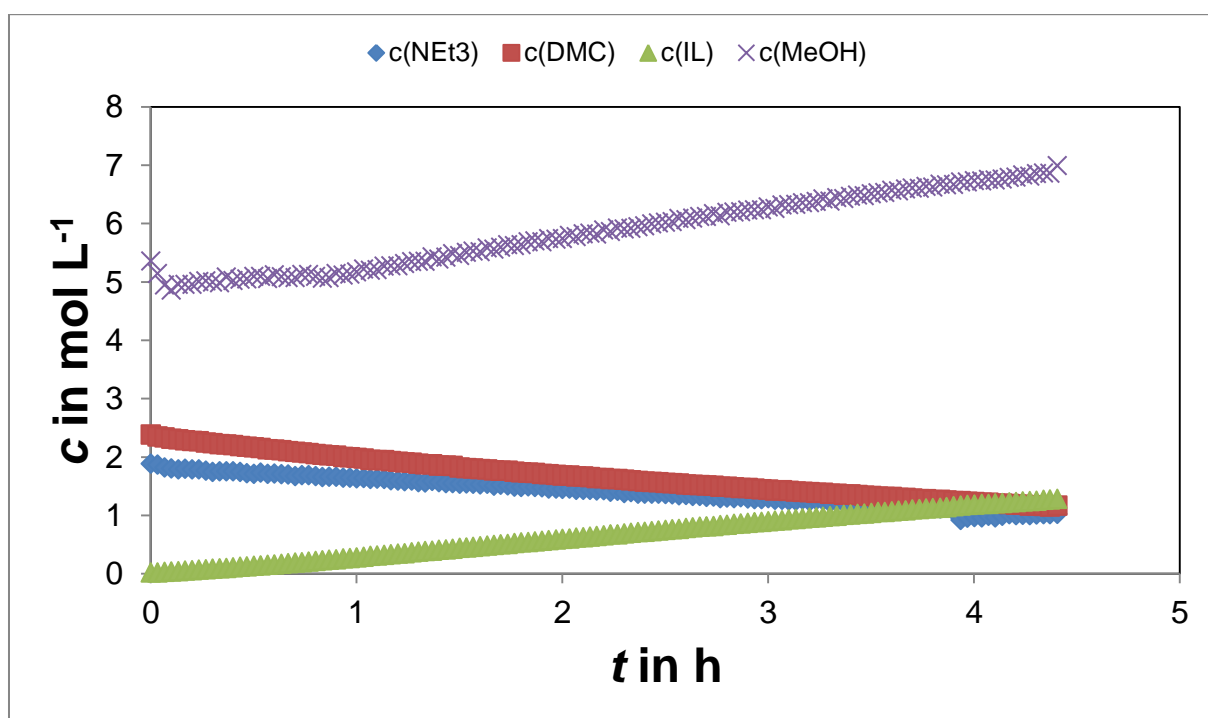
Figure 38: Concentration profiles of solvent, substrates and product determined via Peak Integration at 125 °C (Exp. No. OHL-064). The increase of methanol concentration at 1.0 h indicates a phase change. The discontinuity in the triethylamine profile at about 3.9 h corresponds to refilling of liquid nitrogen which interferes with the relatively small signal of this compound.
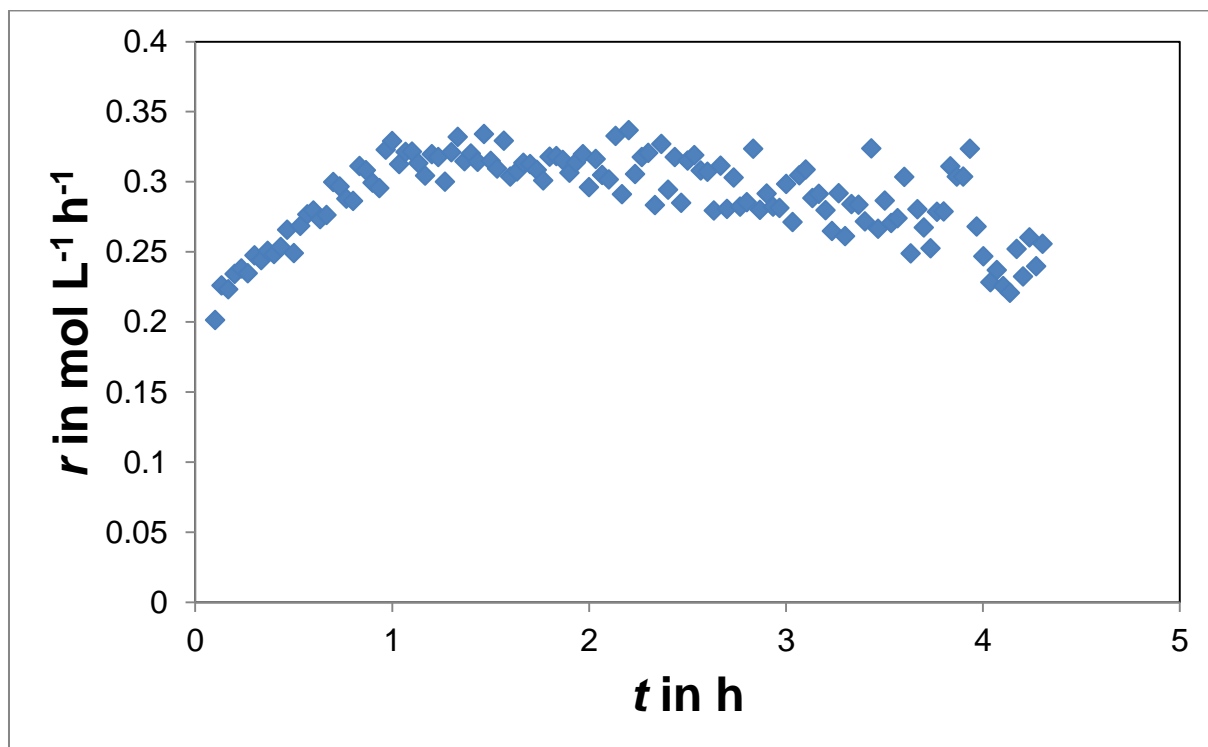
Figure 39: Reaction rate profiles of the product computed via numerical differentiation with an interval length of 12 min at 125 °C (Exp. No. OHL-064). In this experiment, the critical ionic liquid concentration has been reached at 1.0 h.
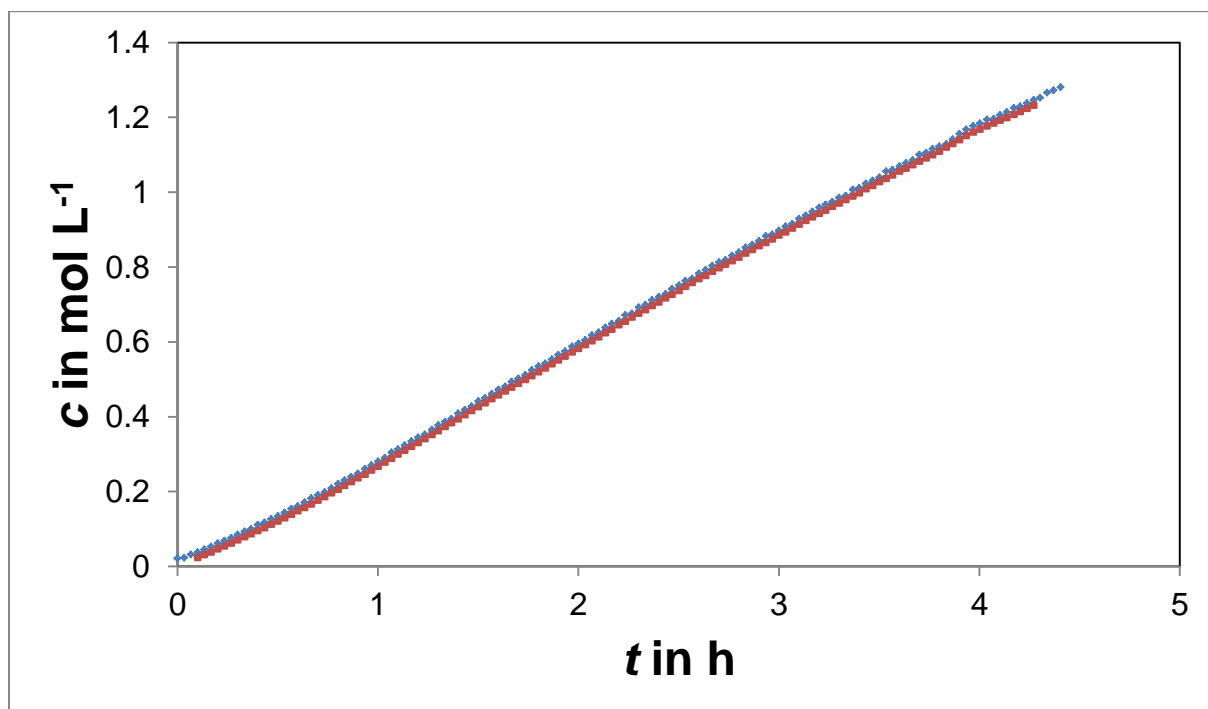
Figure 40: Concentration profile of the product (blue) compared with the re-integrated reaction rate of Fig. 39 (red). The similar shape of both graphs confirms the correctness of the numerical differentiation.
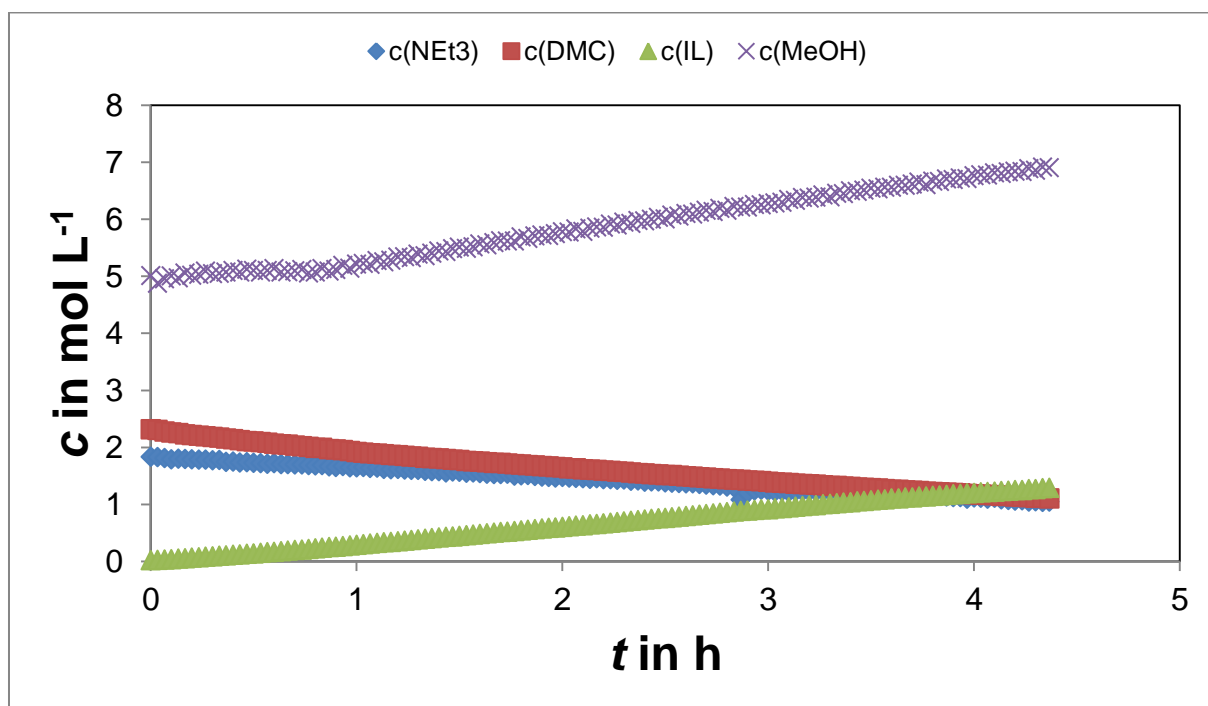
Figure 41: Concentration profiles of solvent, substrates and product determined via Peak Integration at 125 °C (Exp. No. OHL-066). The increase of methanol concentration at 0.8 h indicates a phase change. The discontinuity in the triethylamine profile at about 2.8 h corresponds to refilling of liquid nitrogen which interferes with the relatively small signal of this compound.
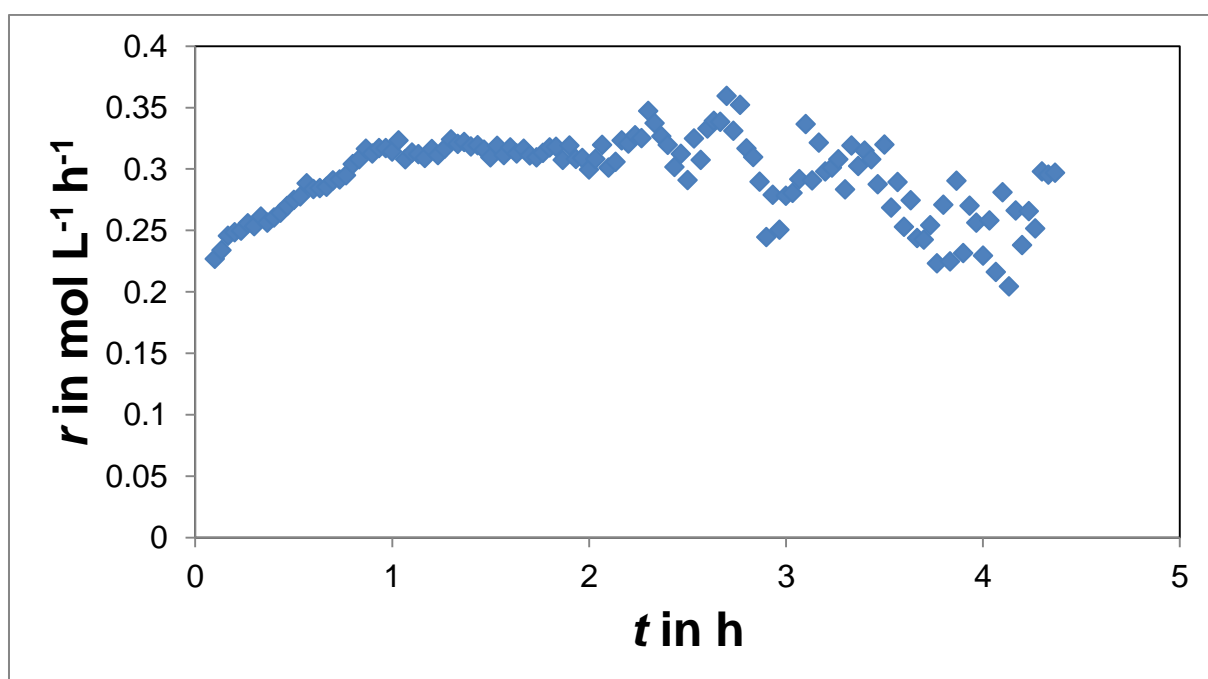
Figure 42: Reaction rate profiles of the product computed via numerical differentiation with an interval length of 12 min at 125 °C (Exp. No. OHL-066). In this experiment, the critical ionic liquid concentration has been reached at 0.8 h.
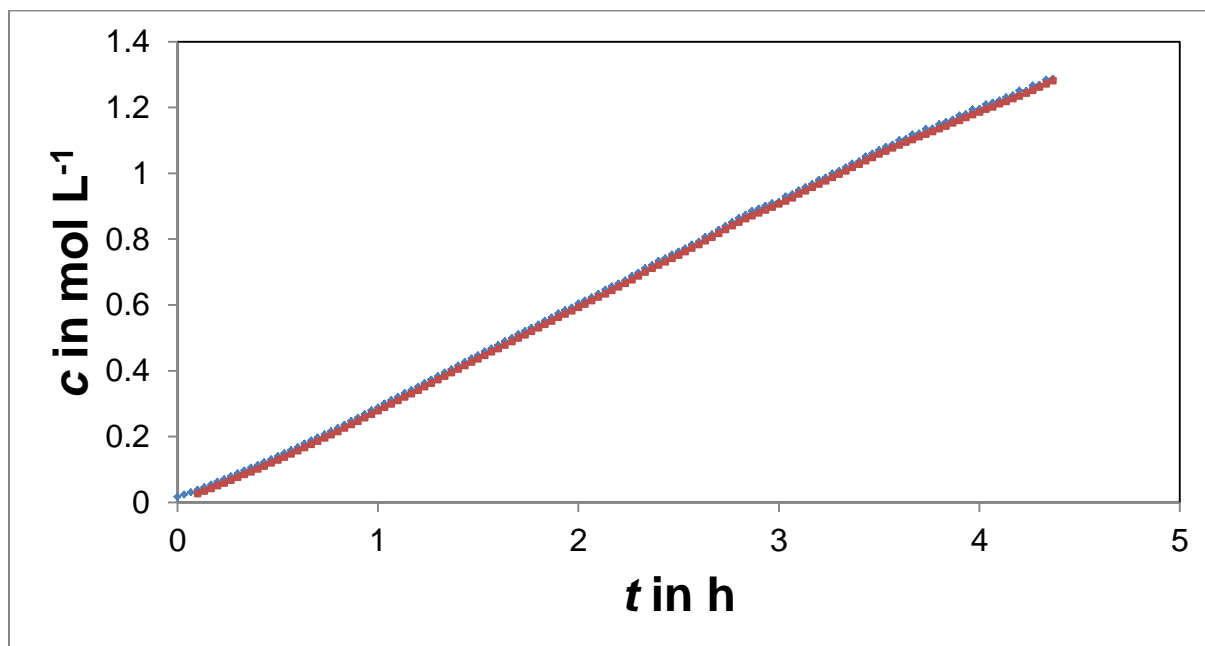
Figure 43: Concentration profile of the product (blue) compared with the re-integrated reaction rate of Fig. 42 (red). The similar shape of both graphs confirms the correctness of the numerical differentiation.
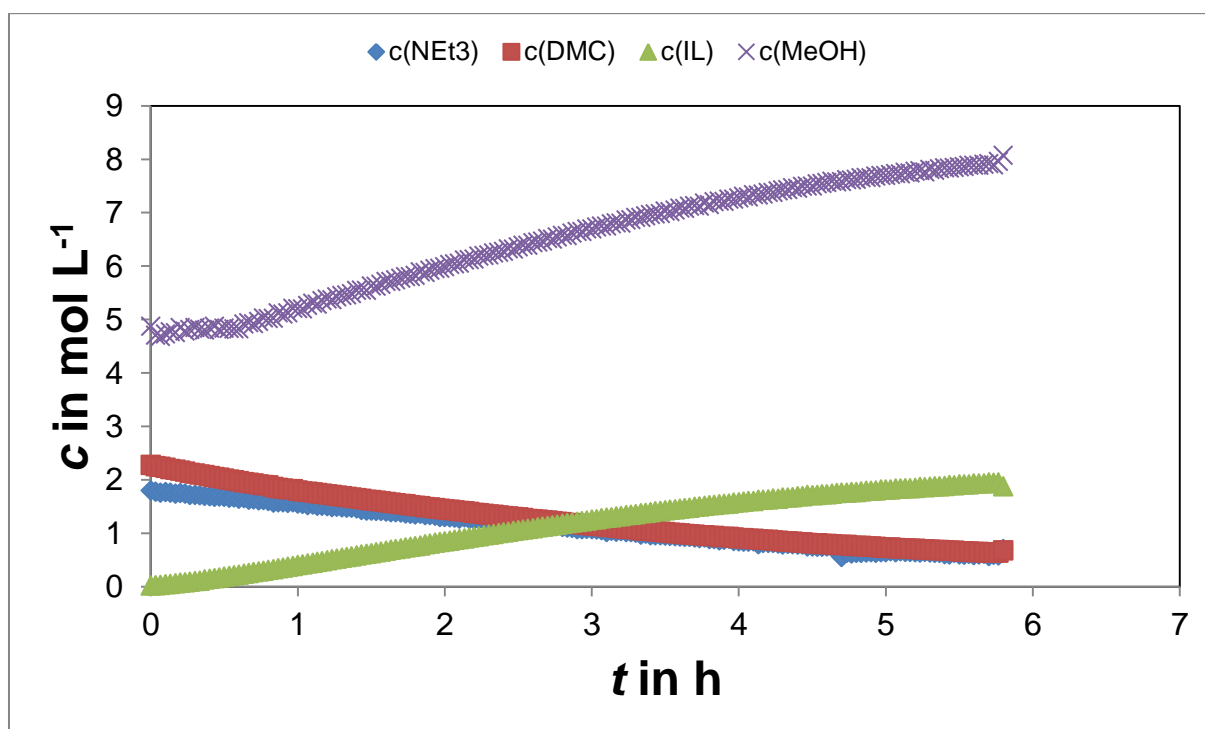
Figure 44: Concentration profiles of solvent, substrates and product determined via Peak Integration at 130 °C (Exp. No. OHL-060). The increase of methanol concentration at 0.7 h indicates a phase change. The discontinuity in the triethylamine profile at about 4.6 h corresponds to refilling of liquid nitrogen which interferes with the relatively small signal of this compound.
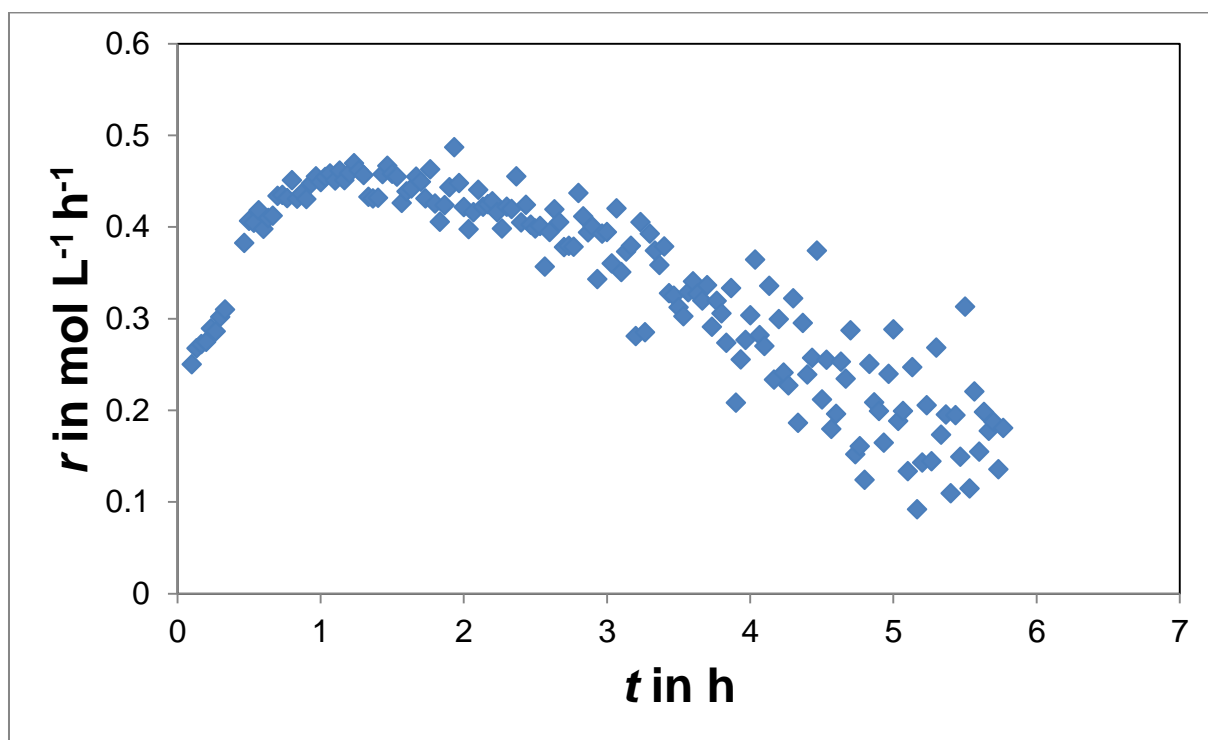
Figure 45: Reaction rate profiles of the product computed via numerical differentiation with an interval length of 6 min at 130 °C (Exp. No. OHL-060). In this experiment, the critical ionic liquid concentration has been reached at 0.7 h.
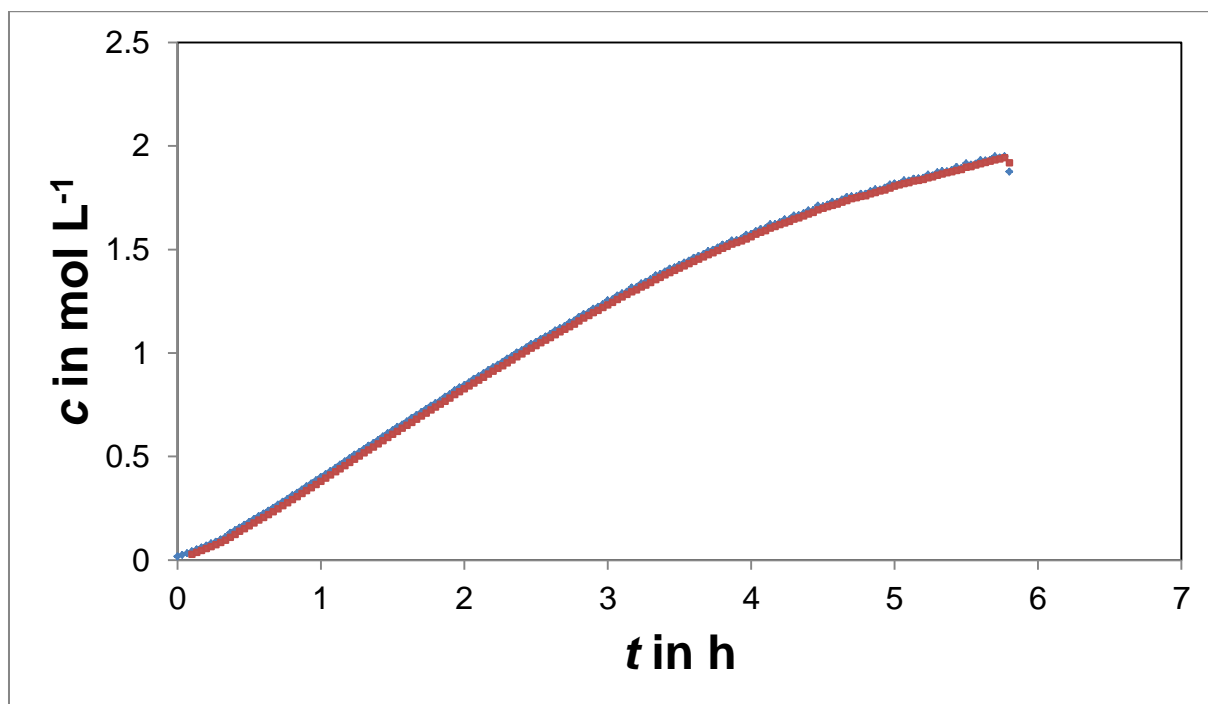
Figure 46: Concentration profile of the product (blue) compared with the re-integrated reaction rate of Fig. 45 (red). The similar shape of both graphs confirms the correctness of the numerical differentiation.
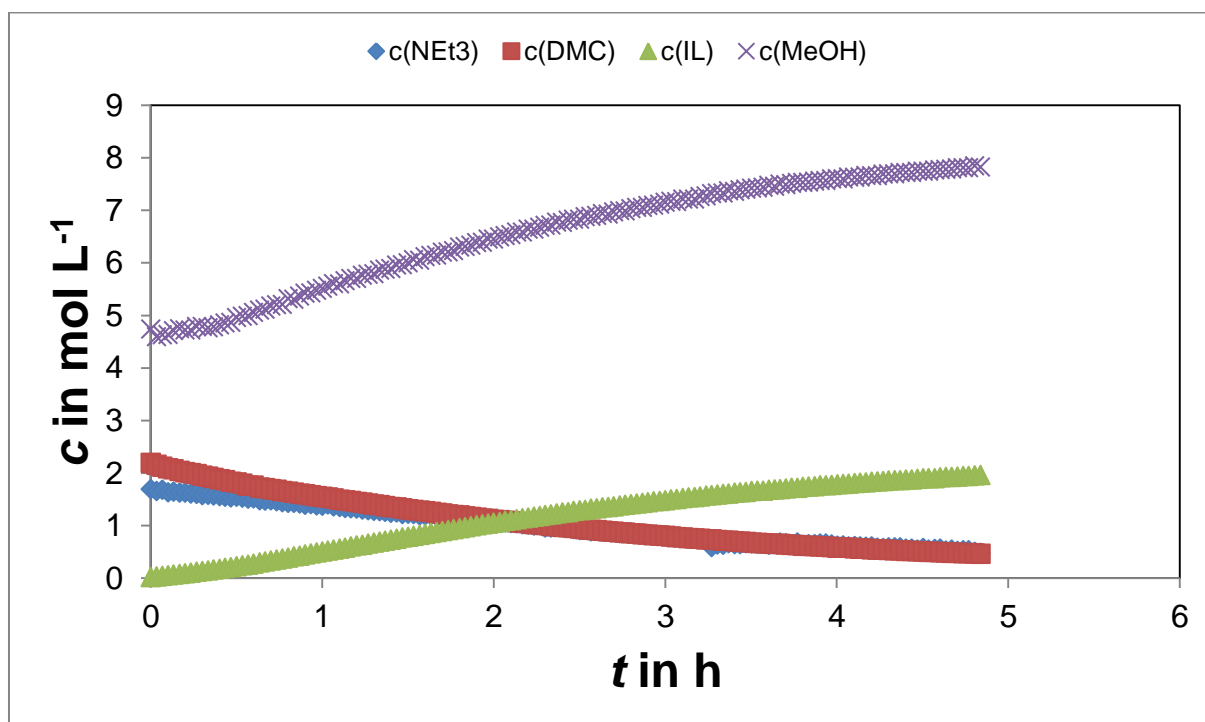
Figure 47: Concentration profiles of solvent, substrates and product determined via Peak Integration at 135 °C (Exp. No. OHL-054). The increase of methanol concentration at 0.6 h indicates a phase change. The discontinuity in the triethylamine profile at about 3.3 h corresponds to refilling of liquid nitrogen which interferes with the relatively small signal of this compound.
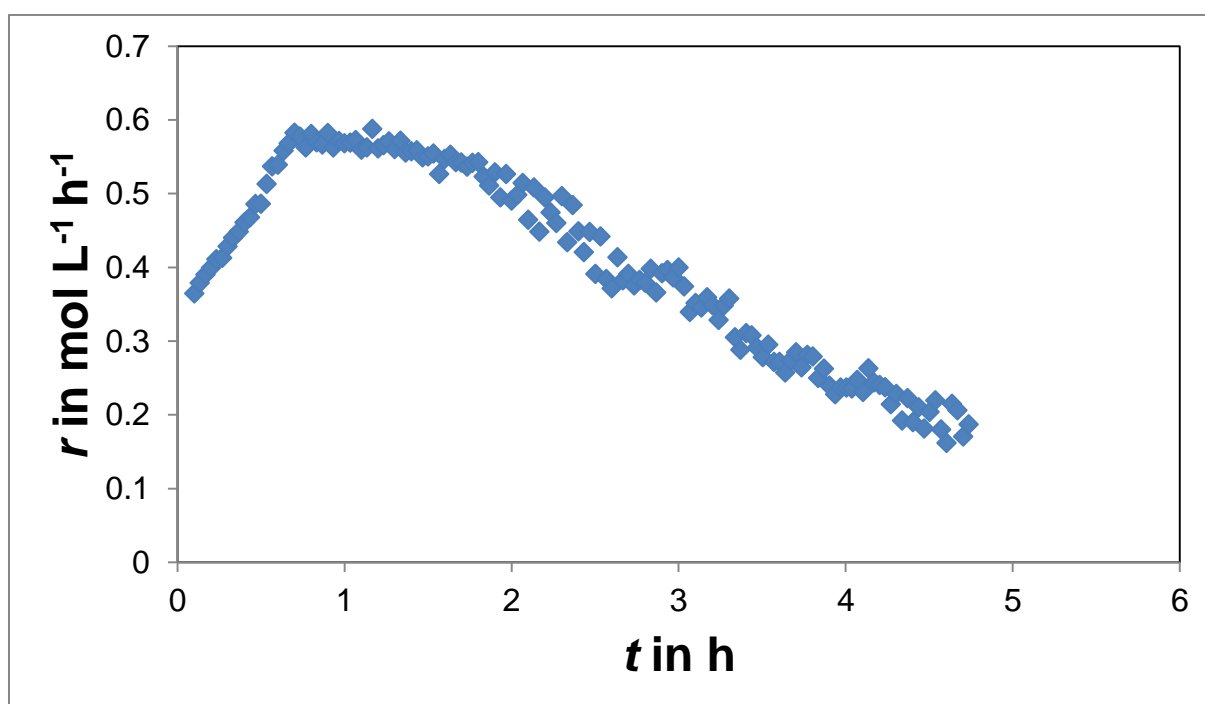
Figure 48: Reaction rate profiles of the product computed via numerical differentiation with an interval length of 12 min at 135 °C (Exp. No. OHL-054). In this experiment, the critical ionic liquid concentration has been reached at 0.6 h.
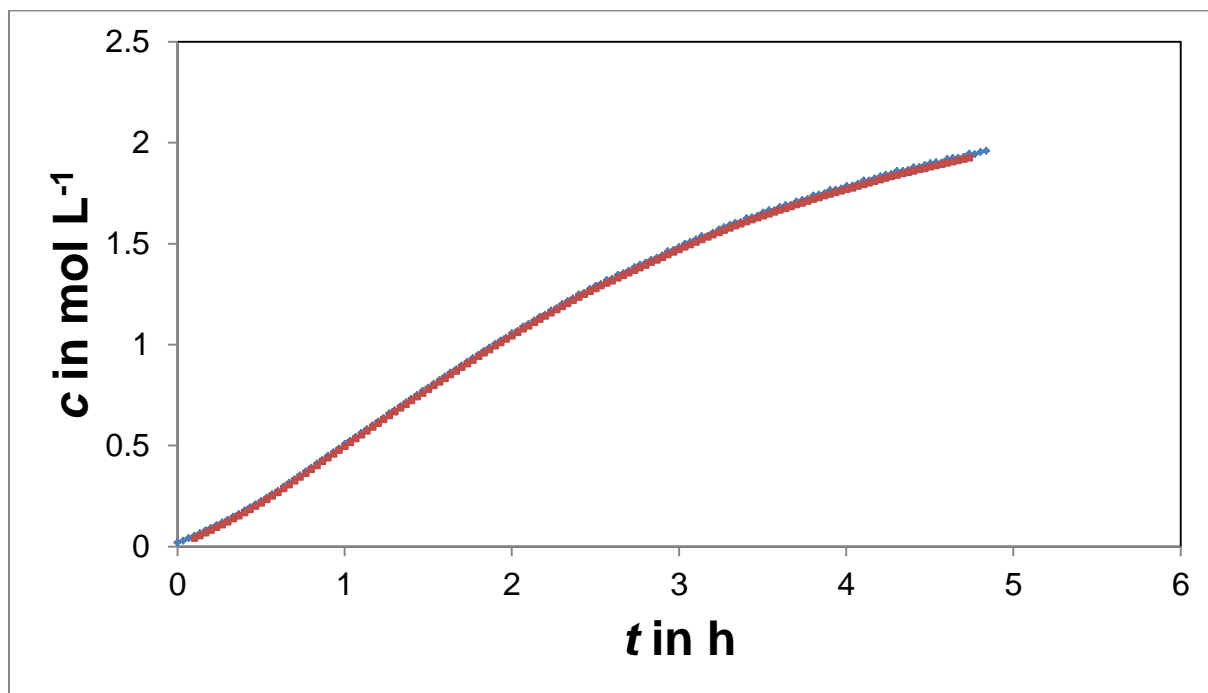
Figure 49: Concentration profile of the product (blue) compared with the re-integrated reaction rate of Fig. 48 (red). The similar shape of both graphs confirms the correctness of the numerical differentiation.
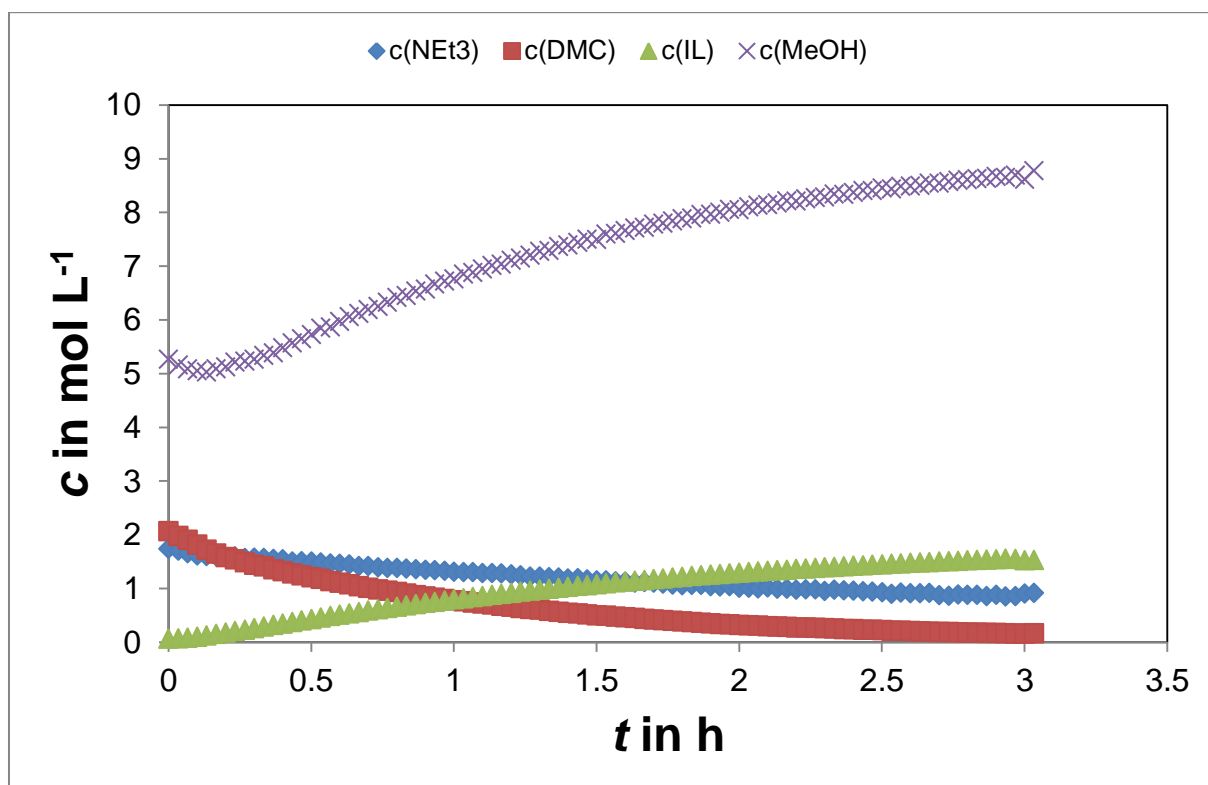
Figure 50: Concentration profiles of solvent, substrates and product determined via Peak Integration at 140 °C (Exp. No. OHL-061). The increase of methanol concentration at 0.3 h indicates a phase change.
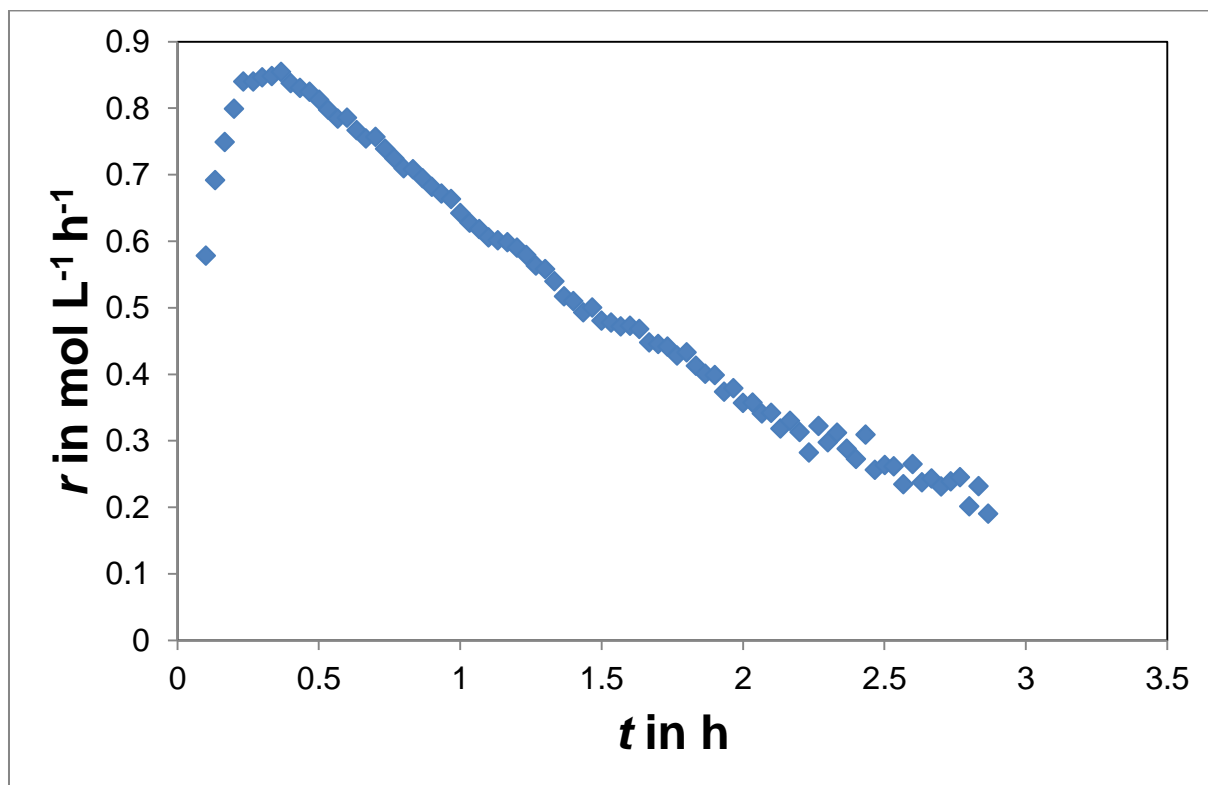
Figure 51: Reaction rate profiles of the product computed via numerical differentiation with an interval length of 12 min at 140 °C (Exp. No. OHL-061). In this experiment, the critical ionic liquid concentration has been reached at 0.7 h.
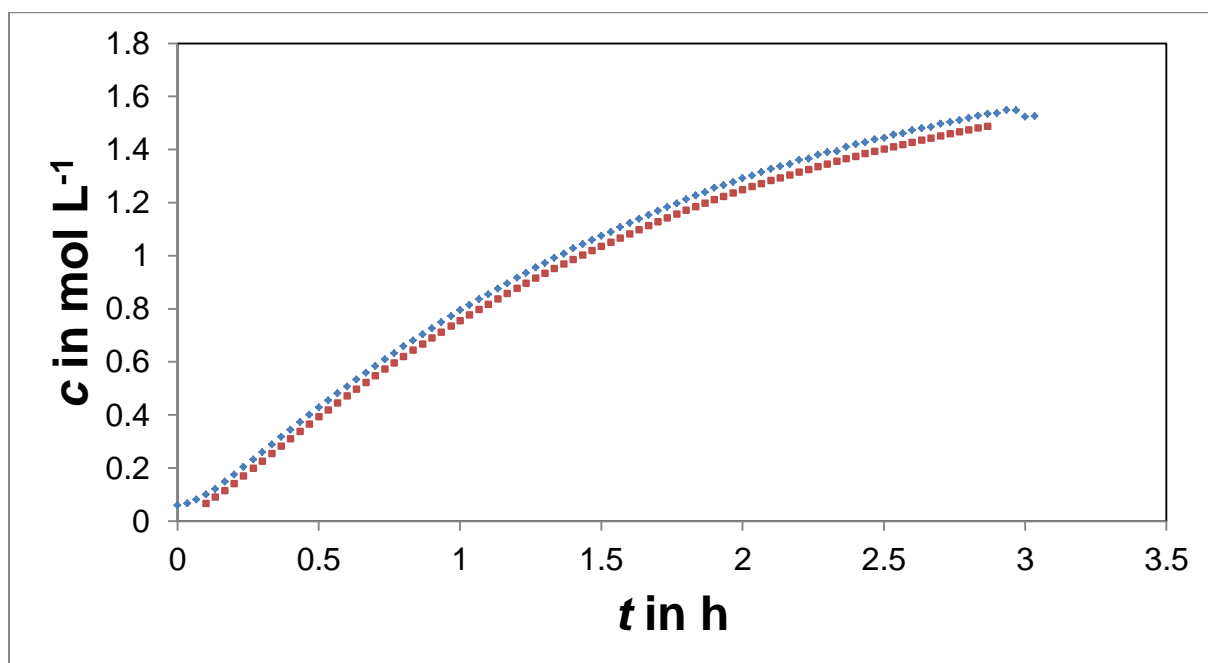
Figure 52: Concentration profile of the product (blue) compared with the re-integrated reaction rate of Fig. 51 (red). The similar shape of both graphs confirms the correctness of the numerical differentiation.

3.3   Kinetic Modeling

3.3.1   Parallel Reaction Model

The reaction rate coefficient k_{app} has been calculated by dividing the reaction rate r by the substrate concentrations $c(DMC)$ and $c(NEt_3)$ (Eq.1).

$$k_{app} = \frac{r}{c(DMC) \cdot c(NEt_3)} \qquad (1)$$
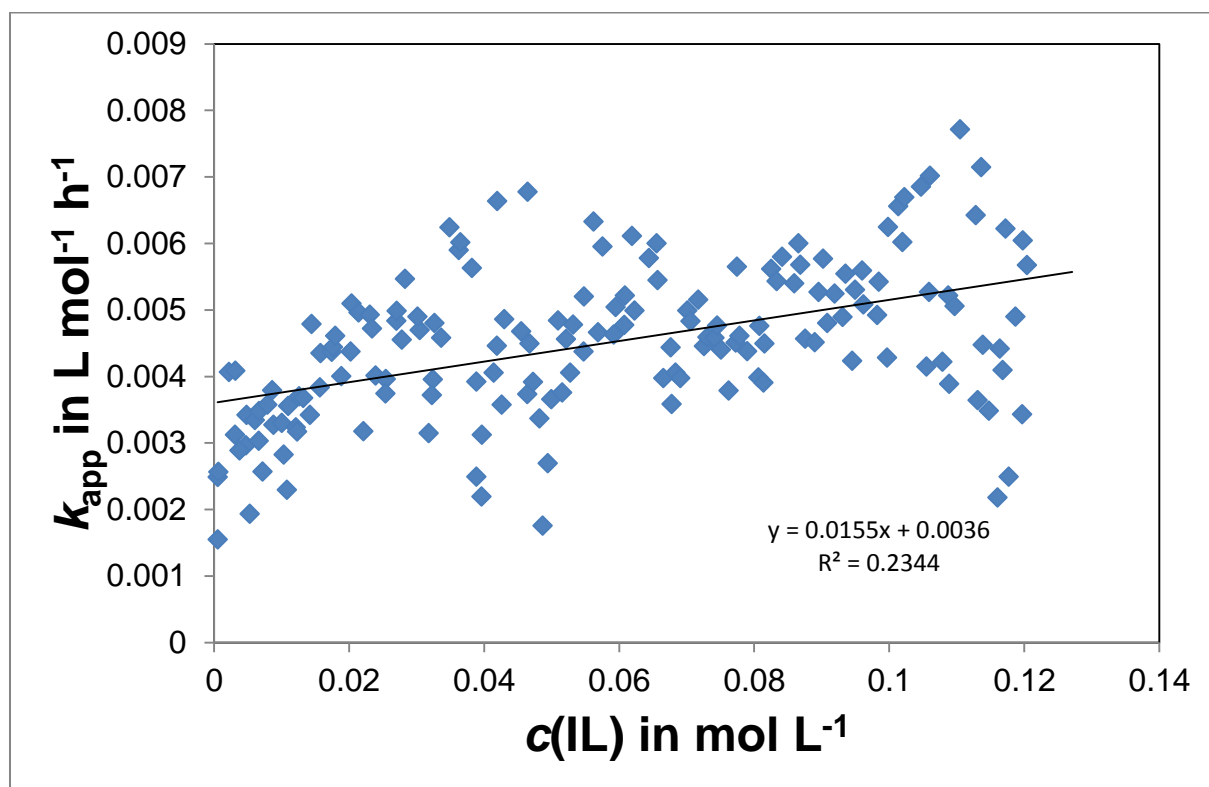
Figure 53: Plot of the reaction rate coefficient k_{app} vs. the product concentration $c(IL)$ at 90 °C (Exp. No. OHL-057). The data points have been endowed with a linear fit function.
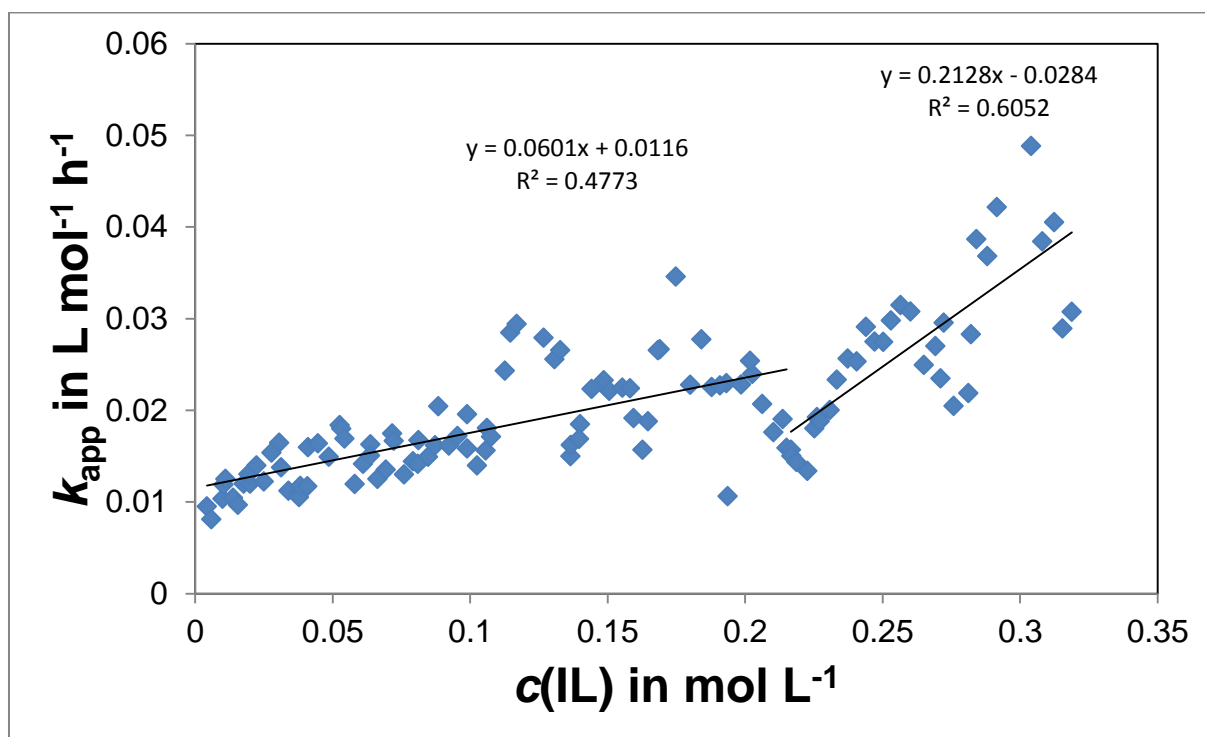
Figure 54: Plot of the reaction rate coefficient k_{app} vs. the product concentration c(IL) at 105 °C (Exp. No. OHL-069). The data points have been endowed with a linear fit function for the sections before and after the critical concentration.
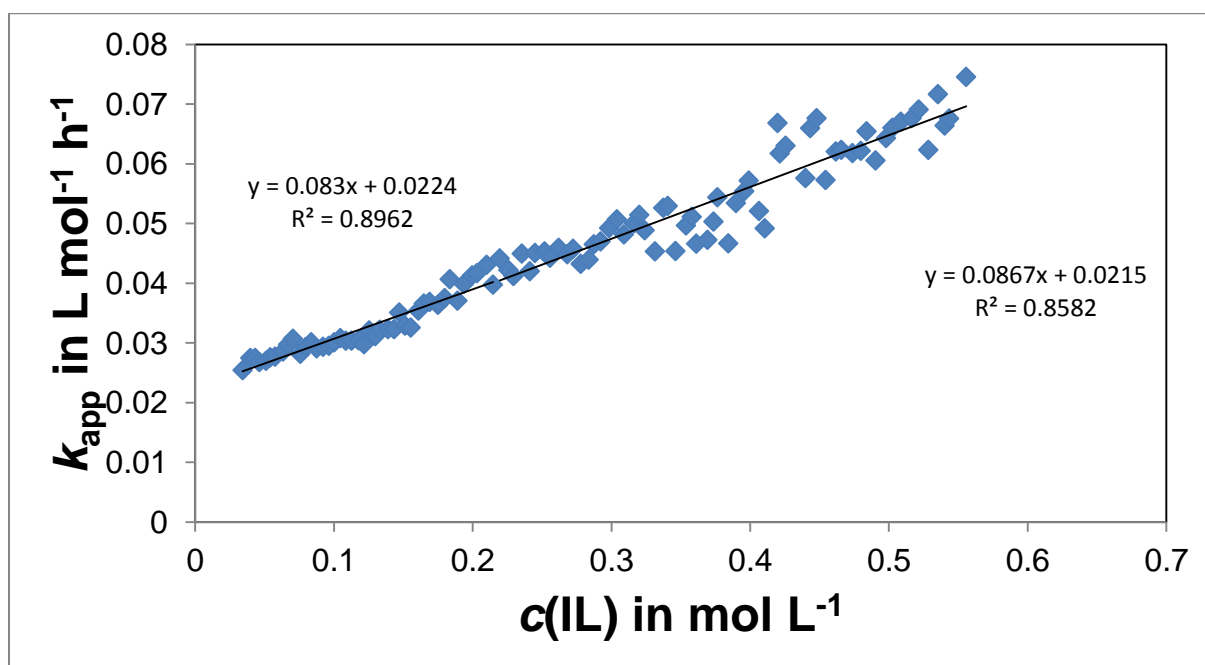
Figure 55: Plot of the reaction rate coefficient k_{app} vs. the product concentration c(IL) at 115 °C (Exp. No. OHL-068). The data points have been endowed with a linear fit function for the sections before and after the critical concentration. A positive curvature is apparent before and after the critical con-centration.
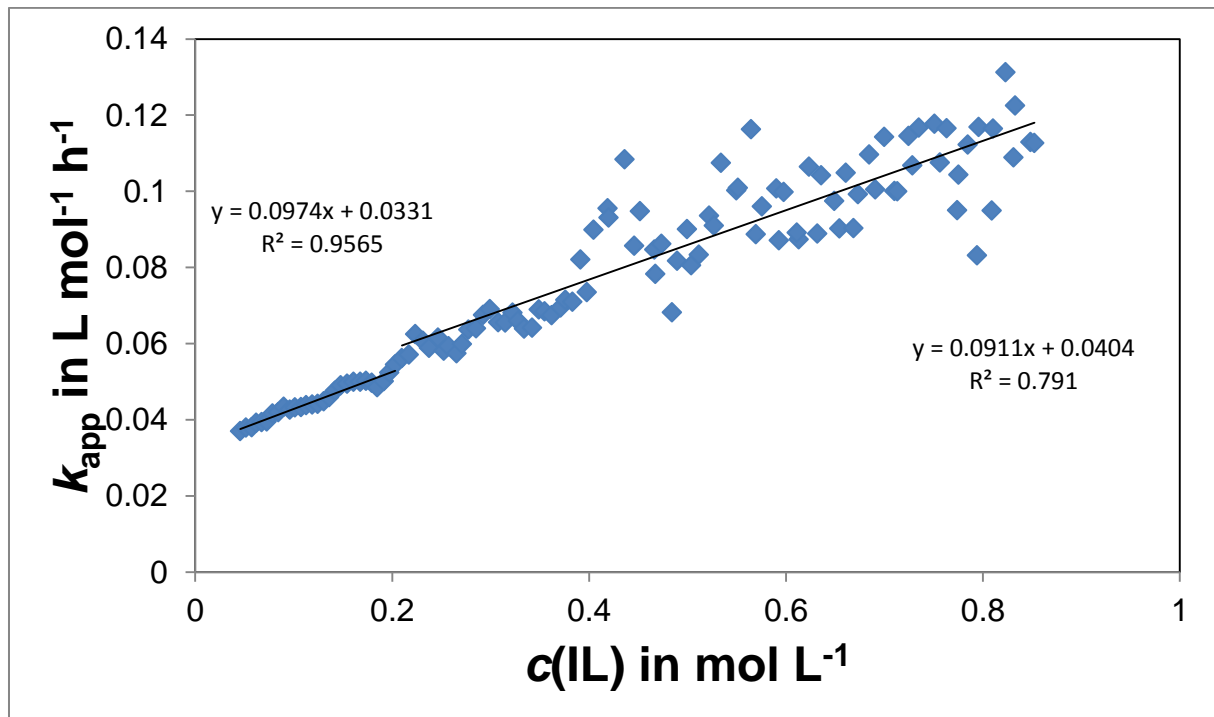
Figure 56: Plot of the reaction rate coefficient k_{app} vs. the product concentration c(IL) at 120 °C (Exp. No. OHL-067). The data points have been endowed with a linear fit function for the sections before and after the critical concentration.
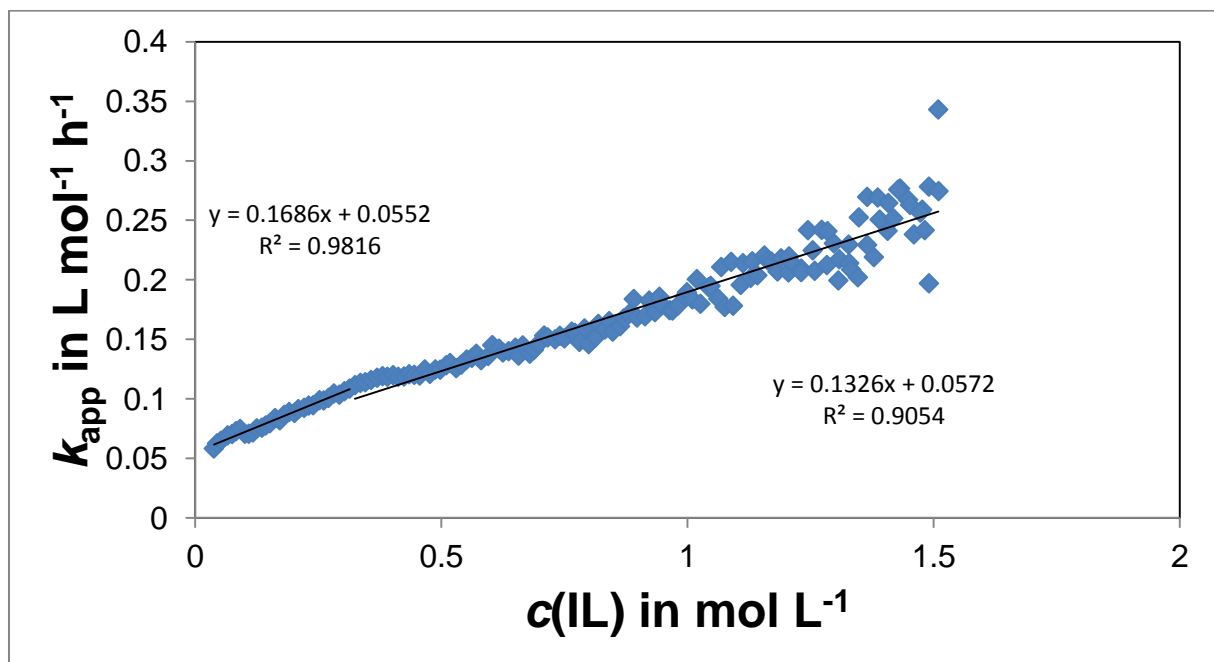
Figure 57: Plot of the reaction rate coefficient k_{app} vs. the product concentration c(IL) at 125 °C (Exp. No. OHL-056). The data points have been endowed with a linear fit function for the sections before and after the critical concentration.
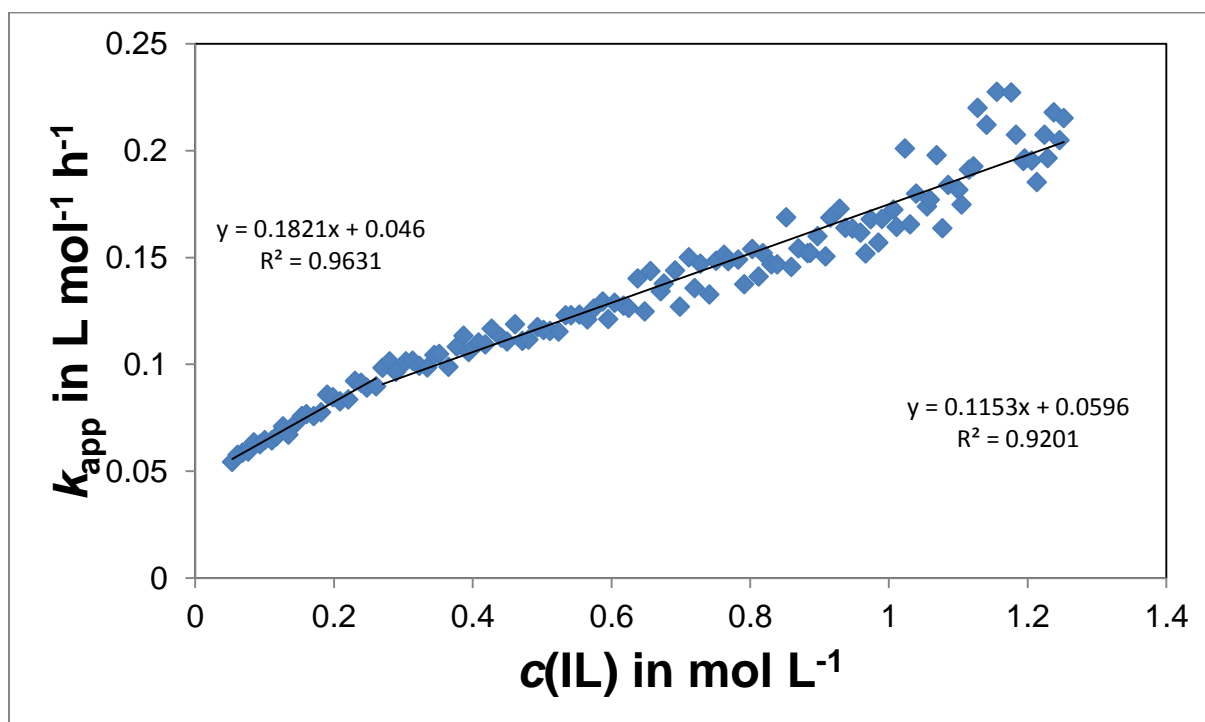
Figure 58: Plot of the reaction rate coefficient k_{app} vs. the product concentration c(IL) at 125 °C (Exp. No. OHL-064). The data points have been endowed with a linear fit function for the sections before and after the critical concentration.
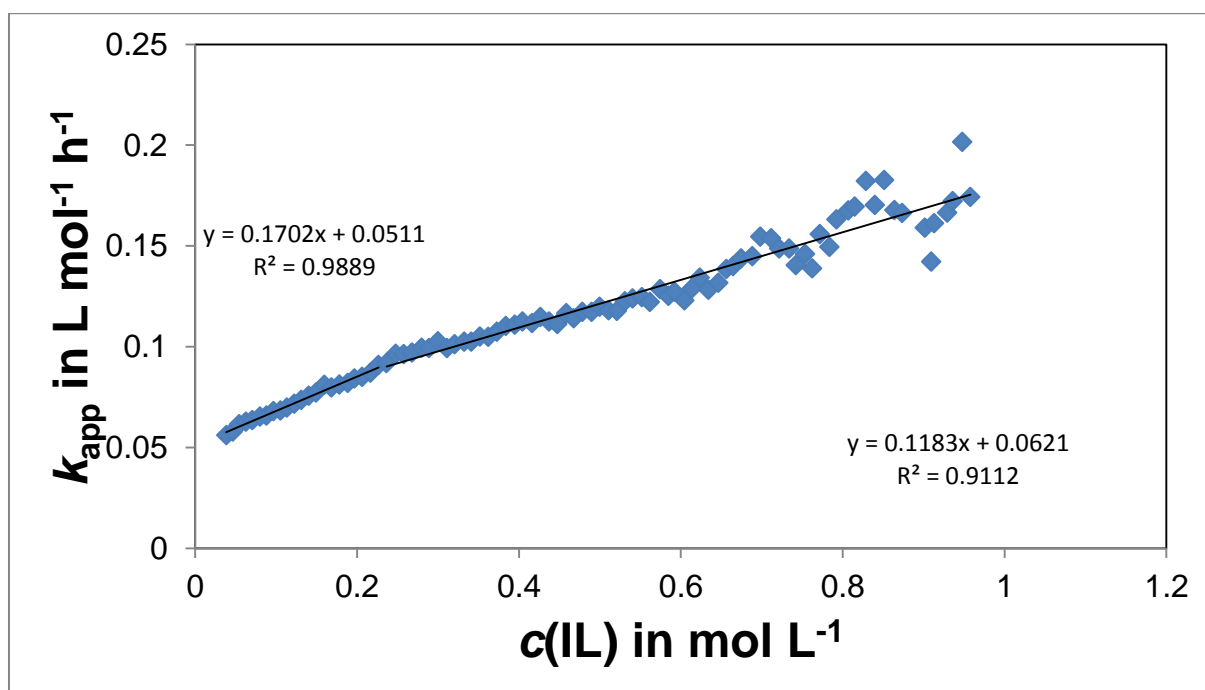
Figure 59: Plot of the reaction rate coefficient k_{app} vs. the product concentration c(IL) at 125 °C (Exp. No. OHL-066). The data points have been endowed with a linear fit function for the sections before and after the critical concentration.
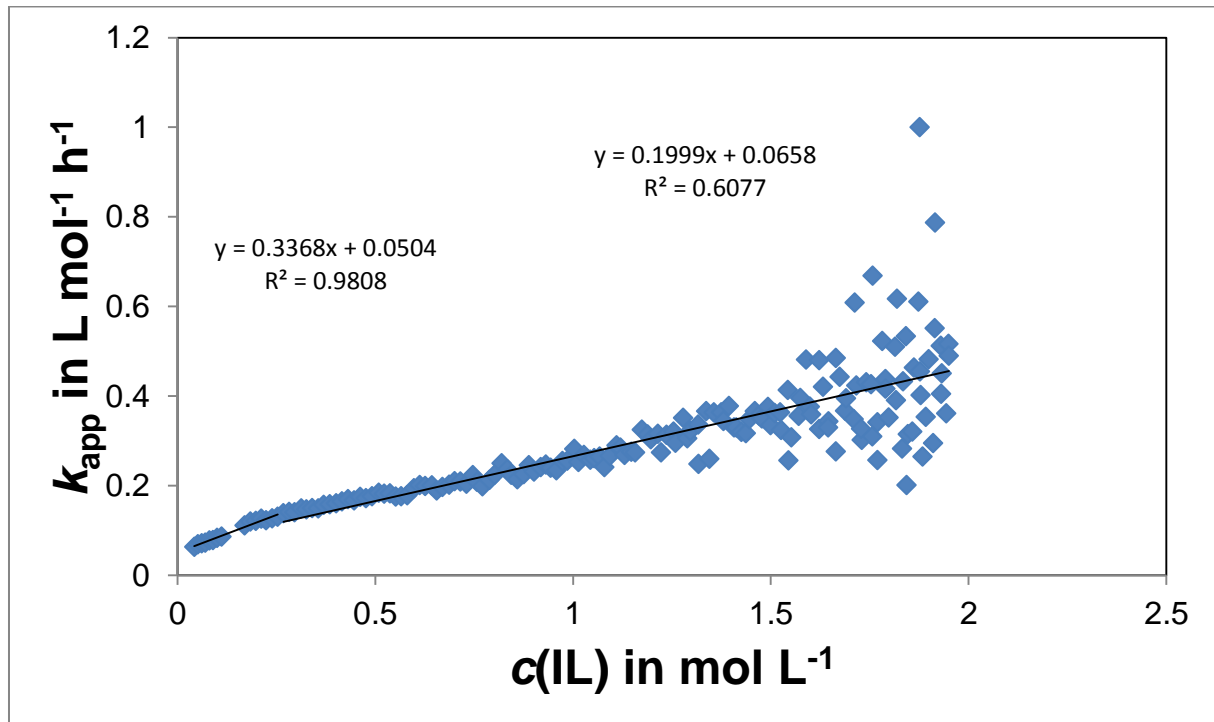
Figure 60: Plot of the reaction rate coefficient k_{app} vs. the product concentration c(IL) at 130 °C (Exp. No. OHL-060). The data points have been endowed with a linear fit function for the sections before and after the critical concentration.
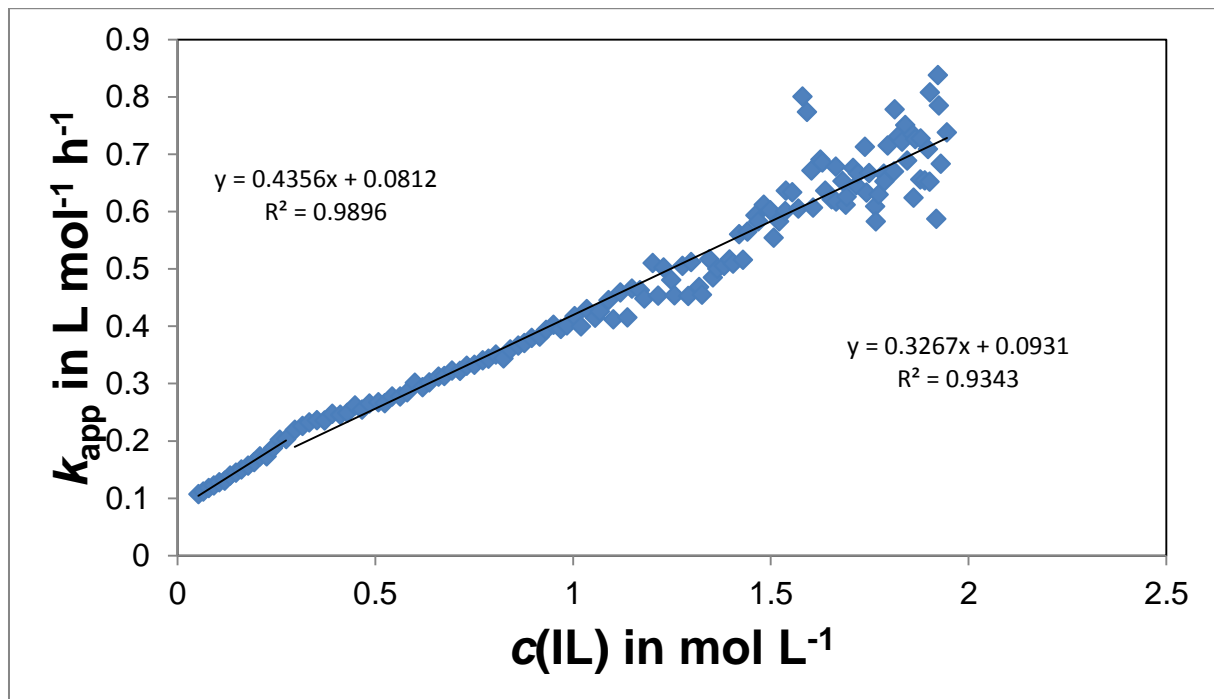
Figure 61: Plot of the reaction rate coefficient k_{app} vs. the product concentration c(IL) at 135 °C (Exp. No. OHL-054). The data points have been endowed with a linear fit function for the sections before and after the critical concentration.
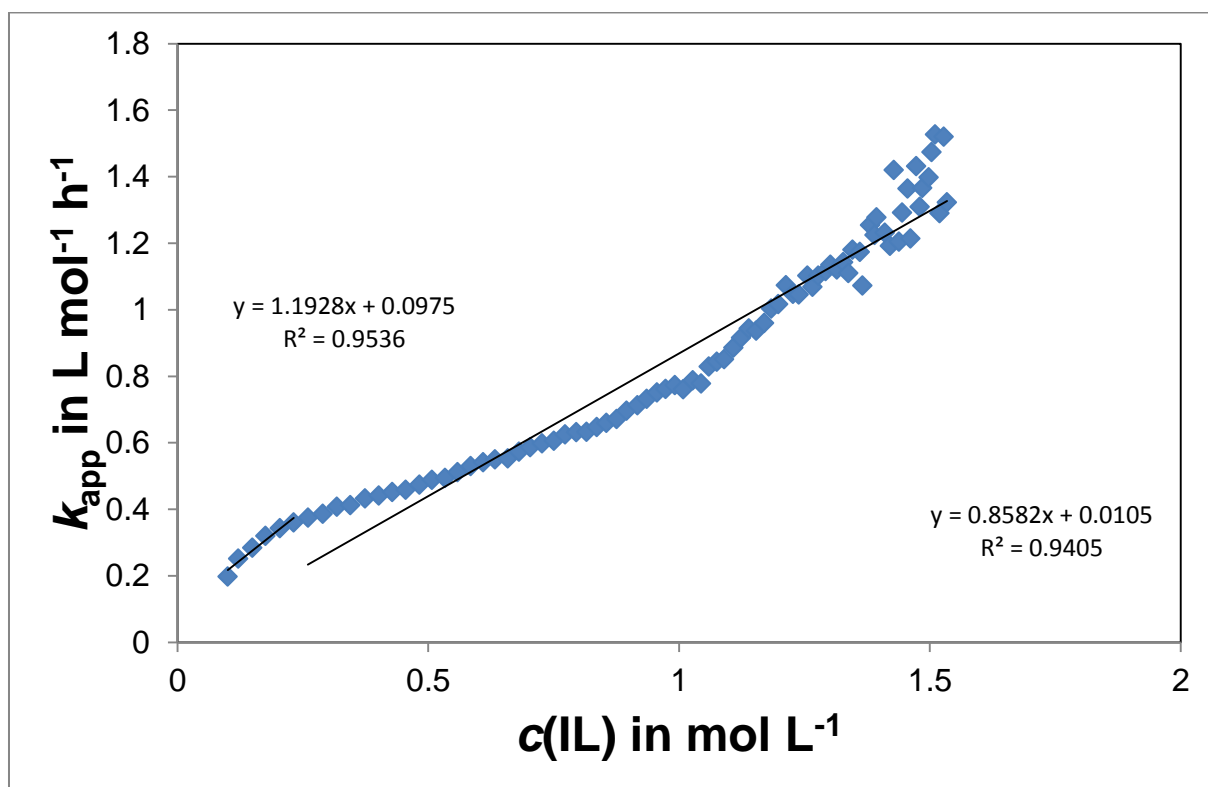
Figure 62: Plot of the reaction rate coefficient k_{app} vs. the product concentration c(IL) at 140 °C (Exp. No. OHL-061). The data points have been endowed with a linear fit function for the sections before and after the critical concentration.

3.3.2 Salting-Out Effect
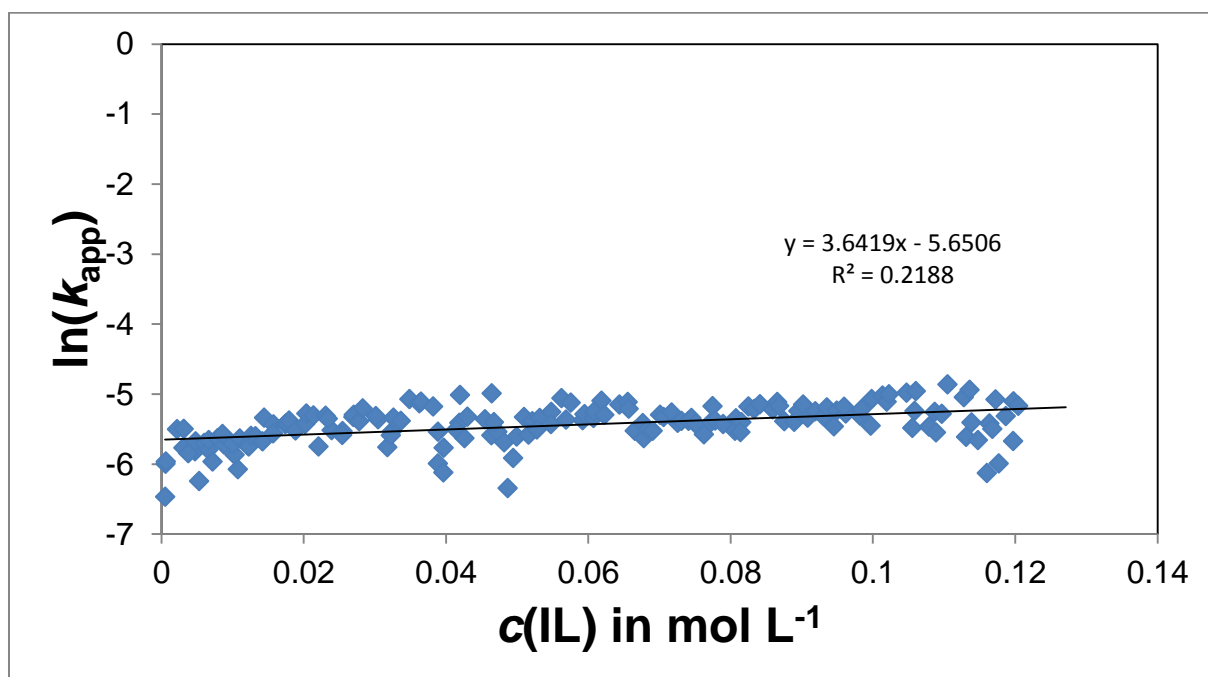
Figure 63: Plot of the logarithmised reaction rate coefficient $\ln(k_{app})$ vs. the product concentration c(IL) at 90 °C (Exp. No. OHL-057). The data points have been endowed with a linear fit function.
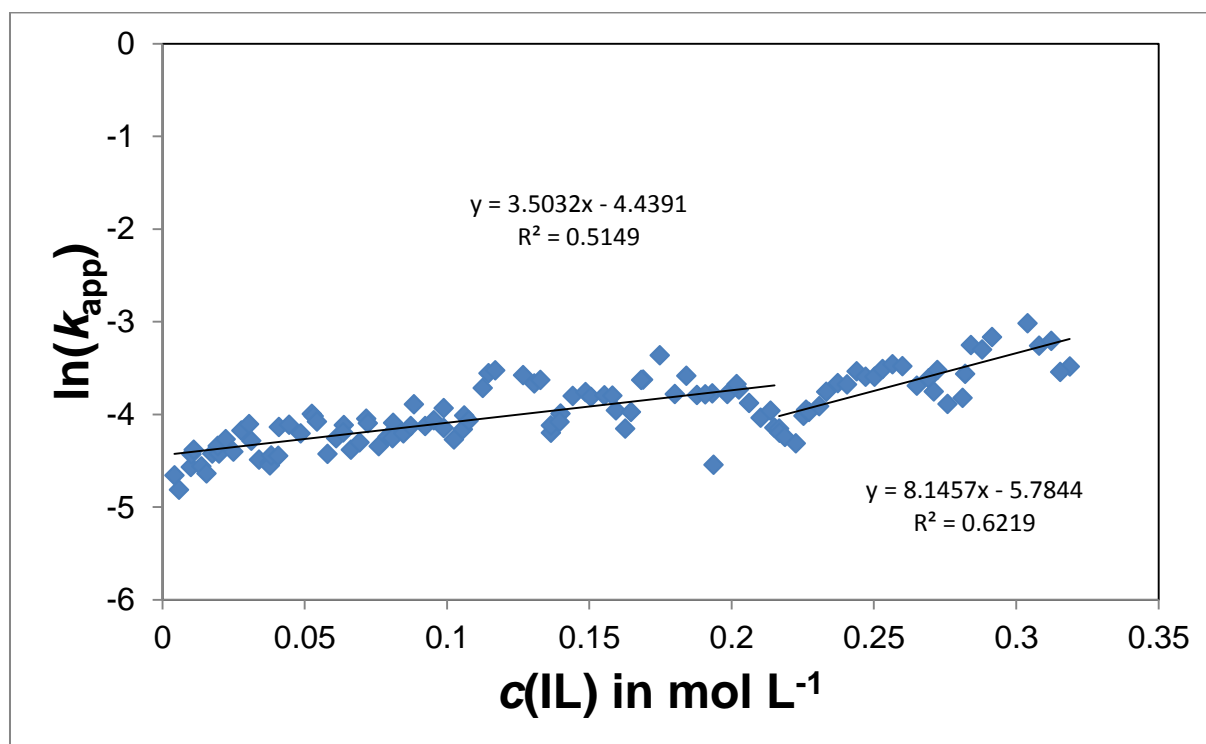
Figure 64: Plot of the logarithmised reaction rate coefficient $\ln(k_{app})$ vs. the product concentration c(IL) at 105 °C (Exp. No. OHL-069). The data points have been endowed with a linear fit function for the sections before and after the critical concentration.
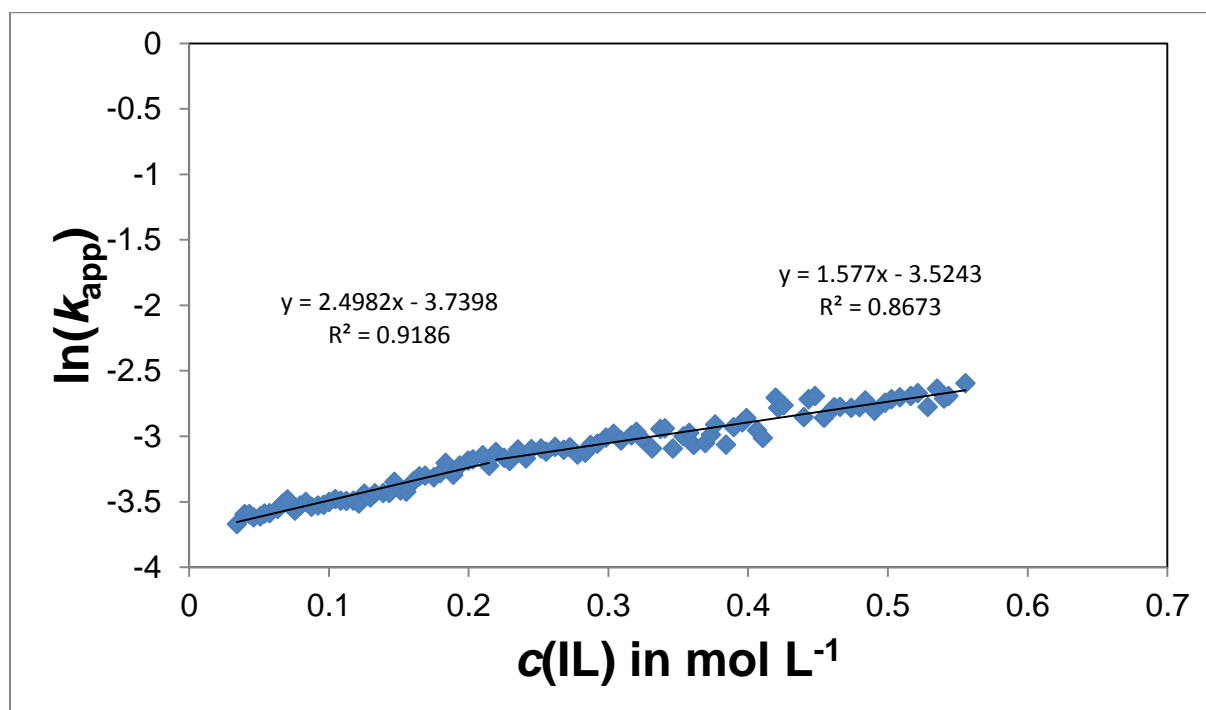
Figure 65: Plot of the logarithmised reaction rate coefficient $\ln(k_{app})$ vs. the product concentration c(IL) at 115 °C (Exp. No. OHL-068). The data points have been endowed with a linear fit function for the sections before and after the critical concentration.
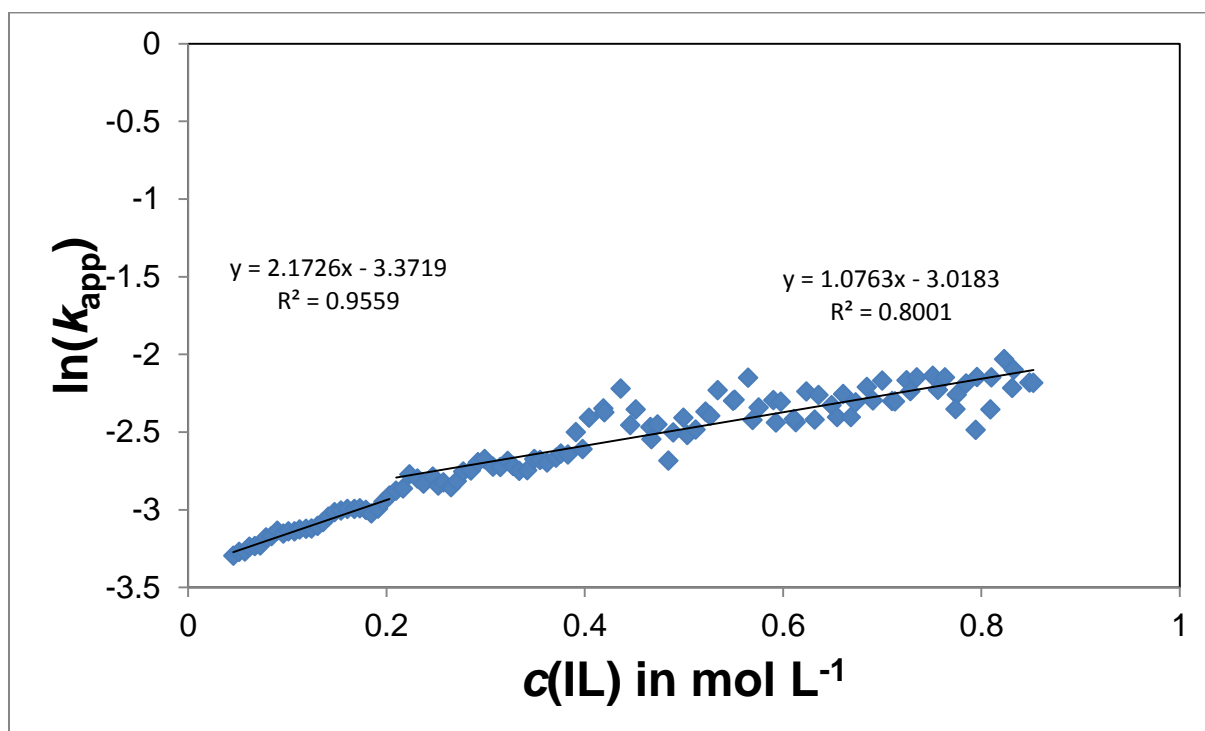
Figure 66: Plot of the logarithmised reaction rate coefficient $\ln(k_{app})$ vs. the product concentration $c(IL)$ at 120 °C (Exp. No. OHL-067). The data points have been endowed with a linear fit function for the sections before and after the critical concentration.
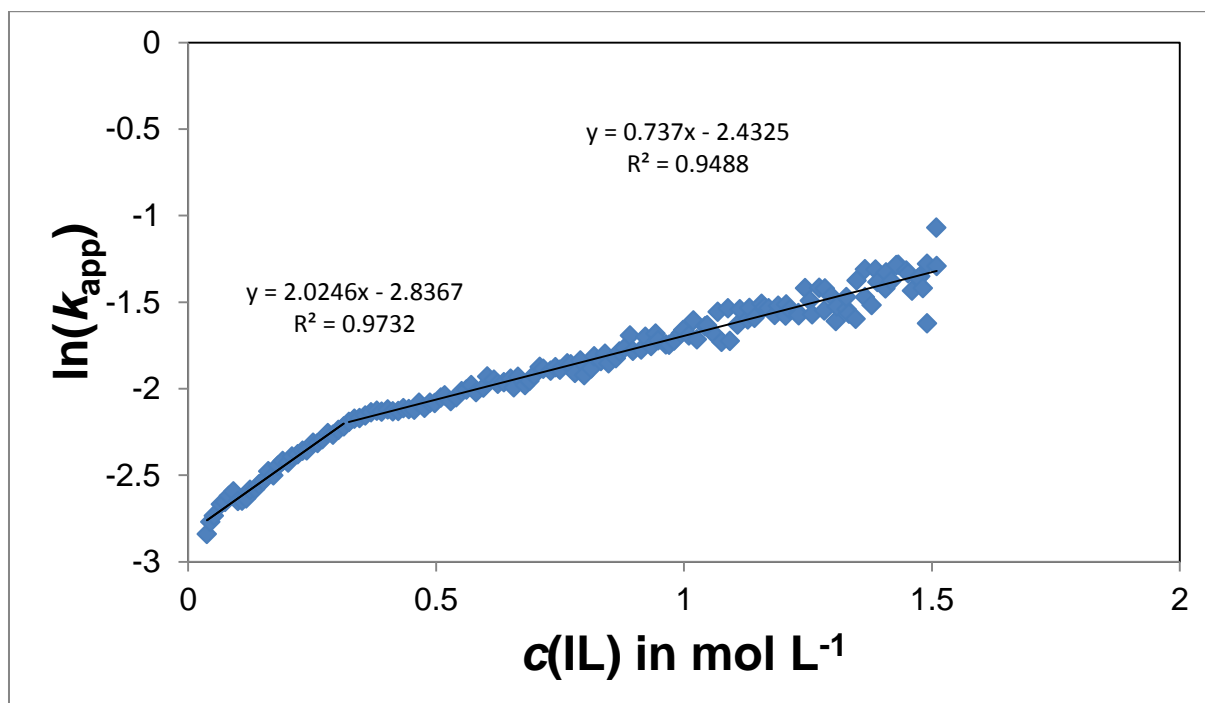
Figure 67: Plot of the logarithmised reaction rate coefficient $\ln(k_{app})$ vs. the product concentration $c(IL)$ at 125 °C (Exp. No. OHL-056). The data points have been endowed with a linear fit function for the sections before and after the critical concentration.

$y = 2.4976x - 3$
$R^2 = 0.9605$

$y = 0.7813x - 2.5363$
$R^2 = 0.9495$
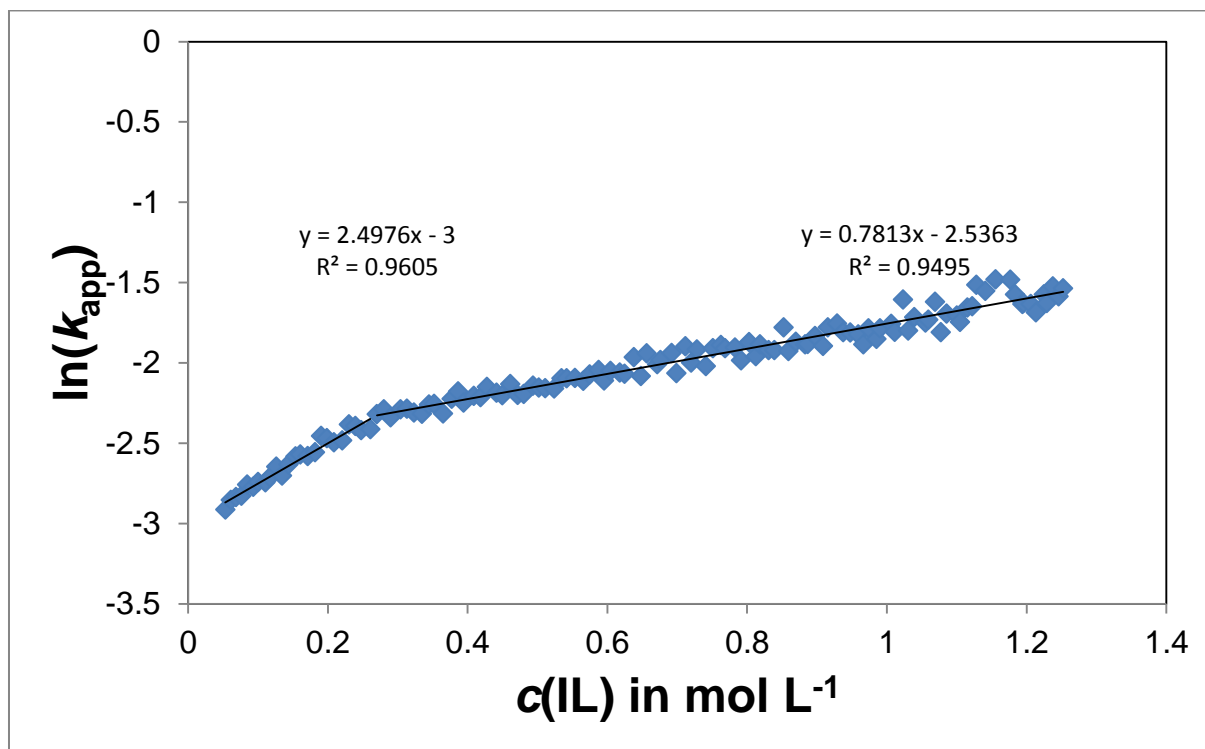
Figure 68: Plot of the logarithmised reaction rate coefficient $\ln(k_{app})$ vs. the product concentration c(IL) at 125 °C (Exp. No. OHL-064). The data points have been endowed with a linear fit function for the sections before and after the critical concentration.

$y = 0.8939x - 2.5718$
$R^2 = 0.9402$

$y = 2.3486x - 2.9279$
$R^2 = 0.9818$
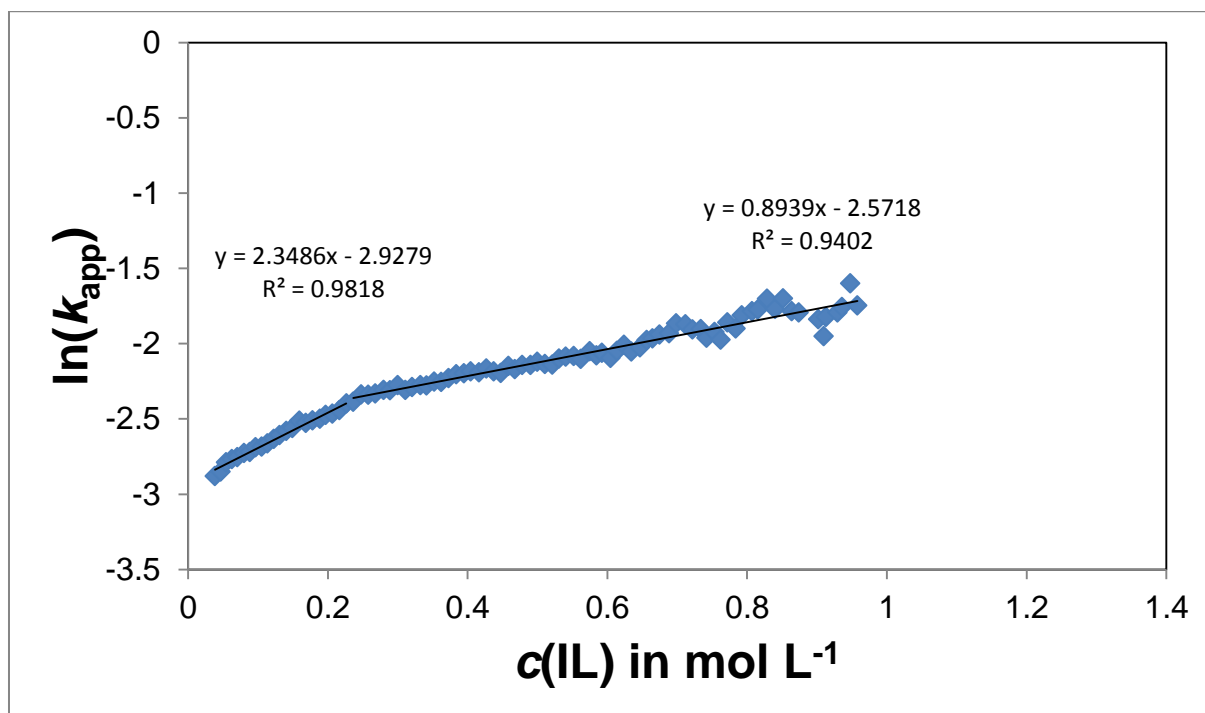
Figure 69: Plot of the logarithmised reaction rate coefficient $\ln(k_{app})$ vs. the product concentration c(IL) at 125 °C (Exp. No. OHL-066). The data points have been endowed with a linear fit function for the sections before and after the critical concentration.
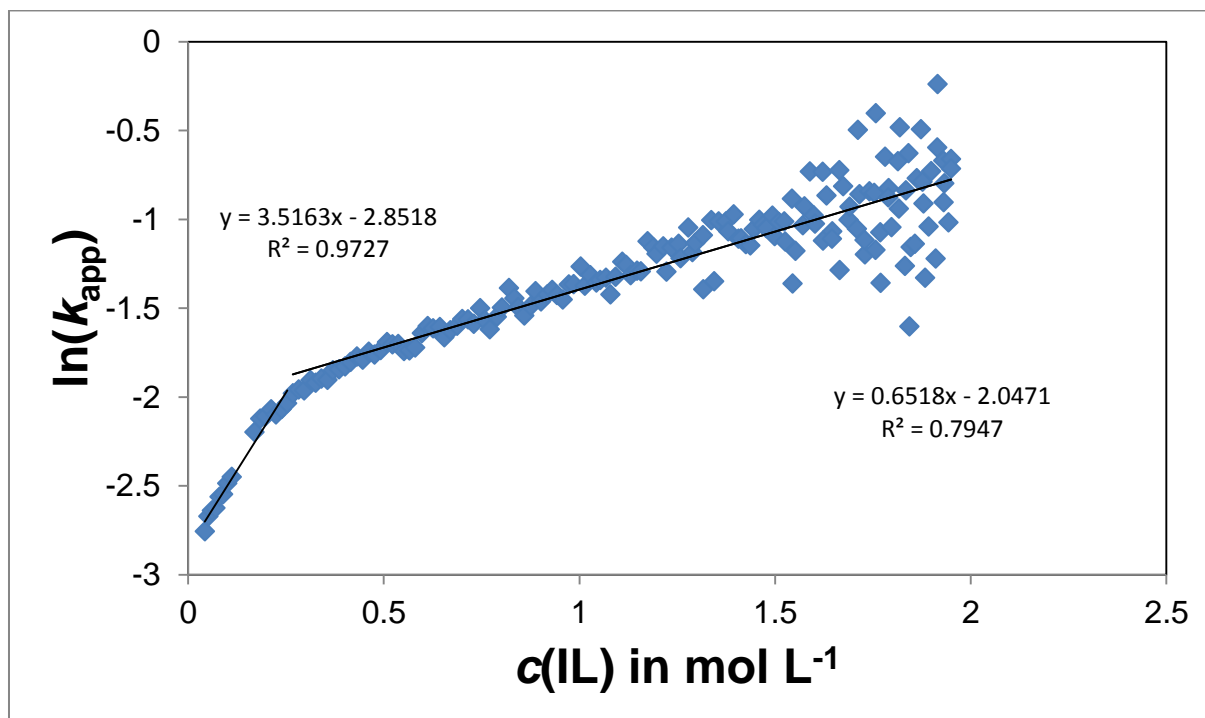
Figure 70: Plot of the logarithmised reaction rate coefficient ln(k_{app}) vs. the product concentration c(IL) at 130 °C (Exp. No. OHL-060). The data points have been endowed with a linear fit function for the sections before and after the critical concentration.
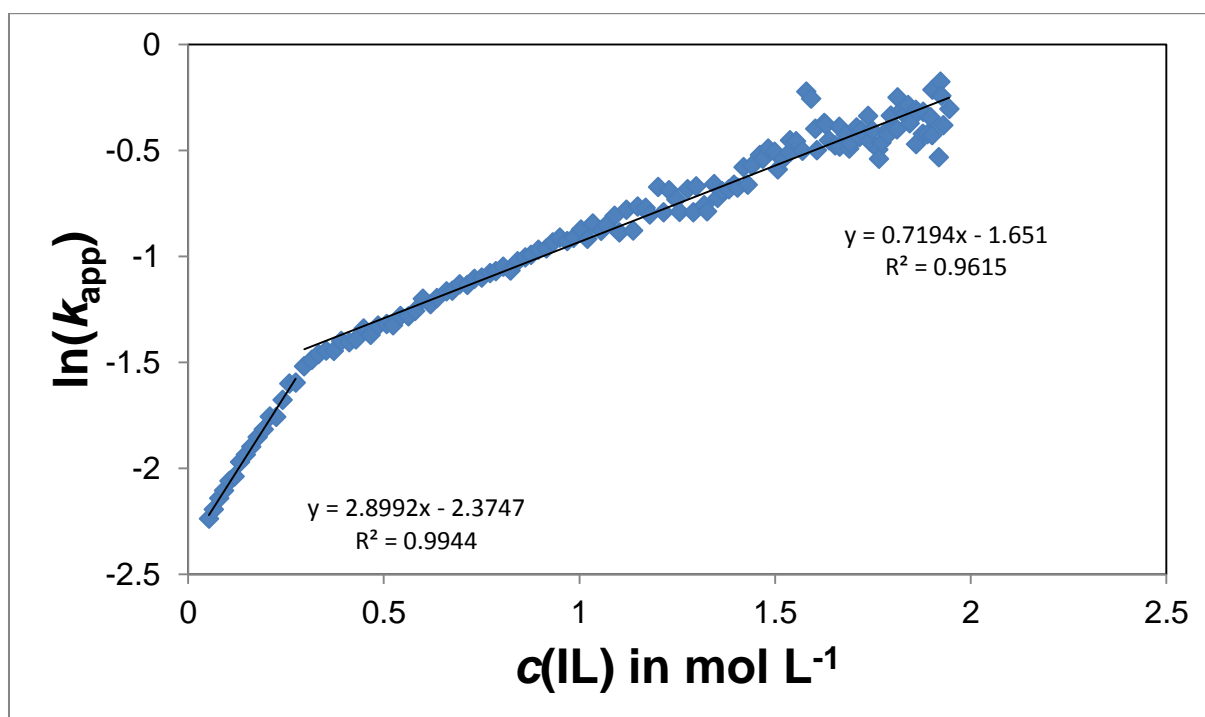
Figure 71: Plot of the logarithmised reaction rate coefficient ln(k_{app}) vs. the product concentration c(IL) at 135 °C (Exp. No. OHL-054). The data points have been endowed with a linear fit function for the sections before and after the critical concentration.
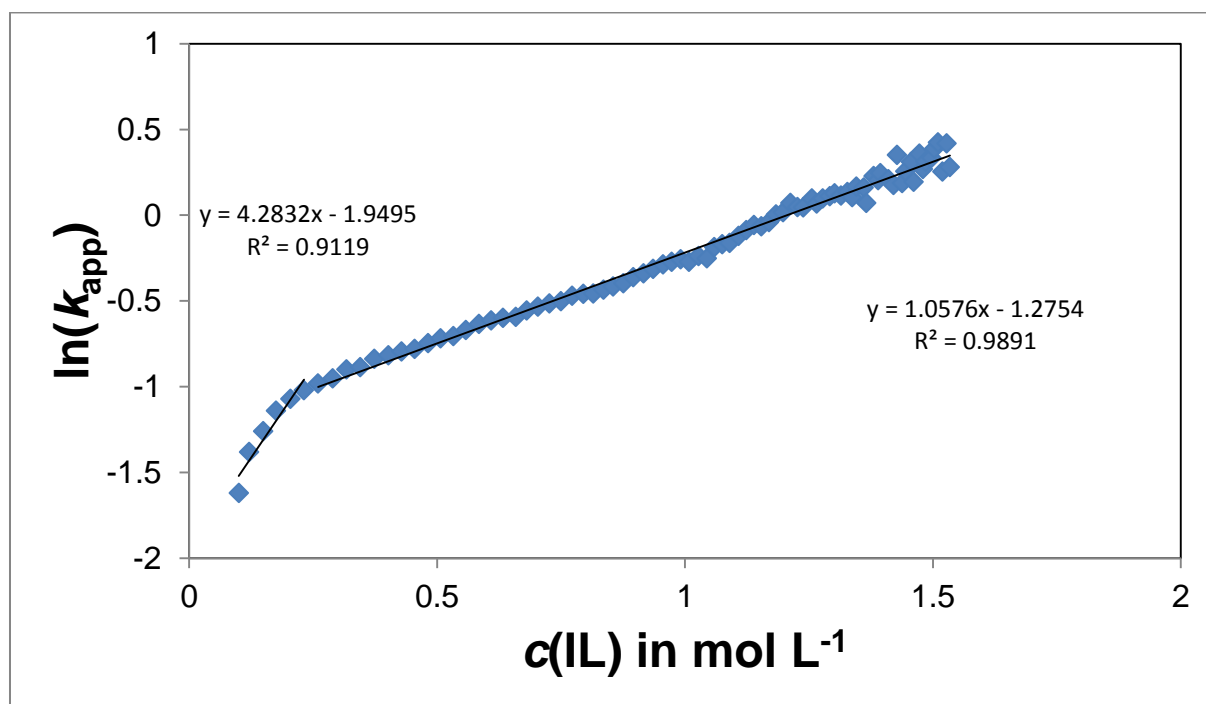
Figure 72: Plot of the logarithmised reaction rate coefficient $\ln(k_{app})$ vs. the product concentration c(IL) at 140 °C (Exp. No. OHL-061). The data points have been endowed with a linear fit function for the sections before and after the critical concentration.

3.3.3 Regular Solution Theory

To apply the regular solution theory, several approximations have been made. The enthalpy of vaporisation as well as the molar volume of $MeNEt_3$ MeOCOO at elevated temperatures are unknown, hence on the enthalpy of vaporisation has been estimated as 150 kJ mol^{-1} and the density of $MeNEt_3$ MeOCOO is determined by weighing 1 mL of substance in a 1 mL syringe (1.12 g mL^{-1}). As these conditions only enable a qualitative determination of δ_{mean}, the temperature dependence of molar volumes of the other substances and thereby the Hildebrandt parameter δ_{mean} are neglected (Eq. 2). Because of the expected volume expansion at elevated temperatures, the determined values of δ_{mean} are systematically underestimated. The values of heat of vaporisation and molar volume of substrates and solvent are taken from the NIST Chemistry Webbook[2].

The quadratic dependence mentioned in the communication is derived from the definition of the activity coefficient γ_i according to the regular solution theory[3] (Eq. 3) and the dependence of the apparent reaction rate coefficient k_{app} of the activity coefficients (Eq. 4 or Eq. 5). As the molar volume and the heat of vaporization of the transition state are unknown, only the general formulation of a quadratic dependence between $\ln(k_{app})$ and δ_{mean} can be achieved (Eq. 6). The discrepancy between the model and the results of this work (Fig. 72 to Fig. 81) is that the plots can be fitted with a linear function while the model predicts a quadratic dependence. Possibly, the systematic errors in the

determination of δ_{mean} mentioned above distort the shape of the curves. Furthermore, the general assumption of regular solution theory is that the compounds of a mixture behave as in pure substance and do not interact with each other. The polar solvent methanol and the produced ionic liquid definitely interact and thereby contradict this assumption. Additional terms which describe the interactions in the mixture could possibly reproduce the experimental data better.

$$\delta_i = \sqrt{\frac{\Delta_{vap}H_i - RT}{V_{m,i}}} \approx \sqrt{\frac{\Delta_{vap}H_i}{V_{m,i}}} \tag{2}$$

$$RT \ln(\gamma_i) = V_{m,i}(\delta - \delta_{mean})^2 \tag{3}$$

$$k_{app} = k_0'' \frac{\gamma(DMC) \cdot \gamma(NEt_3)}{\gamma(transition\ state)} \tag{4}$$

$$\ln(k_{app}) = \ln(k_0'') + \sum_i \ln(\gamma_i^{v_i}) \tag{5}$$

$$\ln(k_{app}) = \ln(k_0'') + a_1 \delta_{mean}^2 + a_2 \cdot \delta_{mean} + a_3 \tag{6}$$
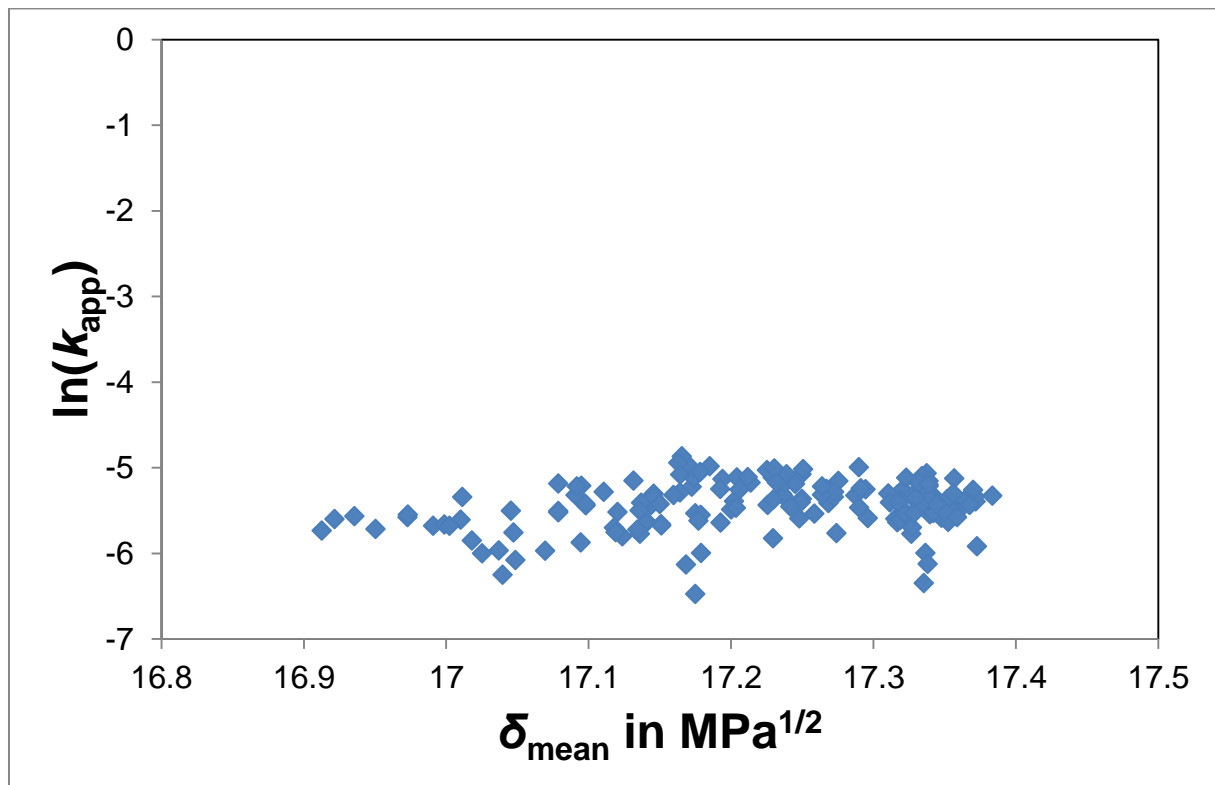
Figure 73: Plot of the logarithmised reaction rate coefficient ln(k_{app}) vs. the averaged Hildebrand parameter δ_{mean} at 90 °C (Exp. No. OHL-057). Because of the strong scattering of the data points, the usage of a fit function is renounced.
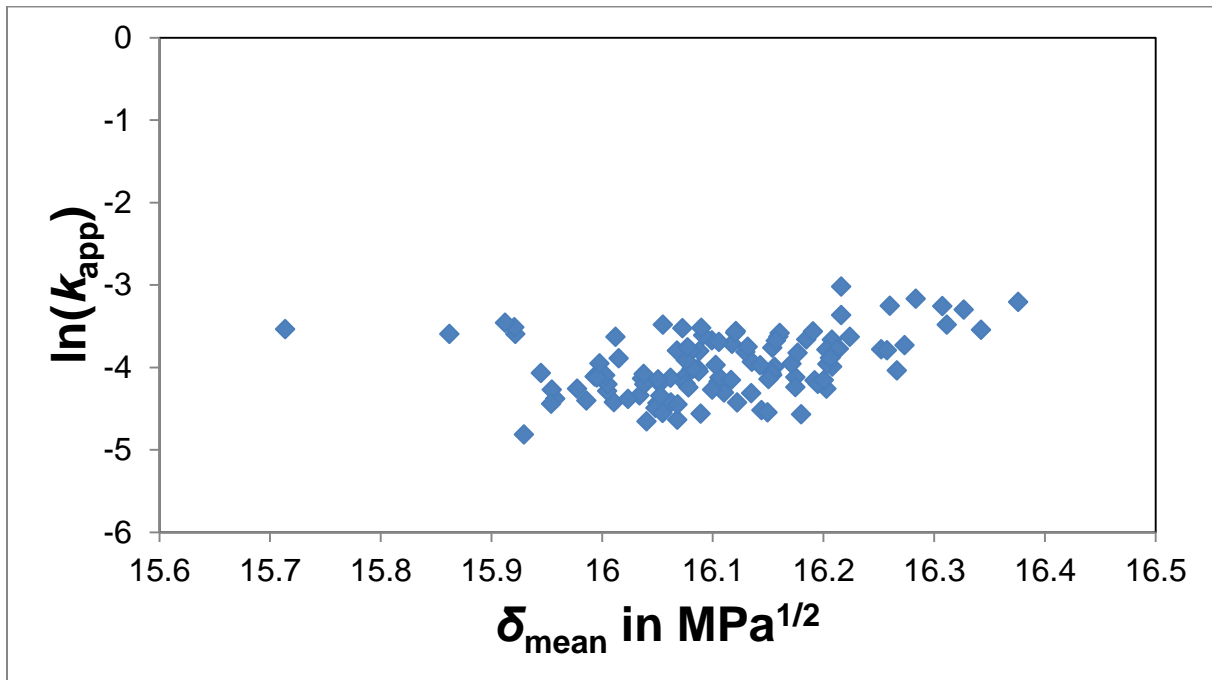
Figure 74: Plot of the logarithmised reaction rate coefficient ln(k_{app}) vs. the averaged Hildebrand parameter δ_{mean} at 105 °C (Exp. No. OHL-069). Because of the strong scattering of the data points, the usage of a fit function is renounced.
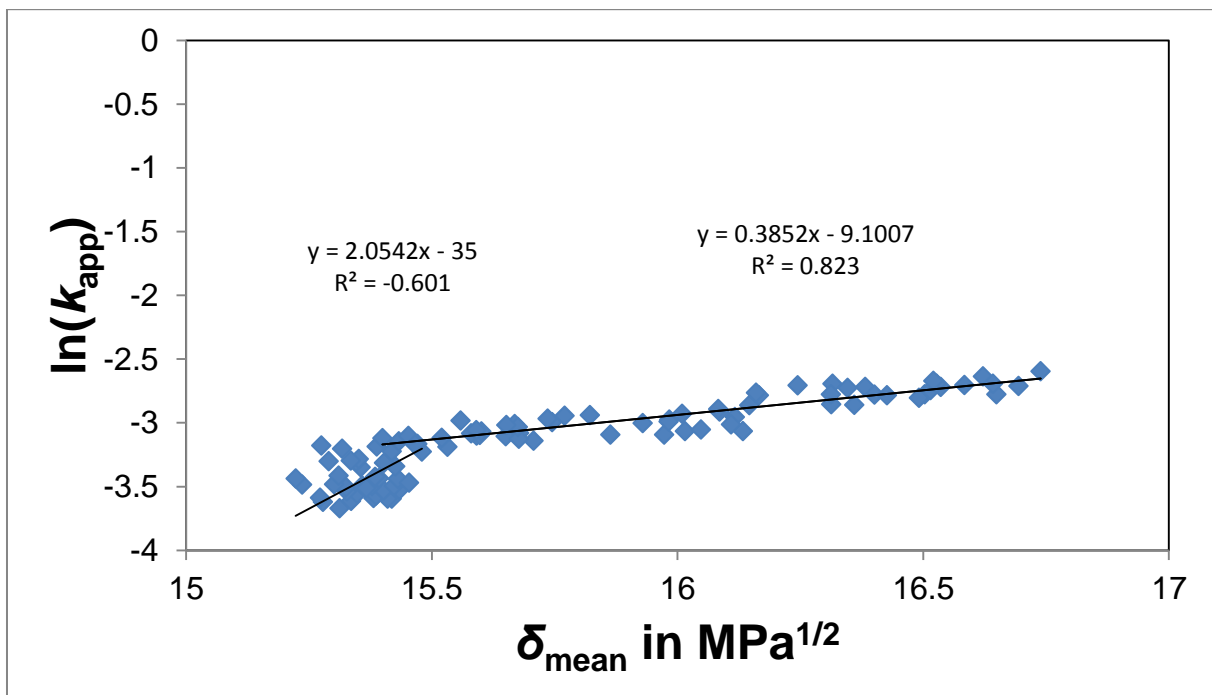
Figure 75: Plot of the logarithmised reaction rate coefficient ln(k_{app}) vs. the averaged Hildebrand parameter δ_{mean} at 115 °C (Exp. No. OHL-068). The data points have been endowed with a linear fit function for the sections before and after the critical concentration.
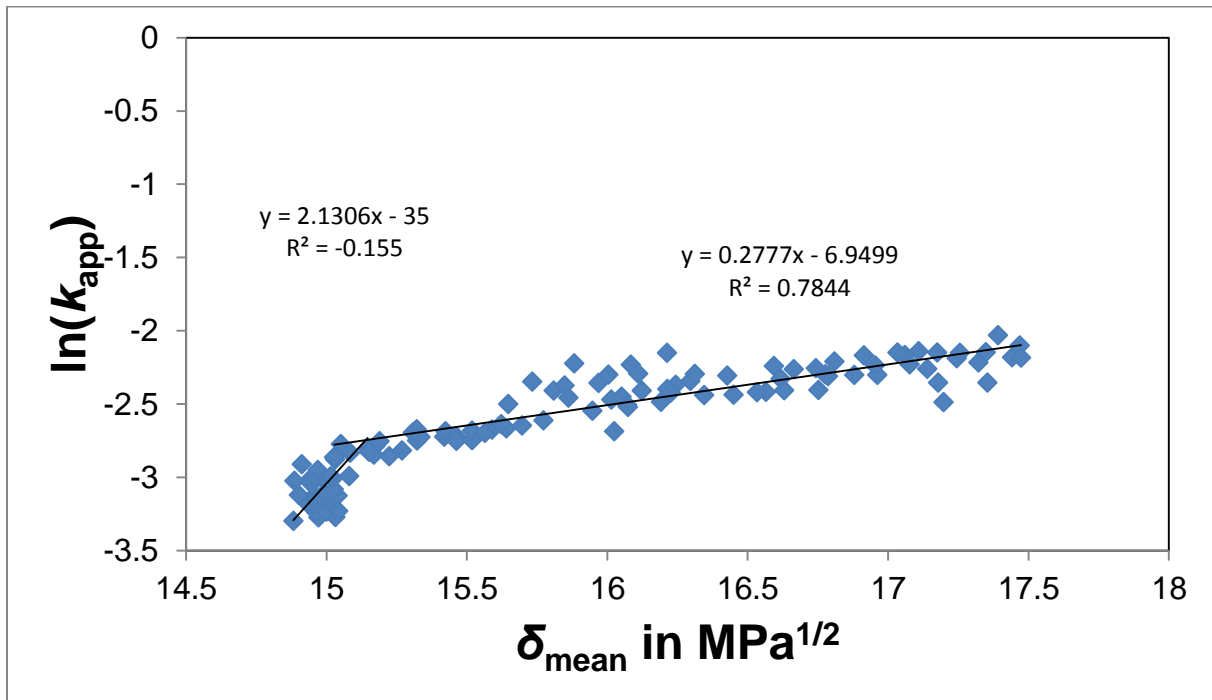
Figure 76: Plot of the logarithmised reaction rate coefficient ln(k_{app}) vs. the averaged Hildebrand parameter δ_{mean} at 120 °C (Exp. No. OHL-067). The data points have been endowed with a linear fit function for the sections before and after the critical concentration.
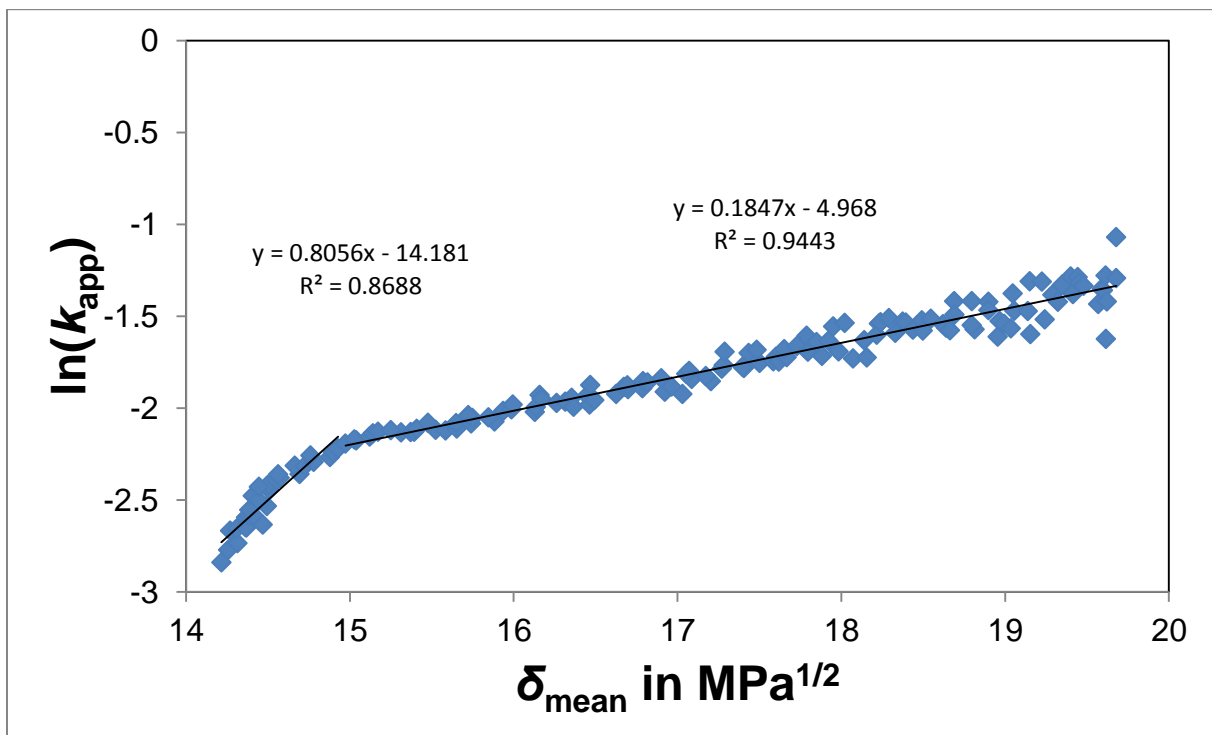
Figure 77: Plot of the logarithmised reaction rate coefficient ln(k_{app}) vs. the averaged Hildebrand parameter δ_{mean} at 125 °C (Exp. No. OHL-056). The data points have been endowed with a linear fit function for the sections before and after the critical concentration.
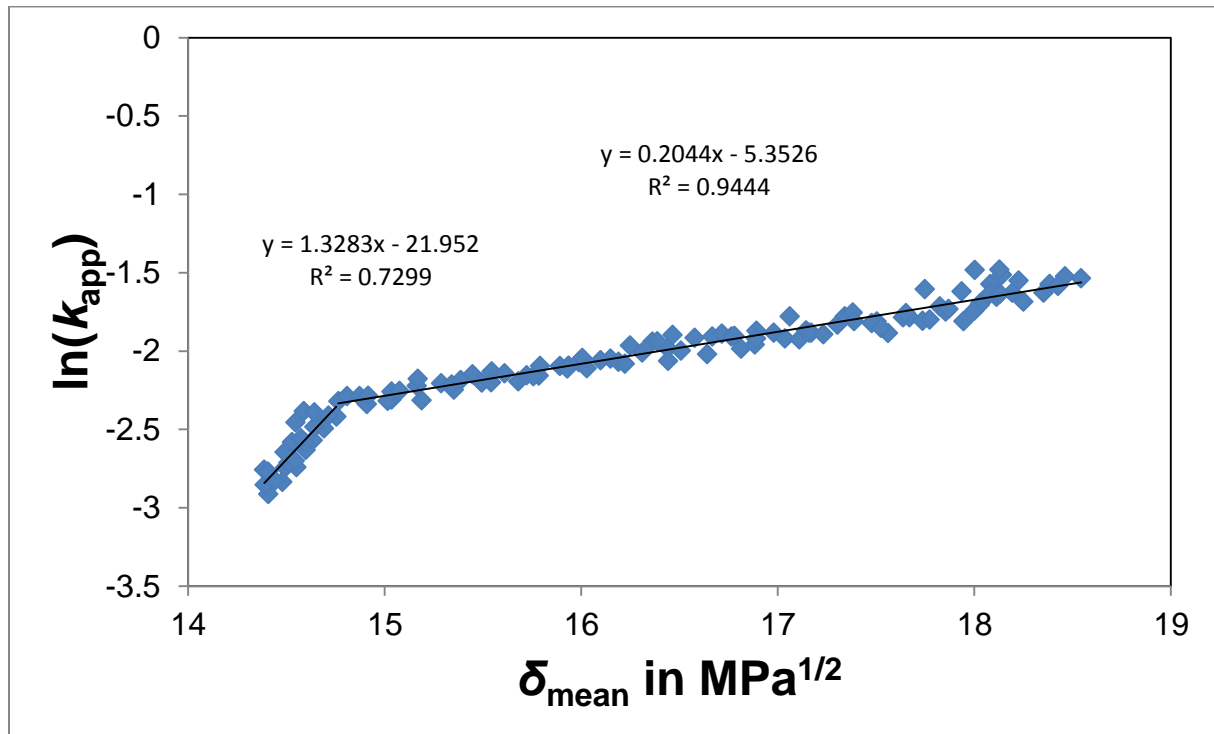
Figure 78: Plot of the logarithmised reaction rate coefficient ln(k_{app}) vs. the averaged Hildebrand parameter δ_{mean} at 125 °C (Exp. No. OHL-064). The data points have been endowed with a linear fit function for the sections before and after the critical concentration.
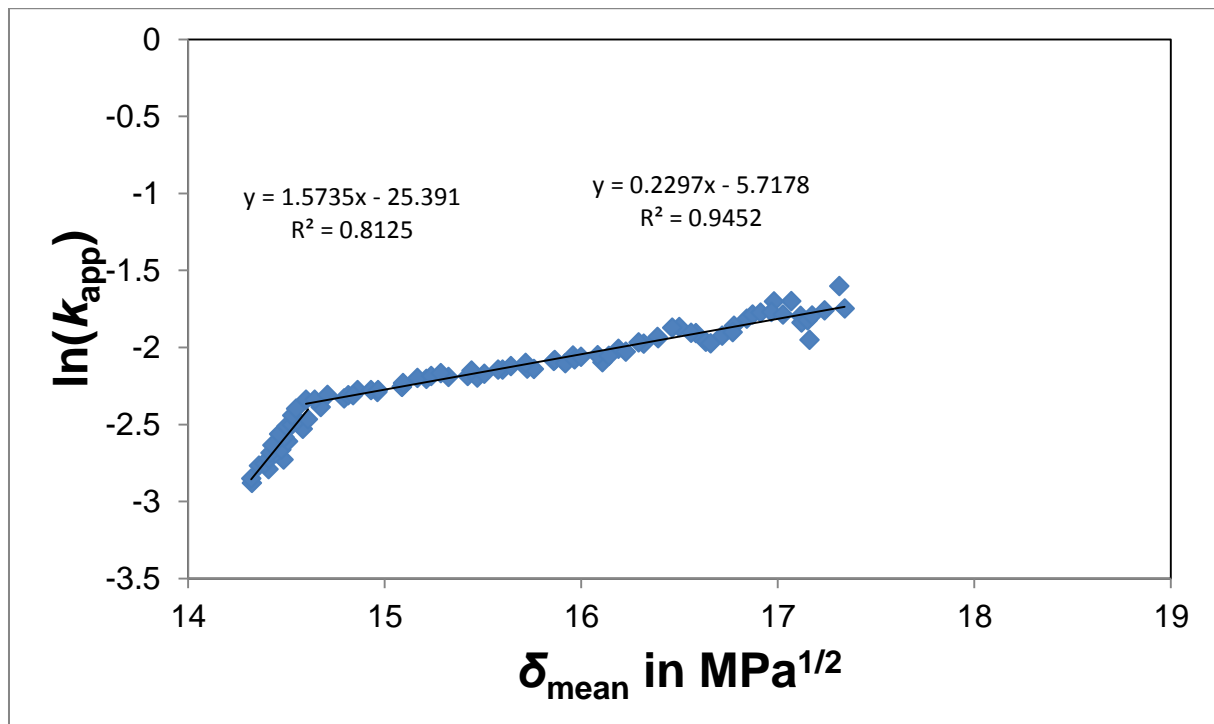
Figure 79: Plot of the logarithmised reaction rate coefficient ln(k_{app}) vs. the averaged Hildebrand parameter δ_{mean} at 125 °C (Exp. No. OHL-066). The data points have been endowed with a linear fit function for the sections before and after the critical concentration.
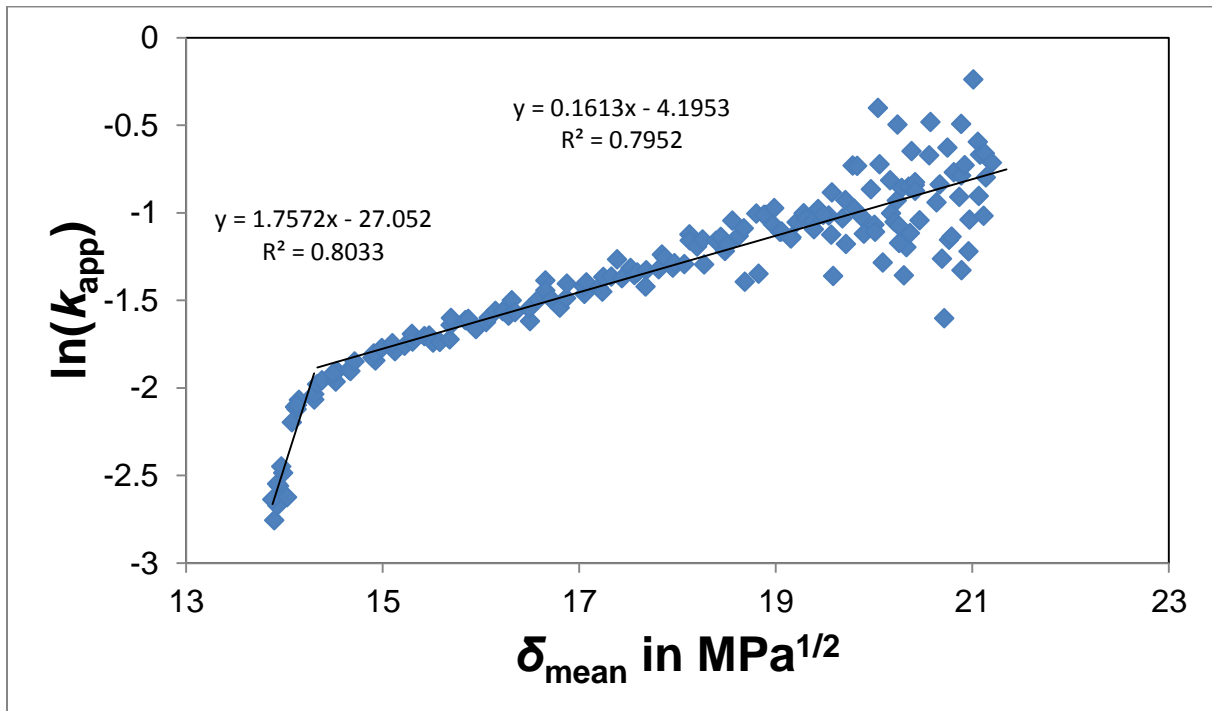
Figure 80: Plot of the logarithmised reaction rate coefficient ln(k_{app}) vs. the averaged Hildebrand parameter δ_{mean} at 130 °C (Exp. No. OHL-060). The data points have been endowed with a linear fit function for the sections before and after the critical concentration.
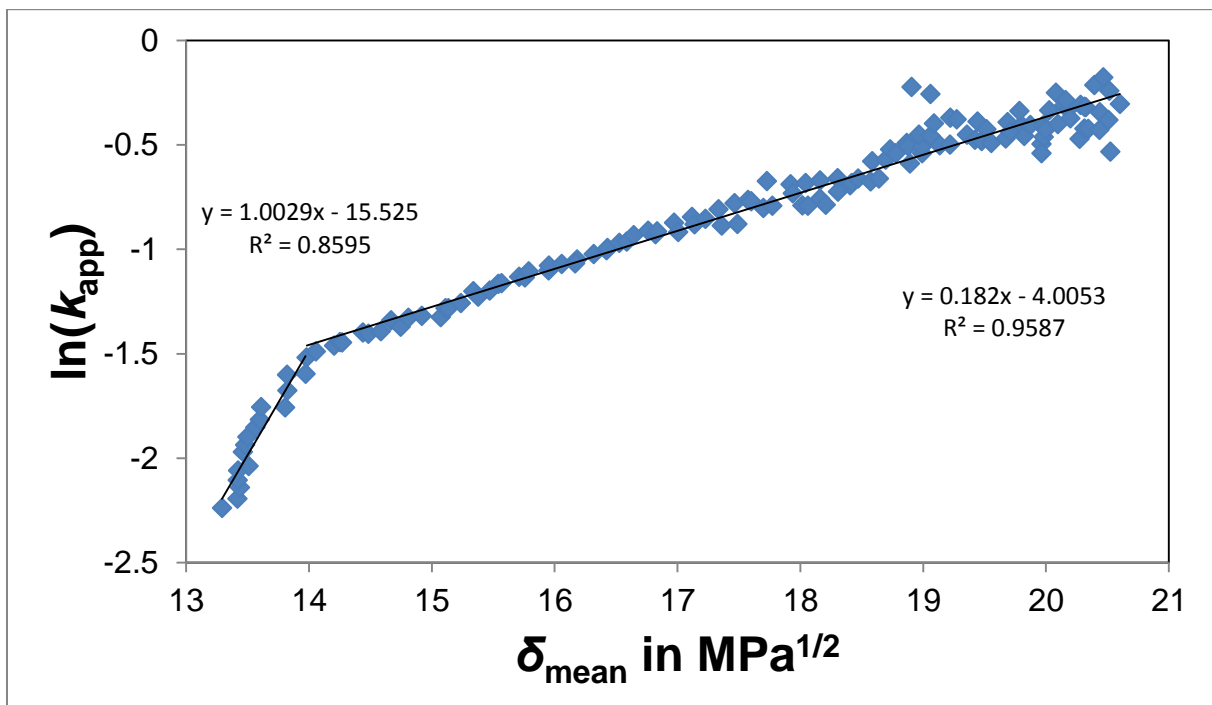
Figure 81: Plot of the logarithmised reaction rate coefficient ln(k_{app}) vs. the averaged Hildebrand parameter δ_{mean} at 135 °C (Exp. No. OHL-054). The data points have been endowed with a linear fit function for the sections before and after the critical concentration.
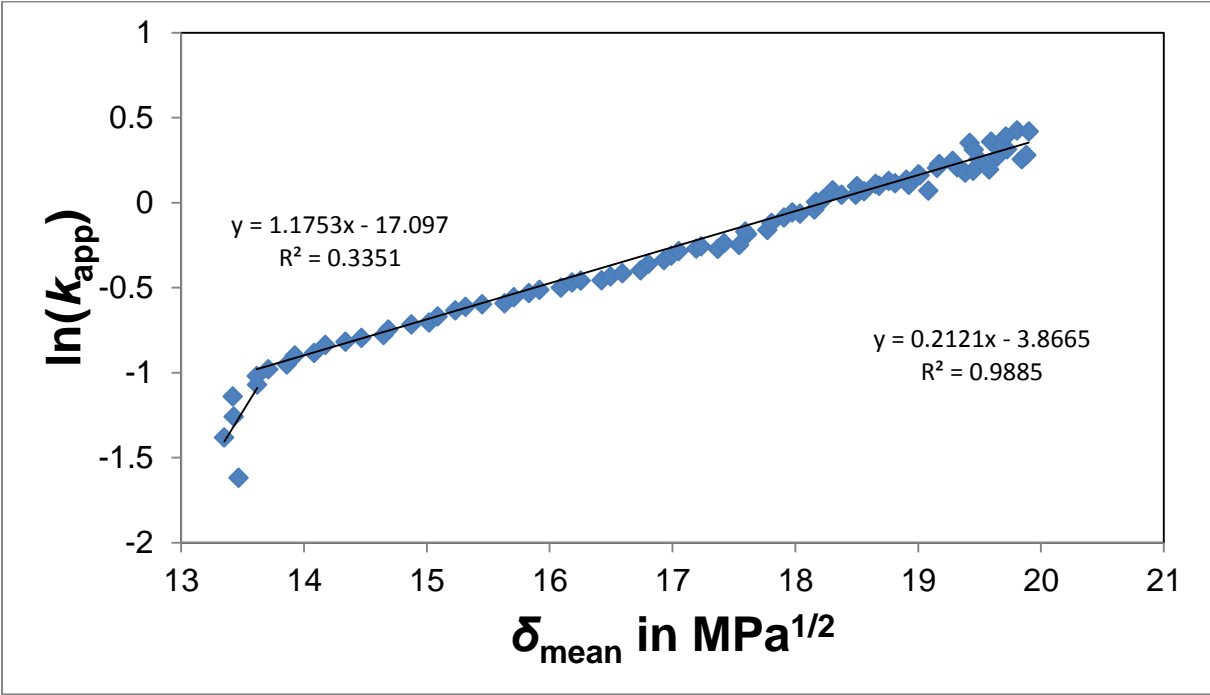
Figure 82: Plot of the logarithmised reaction rate coefficient ln(k_{app}) vs. the averaged Hildebrand parameter δ_{mean} at 140 °C (Exp. No. OHL-061). The data points have been endowed with a linear fit function for the sections before and after the critical concentration.

References

[1] NIST Computational Chemistry Comparison and Benchmark Database, NIST Standard Reference Database Number 101, Release 18, October 2016, Editor: Russell D. Johnson III http://cccbdb.nist.gov/

[2] P.J. Linstrom and W.G. Mallard, Eds., NIST Chemistry WebBook, NIST Standard Reference Database Number 69, National Institute of Standards and Technology, Gaithersburg.

[3] B. E. Poling, J. M. Prausnitz and J. P. O'Connell, The Properties of Gases and Liquids, 5th ed., Mc Graw-Hill, Singapore, 2007, 8.44.